DOI:10.15774/PPKE.ITK.2015.011

Microfluidic Particle Separation Techniques for Biomedical Use

András József Laki

Faculty of Information Technology and Bionics

Pázmány Péter Catholic University

Supervisors:

Kristóf Iván, Ph.D.

Pierluigi Civera, Ph.D. †

Danilo Demarchi, Ph.D.

A thesis submitted for the degree of

Doctor of Philosophy

June 2015

DOI:10.15774/PPKE.ITK.2015.011

Acknowledgements

I would like to thank my supervisors: Tamás Roska†, Pierluigi Civera†, Kristóf Iván, and Danilo Demarchi for having kept me on track. You were always a source of new, and different perspectives to every problem. I greatly appreciate all of the help from the members of the Department of Genetics, Cell- and Immunobiology, the Department of Biophysics and Radiation Biology at Semmelweis University, and the Faculty of Veterinary Science at Szent István University especially from Edit I. Buzás, Viola Tamási, Tamás Szabó, Miklós Kellermayer, István Huszár, Éva Fok, and Olga Jacsó.

I am grateful to Péter Fürjes, Zoltán Fekete, Magdolna Erös, Károlyné Payer, Gabriella Biró and other members of MEMS Laboratory at Research Centre for Natural Sciences of Hungarian Academy of Sciences for helping me in the fabrication of the microfluidic devices. I would like to thank my colleagues at the Polytechnic University of Turin especially to Paolo Motto†, Alessandro Sanginario, Dario Trimarchi, Andrea Carola, Ismael Rattalino, Alice Diemonte and the other member of the MINES lab. Finally, I would like to thank my colleagues and my students at the Pázmány Péter Catholic University, especially to Eszter Leelössyné Tóth, Zsófia Sztyéhlikné Bérces, and Márton Hartdégen.

I have been blessed with a wonderful family that has been an unending source of support and encouragement. I especially want to thank my parents for giving me strength to continue. Finally, I give my deepest thanks to Ágnes for her amazing love and support.

DOI:10.15774/PPKE.ITK.2015.011

Abstract

Sorting and separation of micron-sized particles have an increasing importance in biomedical diagnostics, biochemical analyses, food and chemical processing, and environmental assessment. By employing the unique characteristics of microscale flow phenomena, various techniques have been established for fast and accurate separation, and sorting of cells or particles in a continuous manner. As in classical separation procedures, the size-fractionation of particles or cells could be realized in passive or active methods. Passive procedures, which do not require any external force-field, utilize the interaction between particles, flow, and the channel structure and particles to separate different-sized particles. Meanwhile, active separation techniques make use of external force-fields in different ways.

This doctoral thesis provides a novel pathogen detection device (Flow Through Nematode Filter, FTNF), and a novel application of an asymmetric column structure, which is called deterministic lateral displacement (DLD) device. These can be integrated into biochips that can provide further downstream analysis of the separation products. The working principles are explained in detail, and performances of the devices are discussed through measurement results.

The main application target of the present work is medicine and biomedical research but we are also open for other application areas. The use of these simple microfluidic devices will make it possible to extend the use of cell-sorting in point of care settings, closer to the patient at the clinic or in the field.

Keywords: Microfluidic fractionation procedures · Pathogen enrichment from blood · Blood fractionation · Microvesicle separation from serological samples

DOI:10.15774/PPKE.ITK.2015.011

Contents

DOI:10.15774/PPKE.ITK.2015.011

DOI:10.15774/PPKE.ITK.2015.011

Chapter 1

Introduction

Microfluidics concerns design, fabrication, and experiments of miniaturized fluidic systems, which has undergone rapid developments during the last two decades [1]. As an interdisciplinary area, this rapidly growing field of technology has numerous applications in biomedical diagnostics, chemical analysis, automotive, and electronic industries [2]. One of the pivotal applications of microfluidics is the development of lab-on-a-chip (LOC) devices as point-of-care (POC) diagnostic tools. A typical LOC device includes various functional modules: sample transport, sample preparation, separation, detection, and analysis module [3, 4]. The label-free size separation of particles or cells is vital to many of the analytical and preparative techniques used in the fields of chemical, biochemical, and clinical analysis, which led to ground breaking advances in terms of speed of analyses, resolution of separations, and automation of procedures [5]. Additionally, microfluidic separator devices can form a part of portable systems for point-of-care or on-the-spot detection [6].

Several variations of microfluidic cell sorters, which implement different sorting mechanisms, have been designed and fabricated [7, 8]. The chosen method of particle handling is generally based on the nature of application, which strongly depends on the composition of the sample and the final goal of the analysis should also be considered. Several strategies exist for this purpose based on specific cell/particle characteristics including manipulation of particles in fluids or removal of particulate matter from fluids [9]. The particles may act or interact with the analyte, in which case they need to be removed from the sample [10].

DOI:10.15774/PPKE.ITK.2015.011

1.1 Traditional Fractionation Techniques of Biological Samples

In traditional cell isolation processes, size separation is commonly used to separate mixtures of cells or particles before subsequent analysis or culturing [10]. Cells exhibit variations in their hydrodynamic radii stemming from changes in volume, shape or mechanical properties, dependent on their state of health [11]. The existing cell separation methodologies can be classified into two main groups to enrich selected subpopulations [8]. The first group is based on physical descriptors like size, shape, and density differences and includes filtration and centrifugation techniques, which are commonly used for debulking heterogeneous samples [12, 13]. The second group comprises affinity methods such as capture on affinity solid matrix (beads, plates, fibers) [14–16], fluorescence-activated cell sorting (FACS) [17, 18] and magnetic cell sorting [19, 20], which are based upon biochemical cell surface characteristics and biophysical criteria [8].

Traditional fractionation instruments ranging in size from desktop to room sized models are standard pieces of equipment at most clinical laboratories and are used to analyze and separate cells and other biological particles [21]. The drawbacks of the existing, traditional flow cytometers are that these devices are expensive, require an extensive complementary infrastructure; such as facilities, personnel and reagents. They are not suited to integration with other analysis steps, and time is required to process the signal data limits the rate at which cells can be detected. Much work is therefore being done to develop methods that will not only be cheaper, and therefore more easily available, but also more effective and possibly able to probe particle properties not currently accessible [21].

In clinical diagnostic sense, cell sorting and counting devices are examples of technological solutions that have been designed and optimized for use in centralized laboratories, much like the very first computers. Also nowadays the biological samples (blood, urine, other biological liquids) are collected from patients at the hospitals, at home or in special environments and sent to these centralized diagnostic laboratories where analysis takes place. However, the transportation of samples requires money and time, and the quality of samples may decay due to natural biological processes.

DOI:10.15774/PPKE.ITK.2015.011

1.2 Review of Separation Technologies Integrated into Microfluidic devices

The trend in life science research to miniaturize analytical processes using microfluidic devices, was first seen in the late eighties, and it is still ongoing [1]. The benefits of miniaturization and integration are including increased automation, parallelization, speed, resolution and portability as described in reviews by Mosadegh [22], Craighead [23], Mark [24], Erickson [25], Franke [26] and Dittrich [27]. The idea of integrating sampling, sample handling, reactions, separations and detection into one automated device containing interconnected microchannel networks led to the introduction of the term micro-total-analysis-system (μTAS) in the literature in 1990 by Manz et al. who performed first on-chip separation implementing capillary electrophoresis fractionation of fluorescent molecules [28, 29]. Since that time, applications of μTAS has developed over the past two decades exponentially, meanwhile scientific journals, conferences, and companies specializing in LOC technologies are vivid examples of how theinterest in this field has grown.

In sense of cell isolation, the efficiency of fractionation takes into consideration the available sample volume for analysis, the characteristic/feature that distinguishes the cell types, the required purity of the separated population with desired characteristics, the total number of cells lost during the process of separation, the viability of cells after separation and the physical stress endured by the cells. Finally, choosing an efficient sample handling procedure, the time required for the complete cell separation process and the cost-effectiveness of the technique are also not negligible.

The integration of particle separation techniques into lab-on-a-chip devices is advantageous, as described by Pamme [30], that these label-free processes are continuous, the separation can be monitored continuously and the sample components are displaced laterally thus each fraction could be collected independently. Based on the applied forces the fractionation could be tangential or perpendicular to the flow direction and can be realised as batch or continuous loading procedures (Fig. 1.1). In batch separation techniques, the particles follow the same paths but at different rates which appears as fractionation over time only; thus, these procedures require precise injection of a very small amount of sample into the separation channel. At the other case, the applied forces have perpendicular components to the flow direction thus the particles are

DOI:10.15774/PPKE.ITK.2015.011

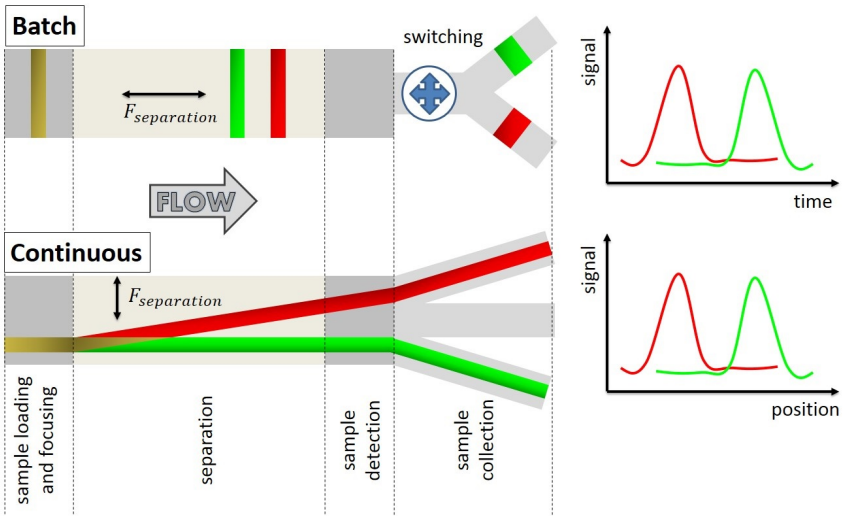

Figure 1.1: Batch separation procedure entails the injection of finite volumes parallel to the flow direction into a separation column. The separated sample fractions pass through a detector at different times, often followed by repeats to optimize separation parameters. Collection of the separated fractions can only be achieved with a flow switching mechanism that redirects different components to different outlets. Continuous procedure separate perpendicularly to the flow direction. The sample is injected continuously together with a carrier liquid, meanwhile the separation efficiency can be monitored in real-time. (adapted from Ref. [30])

displaced laterally and become separated in space.

A range of field flow fractionation (FFF) techniques have been reported for separation of particles in lab-on-a-chip based microfluidic systems [30] since FFF method was pioneered by Giddings in 1960s [31]. The continuous-loaded single-phase field flow fractionation requires external forces or uses only inertial shear forces.

Large variety of methods have been developed to date that operate by external forces but in each case, the special cell properties and attributes have to be taken into consideration. Table 1.1 gives an overview of the different continuous particle separation methods which are based on external perpendicular forces to the direction of flow and focuses on the utilized external forces and the basis of separation. These separation methods can be classified by the applied external forces into acoustophoresis, dielectrophoresis, magnetophoresis, appication of mechanical forces and optophoresis.

The requirement of external forces increases the complexity of the device and may limit the application for some specific reagents such as biological samples. Conse-

DOI:10.15774/PPKE.ITK.2015.011

1.2 Review of Separation Technologies Integrated into Microfluidic devices

Method	Separation induced by	Separation based on	References
Acoustophoresis	Acoustic pressure	Size, density, compressibility	[32–37]
Dielectrophoresis	Inhomogeneous electric field	Size, polarisability	[38–45]
Magnetophoresis	Inhomogeneous magnetic field	Size, magnetization	[46–51]
Mechanical forces	Gravity, centrifugation	Size, density	[52–55]
Optophoresis	Optical force	Size, refractive index	[56–58]

Table 1.1: Listing of continuous flow separation methods using external forces with details of the forces utilized and the basis of separation were taken from the selected references.

quently, researchers have been paying attention to the development of novel physical methods (Table 1.2), which are based on varying only the geometry of microchannels, modifying the flow profile and influencing local flow properties such as bifurcation channels, deterministic cell rolling (DCR), deterministic lateral displacement (DLD), pinched-flow fractionation (PFF) devices, applying Dean effect, or using flow-through filters/membranes.

Hydrophoretic techniques	Separation based on	References
Bifurcation channels	Zweifach-Fung effect	[59–67]
Dean flow	Dean effect	[68–76]
Deterministic cell rolling (DCR)	Shear-induced and wall-induced lift	[77–82]
Deterministic lateral displacement (DLD)	Shear-induced and wall-induced lift	[83–101]
Flow-through filters (FTF)	Pressure field gradient	[102–108]
Pinched flow fractionation (PFF)	Shear-induced and wall-induced lift	[109–124]

Table 1.2: List of continuous flow separation methods using inertial forces detailing the basis of separation based on the selected references.

Comparison of performance of integrable sample fractionation methods is not always straightforward. Plenty of approaches provide high throughput, meanwhile others offer high resolution. Several of the microfluidic devices are simple in terms of operation,

DOI:10.15774/PPKE.ITK.2015.011

whilst other techniques might require a specialist. A number of separation principles require labelling the sample components, whereas some processes are based on intrinsic sample properties. As always, the optimum method will depend on the sample and the analytical task at hand.

1.3 Structure of the Thesis

Chapter 2 discusses the main physical properties of serological samples, which gives a short discussion of hemodynamic principles is beyond the scope of this thesis but in this chapter, an overview of basic principles is presented that are helpful in understanding the physical background.

Chapter 3 discusses a novel microfluidic device to observe uncovered parasitosis from serological samples. This chapter is based on work published in Springer - BioNanoScience [125] and presented at international conferences, which starts with a short introduction, represents the physical principles, and shows the results of computational fluid dynamic simulations, and the experimental tests.

Chapter 4 discusses a novel application of the deterministic lateral displacement device. This chapter starts with the description of physical principles, continues with computational fluid dynamics results and concludes with the evaluation of the experimental results using the DLD structure to separate microvesicles from serological samples. The results presented in Chapter 4 excluding the discussion on the description of principles was also published in Springer - BioNanoScience [126].

DOI:10.15774/PPKE.ITK.2015.011

Chapter 2

Hematology, Hemorheology, and Hemodynamics

2.1 Hematology

Blood (*sanguis*), wihtout doubt the most important biological fluid, performs many fundamental functions to maintain homeostasis; from transporting nutrients and oxygen to tissues and organs to regulating pH and temperature. It also provides an efficient transit system through the vascular network for transporting of immune cells as a defense against foreign microbes and wound healing. As blood contains a myriad of information about the functioning of the human body, complete blood analysis has been a primary diagnostic test in our healthcare system.

The total volume of body fluid is distributed mainly between two compartments: the extracellular fluid and the intracellular fluid. The extracellular fluid is divided into the interstitial fluid and the blood plasma. In an average 70-kilogram adult human, the total body water content is about 60 % of the body weight, or about 42 liters [127]. This percentage can change, depending on age, gender, and degree of obesity. About 28 of the 42 liters of fluid in the body are inside the 75 trillion cells and are collectively called the intracellular fluid, which is almost the 40 % of the total body weight [127]. All the fluids outside the cells are collectively called the extracellular fluid. Together these fluids account for about 20 % of the body weight, which is about 14 liters [127]. The two largest compartments of the extracellular fluid are the interstitial fluid, which makes up more than three fourths of the extracellular fluid, and the plasma, which

DOI:10.15774/PPKE.ITK.2015.011

makes up almost one fourth of the extracellular fluid, or about 3 liters.

Blood contains both extracellular fluid (the fluid in plasma) and intracellular fluid (the fluid in different blood cells). The average blood volume of adults is about 7 % of body weight, or about 5 liters [127]. The composition of the blood are cells and plasma (Table 2.1), which comprises mostly water and contains glucose, proteins, hormones, mineral ions, gases. The cells of blood (Table 2.2) present are red blood cells (called RBCs or *erythrocytes*) white blood cells (called WBCs or *leukocytes*) and platelets (PLT, *thrombocytes*).

Name	Mass concentration $[mg/dl]$	Name	Mass concentration $[mg/dl]$
Sodium	340	Calcium	10.6
Cloride	340	Lactic acid	10
Phospholipids	280	Phosphate	4.5
Cholesterol	150	Magnesium	2.3
Bicarbonate	140	Uric acid	3
Neutral fat	125	Creatinine	1.5
Glucose	100	Bilirubin	0.5
Potassium	20	Bile salts	0.5
Urea	15	Else	4.9

Table 2.1: Average mass concentration of human blood plasma constituents [127]

Name	Average cell concentration $[cells/ml]$	Approximate normal range $[cells/ml]$	Percentage of volume [%]
Erythrocytes	$4.8 \cdot 10^6$	$4.5 - 6.2 \cdot 10^6$	91
Leukocytes	$9.0 \cdot 10^3$	$4.1 - 10 \cdot 10^3$	5
Neutrophils	$5.4 \cdot 10^3$	$3.0 - 6.0 \cdot 10^3$	
Eosinophils	$2.7 \cdot 10^2$	$1.5 - 3.0 \cdot 10^2$	
Basophils	$6.0 \cdot 10^1$	$0 - 1.0 \cdot 10^1$	
Lymphocytes	$2.7 \cdot 10^3$	$1.5 - 4.0 \cdot 10^3$	
Monocytes	$5.4 \cdot 10^2$	$3.0 - 6.0 \cdot 10^3$	
Thrombocytes	$3.0 \cdot 10^5$	$1.5 - 4.0 \cdot 10^5$	4

Table 2.2: The size, percentage and the concentration of the main blood cells [128]

DOI:10.15774/PPKE.ITK.2015.011

The red blood cells are without nucleus, biconcave, disc-shaped bodies. From upper view, their shape is circular, with an average diameter of 7.5 μm. The number of RBCs is around $4.5 - 6.2 \cdot 10^9$ $particles/dl$ [129]. The red blood cells are perfectly elastic structures, flexibly deformable, thus they can pass thought much smaller capillaries than their diameter. The shape of RBCs is sensitive to osmotic variance. In hypotonic milieu (where the concentration of the salt is lower than 0.9 %) the shape of the cells change to spherical shape and after that the cells bursts and the hemoglobin flows out. In this case we get a hemolyzed solution with the hemoglobin and the membranes of the red blood cells.

The average cell concentration of leukocytes is around $4.1-10 \cdot 10^6$ $particles/dl$ [129]. White blood cells are divided into several subclasses, for example basophils, eosinophils, lymphocytes, monocytes and neutrophils. These cells have a great wealth of form and functional character.

The platelets are ovoid, round, flat disc-shaped structures. These cell fragments lack a nucleus. The diameter of the platelets is 2-4 micrometers and their number is around $1.4 - 4.2 \cdot 10^8$ $particles/dl$ [129]. The platelets are responsible for blood clotting (coagulation), by converting fibrinogen to fibrin. This creates a mesh onto which red blood cells adhere and clot, which then stops more blood from leaving the body and also helps to prevent bacteria from entering the body.

Blood performs many important functions. First of all it transports oxygen to tissues. Blood supplies the cells with nutrients such as glucose, amino acids, and fatty acids, removes waste (carbon dioxide, urea, and lactic acid). It has a messenger transport function with hormones and the signaling of tissue damage as well. The blood is supporting the body's self-repair mechanism with the coagulation functionality. White blood cells make immunological detection functions of foreign material by antibodies. The blood makes the regulation of body pH (the normal pH of blood is in the range of 7.35 - 7.45). Also, it helps in the regulation of core body temperature.

DOI:10.15774/PPKE.ITK.2015.011

2.2 Hemorheology and Hemodynamics

Hemodynamics is concerned with the mechanical and physiologic properties describing motion and equilibrium of blood flow under the action of external forces. Further, hemorheology describes the rheological properties of blood and its elements, such as morphology of blood cells and blood viscoelasticity. A full discussion of hemodynamic and hemorheology principles is beyond the scope of this thesis but in this chapter, an overview of basic principles is presented that are helpful in understanding the physical background. Blood is a non-Newtonian fluid, but in narrow microfluidic channels the flow properties of the human blood could be approximated as Newtonian [130]. Based on this assumption, the following equations describe Newtonian fluid properties and are solved with the physical parameters of human blood.

2.2.1 Velocity and Pressure Profile

The sample flow in microchannels has often been associated with negligible inertia that is, fluid flow in microfluidic channels is assumed to occur at low Reynolds number, where Reynolds number is a dimensionless parameter describing the ratio between inertial and viscous forces in a flow. The liquid flow is in stream that is considered to consist of a series of thin laminae slipping over one another, meanwhile in turbulent case the blood moves in irregular varying paths continuously mixing within channels. The description factor for stream types laminar and turbulent, which was introduced by Stokes, but measured by Reynolds, is described as:

$$Re = \frac{\rho D_H v}{\mu}, \tag{2.1}$$

which is also called Reynolds number, where ρ is the density of mass, D_H is the characteristic hydraulic diameter, v is the mean velocity of the fluid, and μ is the dynamic viscosity. In a Stokes flow regime, where $Re \to 0$, the inertia of the fluid is ignored in most microfluidic platforms and contributions of fluid momentum are omitted from the NavierStokes equations resulting in linear, and thus time-reversible, equations of motion for Newtonian fluids. Practically achievable and useful flows in microfluidic systems could operate also in intermediate range flow ($\sim 1 <$Re$<\sim 100$) in which nonlinear and irreversible motions are observed for fluid and particles. The intermediate range flow regime, in which both the inertia and the viscosity of the fluid are finite,

DOI:10.15774/PPKE.ITK.2015.011

still lies within the realm of laminar flow which provides a deterministic nature and thus controllability of fluid and particles within. In the consideration of our application for blood with density of 1060 kg/m^3, shear viscosity of $3.53 \cdot 10^{-3}$ Pas, the range of Reynolds number is shown in Fig. 2.1.

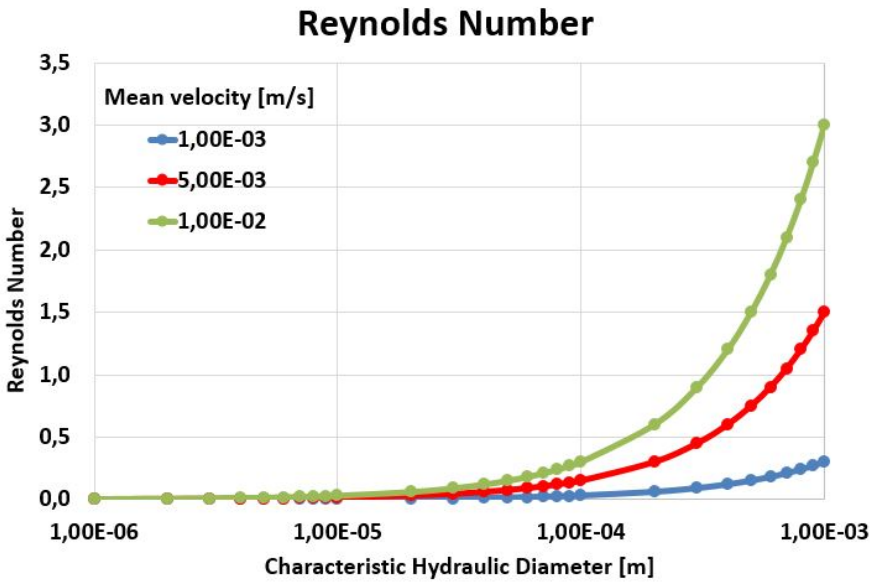

Figure 2.1: The Reynolds number of blood flow ($\rho = 1060\ kg/m^3$ and $\mu = 3.53 \cdot 10^{-3}\ Pas$) is calculated at different velocities (1 mm/s, 5 mm/s, and 10 mm/s) assuming Newtonian flow behavior at different characteristic hydraulic diameters (log scale).

For cases of low Reynolds number, neglecting inertia by using a Stokes flow approximation can lead to incorrect results. To determine exactly the velocity and the pressure profile in a microfluidic channel, incompressible Navier-Stokes equation is applied assuming constant viscosity (μ). The Navier-Stokes equation is derived from the basic laws of conservation of mass, momentum and energy in the following way:

$$\frac{\delta \vec{\mathbf{v}}}{\delta t} + \vec{\mathbf{v}} \cdot \nabla \vec{\mathbf{v}} = -\nabla P + \nu \nabla^2 \vec{\mathbf{v}} + F, \tag{2.2}$$

where $\vec{\mathbf{v}}$ is the velocity vector, P is the pressure and F is the sum of external body forces (e.g. gravity, electrophoretic forces, magnetophoretic forces, mechanical forces (i.e. ultrasound) and optophoretic forces).

DOI:10.15774/PPKE.ITK.2015.011

2.2.2 Energy Conservation

Assuming no friction inside the flow, Bernoulli's equation can be derived from the Navier-Stokes equation (Eq. 2.2). Bernoulli's principle (conservation of energy) states that for an inviscid flow, an increase in the speed of the fluid occurs proportionally with an increase in both its dynamic pressure and kinetic energy, and a decrease in its static pressure and potential energy, which can be described in the following way:

$$\frac{\Delta P}{\rho} + \frac{v^2}{2} + a_{grav} h = 0, \tag{2.3}$$

where ΔP is the pressure drop, a_{grav} is the gravitational acceleration and h is height of fluid. This states that, in a steady flow, the sum of all forms of mechanical energy in a fluid along a stream is the same at all points on that stream, thus this requires that the sum of kinetic energy and potential energy remains constant.

2.2.3 Volumetric Flow Rate and Hydrodynamic Resistivity

One of the properties of a fluid is that it will flow from a region of higher pressure toward a region of lower pressure. The primary parameter used in lab-on-a-chip devices to describe blood flow is the flow rate, which is the total volume of liquid pumped through the channel in a given time interval. The relationship between blood flow, resistance, and pressure in cylindric channels can be determined using the Hagen-Poiseuille law:

$$Q = \frac{\Delta P \pi r^4}{8 \mu L}, \tag{2.4}$$

where Q is the flow rate, ΔP is the pressure gradient, r is the radius of channel, μ is the viscosity of fluid (in our case: blood), L is the length of channel. The flow resistance can be considered in the following representation:

$$R = \frac{\mu L}{8 \pi {D_H}^4}, \tag{2.5}$$

where D_H is the hydraulic diameter. Generally, the length of microfluidic channels is in millimeter scale while the hydraulic diameter, which is a commonly used term when handling flow is well bellow the millimeter scale in noncircular tubes or channels, and is defined by:

$$D_H = \frac{4A}{B}, \tag{2.6}$$

DOI:10.15774/PPKE.ITK.2015.011

where A is the cross sectional area and B is the wetted perimeter. The microfluidic channels that are generally used in microfarication have a rectangular cross-section, in which case the hydraulic diameter (D_H) can be considered in the following way:

$$D_H = \frac{2wh}{w+h}, \tag{2.7}$$

where w is the width ($w \approx 100\mu m$) and h is the height ($h \approx 20\mu m$) of our designs thus the typical value of the hydraulic diameter is around $33\mu m$. According to Eq. 2.4 the flow rate Q, which is determined by the pressure gradient, radius of channel, viscosity of fluid and length of the channel, is inversely proportional to the fluid resistance (Eq. 2.5) and it can be described as:

$$Q = \frac{\Delta P}{R}. \tag{2.8}$$

In this case Eq. 2.4 can be considered analogous to Ohm's law, hence the flow rate is inversely proportional to the resistance. The walls of the microfluidic channels are considered as rigid thus the Hagen-Poiseuille law is applicable. If we consider a 1 mm long straight microchannel with 20 μm depth and the width from 10 μm up to 300 μm the order of magnitude of flow resistance of blood flow is between $10^{10} - 10^{12}$ Pas/m^3, meanwhile the total pressure drop is in the range from a few kPa up to 100 kPa.

2.2.4 Kinematic Properties

In microfluidic channels, the flow is usually smooth and orderly because the fluid separates into an infinite number of concentric layers with different velocities. When a fluid (in our case: blood) flows past a solid surface, a thin layer develops adjacent to the surface where frictional forces retard the motion of the fluid. There is a gradient of frictional resistance between fluid in contact with the solid surface and fluid in the center of the stream. If the fluid particles travel along well-ordered nonintersecting layers, this is termed laminar flow. In a small Reynolds number case, the floating particles are moved by the fluid through a viscous Stokes drag and their trajectories are $X_p(t)$ [131]:

$$\frac{dX_p}{dt} = V_p, \tag{2.9}$$

$$\frac{dV_p}{dt} = -\frac{1}{\tau_p}\left[V_p - v(X_p, t)\right] + g, \tag{2.10}$$

DOI:10.15774/PPKE.ITK.2015.011

where g is the acceleration of gravity, τ_p is the relaxation time of the particle, which is:

$$\tau_p = \frac{2\rho_p r_{particle}^2}{9\mu}, \tag{2.11}$$

where ρ_p is the mass density of the particle and $r_{particle}$ is the radius of the particle. The fluid velocity at the location of the particles is evaluated by linear interpolation. The inertia of the particle becomes dominant at higher velocities or masses.

Physical property	Blood	Water [132]	Dimension
Density (ρ)	$1.06 \cdot 10^3$ [133]	$1.0 \cdot 10^3$	$[kg/m^3]$
Shear viscosity (μ)	$3.53 \cdot 10^{-3}$ [134]	$1.0 \cdot 10^{-3}$	$[Pas]$
Kinematic viscosity (ν)	$3.33 \cdot 10^{-6}$ [135]	$1.0 \cdot 10^{-6}$	$[m^2/s]$
Surface tension (in air) (γ)	$5.8 \cdot 10^{-2}$ [136]	$7.3 \cdot 10^{-2}$	$[kg/s^2]$
pH	7.35-7.45 [137]	7	
hematocrit	45.7 [138]		[%]

Table 2.3: Physical properties of human blood (at $37°C$) and water (at $20°C$) at 1 atm pressure

There are dimensionless numbers that provide information about the qualitative behavior of flow in a continuous single-phase liquid. The Reynolds number (Re) determines the inertial effect of fluid flow (turbulency), and the Péclet number (Pe) describes the mass transport contribution of molecules or particles (dispersion). The particle Reynolds number (Re_p) shows the inertial effect on a particle within a fluid flow, and the Stokes number (St) is useful to study the trajectory mismatch between the particle and fluid, and the size-based separation effect.

The particle Reynolds number (Re_p) can be defined as follows from [139] and is represented in Fig. 2.2:

$$Re_p = \frac{\rho v_{max} d_{particle}^2}{\mu D_H} = Re \frac{d_{particle}^2}{D_H^2}, \tag{2.12}$$

where Re is the Reynolds number, $d_{particle}$ is the particle diameter, v_{max} is the maximum flow velocity and μ is the shear viscosity (in our case, blood at $3.53 \cdot 10^{-3}$ Pas).

In case of mass transport, the particle motion can be estimated by the Péclet number:

$$Pe = \frac{v_{mean} D_H}{D}, \tag{2.13}$$

DOI:10.15774/PPKE.ITK.2015.011

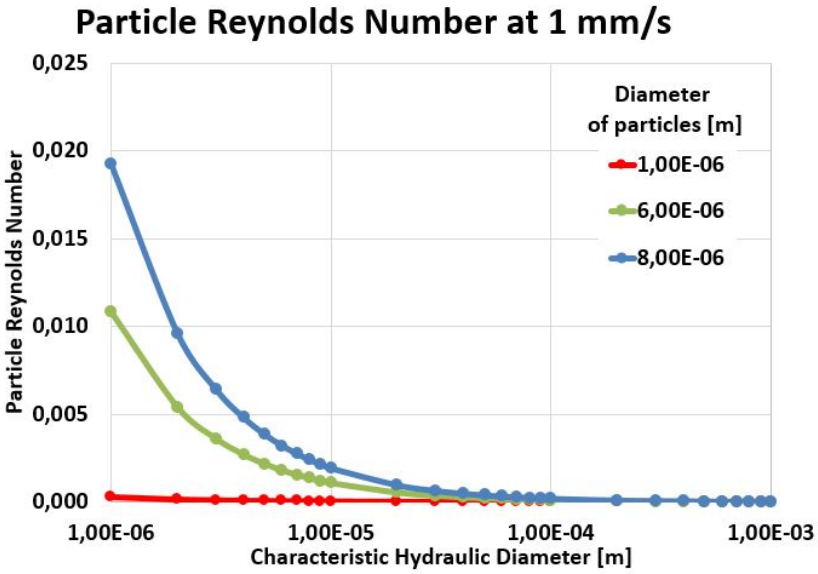

Figure 2.2: Particle Reynolds number of different size particles (1 μm, 5 μm, and 8 μm) at different characteristic hydraulic diameter (log scale) at 1 mm/s flow rate within blood ($\rho = 1060\ kg/m^3$ and $\mu = 3.53 \cdot 10^{-3}\ Pas$).

where v_{mean} is the mean velocity of the fluid (in our case, $v \approx 1.0 \cdot 10^{-2}\ m/s$) and D is the diffusion coefficient of particles. The diffusion coefficient of the particles is described by the Stokes-Einstein equation:

$$D = \frac{k_B T}{6\pi\mu r_{particle}}, \tag{2.14}$$

where k_B is Boltzmann's constant ($1.38 \cdot 10^{-23}\ J/K$), T is the absolute temperature (in our case: 298 K), and $r_{particle}$ is the radius of a spherical particle. In consideration of blood cells, the shape of the particles are not perfectly round and rigid but in these models blood cells can be approximated using perfect spherical particles. If Pe>1 the advection rate is bigger than the diffusion rate thus the particles are basically confined to streams. When a particle encounters an accelerating flow in a nonlinear channel, the Stokes number estimates the particle behavior as the ratio of the relaxation time of the particle (τ_p) (eq. 2.11) to the characteristic time of the flow (τ_f):

$$St = \frac{\tau_p}{\tau_f} = \frac{2\rho_p r_{particle}^2/9\mu}{D_H/v_{max}} = \frac{\rho_p}{18\rho} Re_p, \tag{2.15}$$

where v_{max} is the maximum fluid velocity well away from the obstacle, ρ_p and ρ are the particle density and fluid density.

DOI:10.15774/PPKE.ITK.2015.011

If St>1, a particle will continue in its original direction of movement instead of following the fluid stream when the flow turns suddenly due to the channel geometry. The Péclet and the Stokes number of the main blood components at 0.001 m/s flow rates are demonstrated in Fig. 2.3 and in Fig. 2.4.

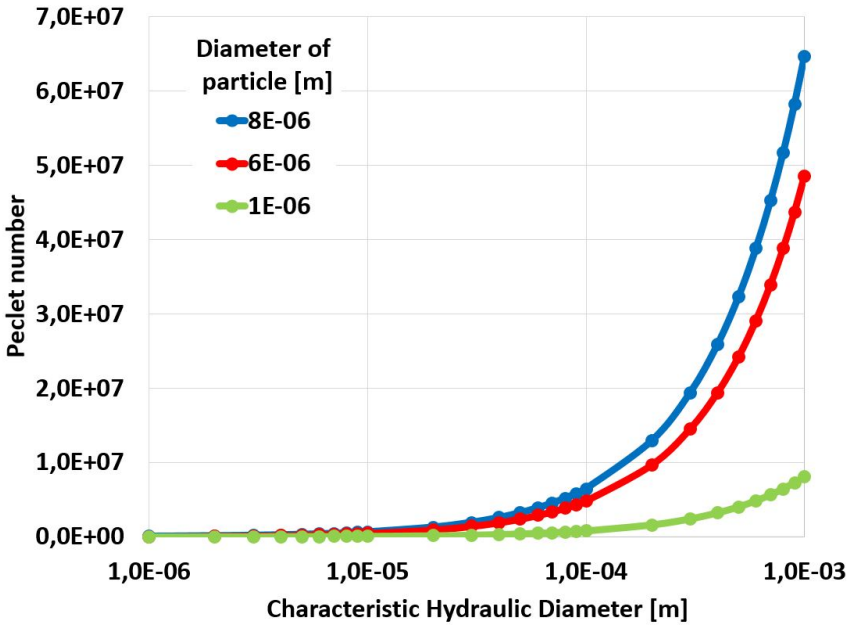

Figure 2.3: Peclet number of different size particles (1 μm, 5 μm, and 8 μm) at 1 mm/s flow rate within the blood ($\rho = 1060\ kg/m^3$ and $\mu = 3.53 \cdot 10^{-3}\ Pas$)at different characteristic hydraulic diameters (log scale) using a Newtonian fluid approximation of blood.

2.2.5 Effects of Viscoelasticity

Since blood is a non-Newtonian fluid, its rheological properties depend on shear rate and the dimensions and the geometry of the conduit through which it flows. The cellular components are suspended in plasma, an aqueous solution that generally follows Newtonian dynamics. Since flow resistance is affected in many pathological conditions, quantitative approaches have been proposed to characterize the complex rheological properties of blood. Blood cells suspended in plasma will deform due to the interactions with the surrounding fluid and walls, described by viscous stress tensor (τ) this results in a gradual deformation over time. The rate of shear, also called velocity gradient, is caused by the laminar flow along the channel where the lamellae slip on one another

DOI:10.15774/PPKE.ITK.2015.011

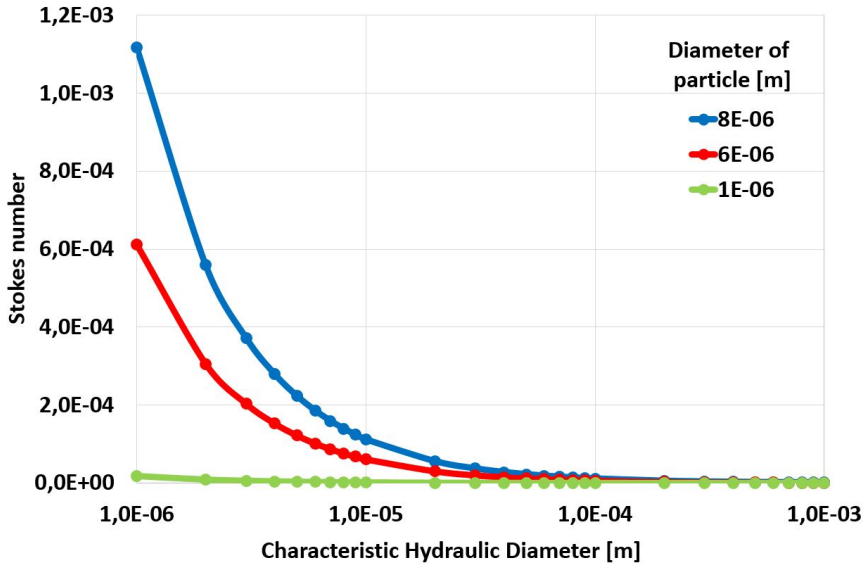

Figure 2.4: Stokes number of different size particles (1 μm, 5 μm, and 8 μm) at 1 mm/s flow rate within the blood ($\rho = 1060\ kg/m^3$ and $\mu = 3.53 \cdot 10^{-3}\ Pas$)at different characteristic hydraulic diameters (log scale) using a Newtonian fluid approximation of blood.

and move at different speeds perpendicular to the wall. If the ratio between shear stress and rate of shear strain is linear the fluid is considered Newtonian fluid. For an incompressible and isotropic Newtonian fluid, the viscous stress is related to the strain rate by the simpler equation:

$$\tau = \mu \frac{\delta v}{\delta y}, \tag{2.16}$$

where $\delta v/\delta y$ is the derivative of the velocity component that is parallel to the direction of shear, relative to the displacement in the perpendicular direction. In application the liquid flow, which is vertebrate blood, is composed of blood cells suspended in blood plasma. The plasma, which constitutes 55 % of blood fluid, is an aqueous solution containing 92 % water, proteins, dissolved nutrients (amino acids, fatty acids and glucose), waste products (carbon dioxide, urea, lactic acid) [129]. Regarding viscosity, the intravenous blood cannot be considered a perfect Newtonian liquid due to blood cells, but the plasma. Viscoelasticity is a property of human blood that is primarily due to the elastic energy that is stored in the deformation of red blood cells as the heart pumps the blood through the body. The energy transferred to the blood by the pressure-driven flow is partially stored in the elastic structure, another part is dissipated by viscosity, and the remaining energy is stored in the kinetic motion of the blood.

DOI:10.15774/PPKE.ITK.2015.011

In Poiseuille flow, blood cells and plasma do not travel at the same average velocity. This results in differences in microchannels and discharge hematocrits. Although Eq. 2.4 is only valid for Newtonian fluids, fitting experimental data to this equation ($Q = \frac{\Delta P \pi r_{tube}^4}{8\mu_e L}$) provides a convenient method of characterizing flow resistance by the effective viscosity (μ_e), which depends on the fluid being tested, the capillary diameter, and the flow rate (or pressure drop) [140]. At high shear rates blood cells occupy the central axis of microfluidic channels leaving the cell-free zone of plasma periphery. A decrease in hematocrit tends to increase shear stress due to the decreased effective viscosity (μ_e). The normal value of hematocrit is $40-45$ % for men, meanwhile $35-40$ % for women, which is approximately three times more than that of water. The Fåhræus-Lindquist effect [130] describes the relation between the effective viscosity (μ_e) and the radius of capillary tubes (r_{tube}). According to experimental observation of Fåhræus et al. the relative viscosity of blood decreases inversely to the diameter of channels due to the erythrocytes move over the center of the channel, leaving plasma at the wall of the microchannels and the hematocrit in the channel was always less than the hematocrit in the original sample. The ratio of these two hematocrits, the tube relative hematocrit (H_R):

$$H_R = \frac{hematocrit_{channel}}{hematocrit_{sample}}, \tag{2.17}$$

where $hematocrit_{channel}$ is defined as the ratio of blood cells volume within the channel to the total volume of the sample.

In the following chapters and discussions we consider a Newtonian approximation of blood flow under the assumption that most of our microfluidic channels are at the similar hydraulic range, and the flow velocities also are considered within a small variation of a certain range. This simplification is especially necessary when conducting numerical calculations where the implementation of non-newtonian fluid dynamics could render the already complex models insolvable.

DOI:10.15774/PPKE.ITK.2015.011

Chapter 3

Flow Through Nematodes Filter

3.1 Filtration of Nematodes Using an Integrated Microcapillary System

3.1.1 Motivation, description of the problem to be solved

The filarial nematodes are a group of arthropod-borne worms that reside in the subcutaneous tissues, deep connective tissues, lymphatic system, or body cavities of humans. Some adult filarial worms can survive in the human host for many years, causing a number of chronic and debilitating symptoms, including inflammatory reactions [141]. The female worms produce large numbers of larvae called microfilariae, which are highly motile, threadlike prelarvae that in some species maintain the egg membrane as a sheath; these are called sheathed forms, while those that rupture the egg membrane are called unsheathed forms. Once released by the female worm, microfilariae can be detected in the peripheral blood or cutaneous tissues, depending on the species. The microfilariae, which may survive for 1 to 2 years, are not infective for other vertebrate hosts, nor do they undergo any further development in the vertebrate host [141]. The infections are transmitted to humans by the bites of obligate blood-sucking arthropods that had become infected through ingesting larvae (microfilariae) contained in a blood meal obtained from a mammalian host. The most speared filarial species in which the human is the definitive host is summed in Tab. 3.1.

Disease-specific immunodiagnostic and molecular testing markets increase worldwide. The genus *Dirofilaria*, which includes etiologic agents such as *Dirofilaria immitis*

DOI:10.15774/PPKE.ITK.2015.011

Species	Distribution	Vector	Location
Wuchereria bancrofti	Tropics and subtropics worldwide; mainly India, China, Indonesia, Eastern Pacific	Mosquito	Lymphatic
Brugia malayi	Southeast Asia, Indonesia, India, Indonesia, Southeast Asia	Mosquito	Lymphatic
Brugia timori	Islands of Timor and Lesser Sunda in Indonesia	Mosquito	Lymphatic
Loa loa	Africa	Deerfly	Subcutaneous
Mansonella perstans	South and Central America, Africa	Biting midge	Body cavities, mesentery, perirenal
Mansonella ozzardi	South and Central America, Caribbean	Biting midge, blackfly	Subcutaneous, body cavities
Mansonella streptocerca	West and Central Africa	Biting midge	Subcutaneous
Onchocerca volvulus	South and Central America, Africa	Blackfly	Subcutaneous
Dirofilaria immitis	Japan, Australia, United States, Europe	Mosquito	Pulmonary nodules
Dirofilaria repens	United States, Africa, Asia, Europe, and South America	Mosquito	Subcutaneous

Table 3.1: Listing of human filariasis by Gracia et al. [141]

and *Dirofilaria repens*, is responsible for the increased occurrence of zoonotic dirofilariosis in vertebrates worldwide. Human infections by these parasites may also occur, and 1782 cases have been reported in over 37 countries in Europe, North America, Southeast Asia, and Africa [142–144], 372 of which were pulmonary and 1410 of which were subcutaneous/ocular cases over the last decade [145]. Increased -travel, pesticide -restrictions, and the introduction of the Asian tiger mosquito, which take a blood -meal that is twice as large as the common mosquito species, have contributed to the spread of cardiopulmonary and subcutaneous dirofilariosis in final host carnivores [146].

DOI:10.15774/PPKE.ITK.2015.011

3.1 Filtration of Nematodes Using an Integrated Microcapillary System

The life cycle of species of *Dirofilaria* genus consists of larval stages (L1-L3) in arthropod intermediate host as vector (mosquito), developing stages (L3-L5) and adult stage in natural host (Fig. 3.1). The development period of the microfilariae mostly depends on the temperature inside the species of intermediate host (from 10 to 21 days at around $25°C$). In infective stage, the larvae (L3) migrate to the Malpighian tubule lumen of the mosquito, while during subsequent nutrition of the intermediate host the larvae enter to subcutaneous connective tissue of definitive host. In this stage (L3), the infective larvae of these filarioidea invade a variety of human or animal tissues and elicit little or no discernible response from the host during the course of their development unless they enter exquisitely sensitive tissues such as the conjunctivae. The *D. immitis* and *D. repens*, which are responsible in human, persist for months without a detectable host response. In their natural hosts, filarioids are typically long-lived, living often several years or more [147]. *D. immitis* infective larvae (L3s), commonly called "heartworm", cause a chronic infection in the right heart/inferior vena cava, and the pulmonary vein where uncontrolled parasite development may result in serious disease for the natural host but in humans do not survive their migration in subcutaneous tissue [148]. *D. repens* causes chronic infection where parasite development is limited within the eye, subcutaneous tissues, abdominal cavities, and urinary bladder. Species of *Dirofilaria* affect mostly dogs and other carnivores such as cats, wolves, and foxes. Humans may become infected as aberrant hosts, the worms fail to reach adult stage while residing in a human body.

The late stage (L4-L5) differential diagnosis of human pulmonary dirofilariosis costs $80,000 or more per patient in the USA [160]. In addition, in the case of *D. immitis*, it exposes the patient to unnecessary surgery which carries a risk of mortality. Therefore, the early-stage (L3) diagnostic techniques reduce risk of complications and also save health care costs. Large scale screening for dirofilariosis involves the use of the serologically based antigen or antibody lateral flow devices which are commercially available for this purpose: VetScan Canine Heartworm Rapid Test Kit (Abaxis, Union City, CA, USA), Heartworm IC (Argolabo S.p.A., Scarmagno, TO, Italy), Solo Step CH Canine Heartworm Antigen Test (Heska, Loveland, CO, USA), FASTest HW Antigen (Megacor Diagnostik GmbH, Hoerbranz, Austria), CH9705/FX Immunochromatographic device (Multimage S.r.l., Cavaria, VA, Italy), Woodley InSight Heartworm Rapid Diagnostic

DOI:10.15774/PPKE.ITK.2015.011

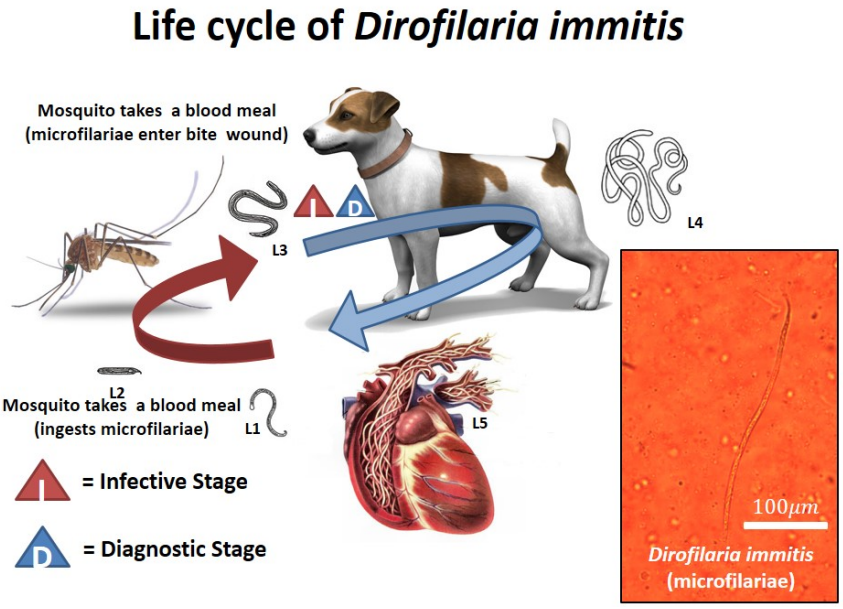

Figure 3.1: The life cycle of *Dirofilaria immitis* which consists of three stages (L1-L3) in arthropod (mosquito) intermediate vector and other two stages (L4 and L5) in vertebrate host. During the blood meal, an infected mosquito introduces L3 filarioid larvae of *D. immitis* into the skin of the definitive host. The L3 nematodes invade the tissues of natural host undergoing themselves two more molts into adults. Adult heartworms reside in pulmonary arteries and are occasionally found in the right ventricle of the heart. Adult females are usually $250 - 310$ mm long by 1 mm wide; males are usually $120 - 200$ mm long by $0.7 - 0.9$ mm wide. Adults can live for $5 - 10$ years. In the heart, the female worms are capable of producing microfilariae over their lifespan, which are $290 - 330$ μm long and $5 - 7$ μm wide [149]. The microfilariae are found in peripheral blood, which can be ingested by another mosquito during its blood meal.

Test (Woodley Equipment Company Ltd, Horwich, UK), and Canine Heartworm Antigen Test (SA Scientific, San Antonio, TX, USA). These antigen or antibody lateral flow devices require at least three adult female heartworms and do not exist for detection of *D. repens*. The antigen presence of dirofilariosis does not occur in each case thus in diagnostics several seroepidemiological methods have been developed to explore the existence of intravenous nematodes or to determine its volumetric population from blood samples. The gold standard in diagnosis depends upon microscopical detection of microfilariae in blood but classical microbiological test is also used. This is very difficult in dirofilariosis where the parasitemia is frequently below 100 nematodes per

DOI:10.15774/PPKE.ITK.2015.011

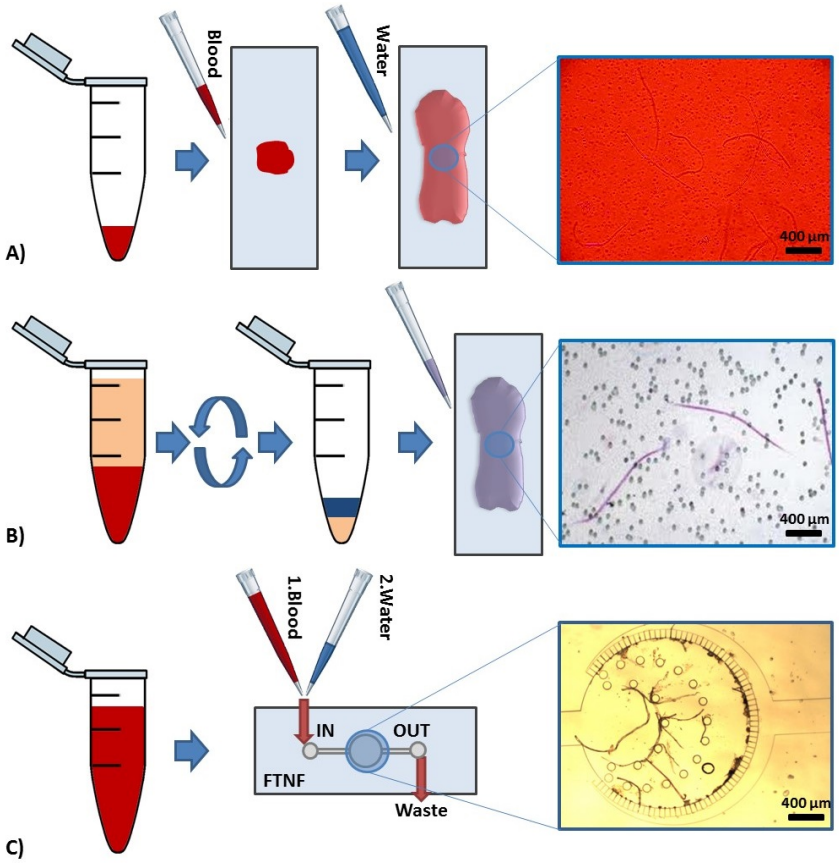

Figure 3.2: Comparison of detection and diagnostic methods and protocols for dirofilariosis including the proposed simple use FTNF device. A) Blood smear test. Starts with pipetting a drop of serological sample on a glass slide, then hemolyzing with deionized water and finally counting the number of nematodes within the all volume of sample. B) The modified Knott′s test. Anticoagulant blood sample is dissolved 2% formalin in a conical centrifuge tube. After the 5 minutes centrifugation at 1500 *rpm*, the sediment is mixed by one drop of methylene blue stain coloring the cuticle of nematodes. Finally, the number of nematodes is counted optically. C) Flow-through nematode filter (FTNF). Concentrates the nematodes in the center of the device before the hemolysis from a few *ml* of blood offering an instantaneous readout.

milliliter of blood. Given the low abundance of parasites in the blood, methods have been developed to raise the efficiency of detection rising the cost and the required time of diagnosis. The following enumeration, which is also summarized in Table 3.2, represents a scale of executive complexity in inverse proportion of currently used diagnostic methods [146]: serologic methods (fresh blood smear and histochemical stain based

DOI:10.15774/PPKE.ITK.2015.011

Method	Limit of detection	Volume requirement	Duration	References
Serologic methods (fresh blood smear, histochemical stain based tests)	1-2 nematodes	0.5-1 ml	10-30 min	[146, 150]
Concentration methods (Knott's test, hematocrit method, filter test)	1-2 nematodes	2-3 ml	20-40 min	[151, 152]
Enzyme-linked immunosorbent assays (ELISAs)	22-43 kDa antigens	200-400 μl	2-4 h	[153–156]
PCR amplification	2-3 DNS	10-100 μl	3-5 h	[142, 157–159]

Table 3.2: Laboratory diagnostics of blood-borne parasitic diseases

tests), concentration methods (Knott's test, hematocrit method, filter test), enzyme-linked immunosorbent assays (ELISAs), multiplex real-time PCR amplification. When dirofilariosis is diagnosed, the erratic progression of many infections and the lack of microfilariae in most cases necessitate the use of combined diagnostic techniques. The evaluation of serological methods and the concentration procedures are based on optical detection while the enzyme-linked immunosorbent assays (ELISAs) and RT-PCR amplification requires further costs (instruments, higher skilled labor). Each diagnostic technique is multiplexable and combinable with other methods. The most widespread technique is the smear test, which is shown in Fig. 3.2.A and starts with pipetting serological sample onto a glass slide after the hemolysis, the nematodes are counted. The modified Knott's test, which concentrates nematodes by centrifugation and mark specific species by Giemsa stain and shown in Fig. 3.2.B. First, the anticoagulant blood sample is dissolved 2% formalin in a conical centrifuge tube. After the 5 minutes centrifugation at 1500 *rpm*, the sediment is mixed by one drop of methylene blue stain coloring the cuticle of nematodes to distinguish better the different nematode spices. Finally, the number of nematodes is counted as is the previous method. The advantage of the concentration method versus the basic serologic methods is the raised detection limit from a bigger sample volume.

DOI:10.15774/PPKE.ITK.2015.011

3.1 Filtration of Nematodes Using an Integrated Microcapillary System

I have designed a microfluidic device, called flow-through nematode filter (FTNF), which is shown in Fig. 3.2.C. This device uses an integrated filtering technique providing the ability to detect much smaller concentration of nematodes from specimens, determine them more accurately and specifically without any external devices reducing the price of the measurement retaining an similar efficiency. The developed diagnostic device integrates a special, microfluidic filter to concentrate circulating parasites from serological sample.

The overall mechanism and the novelty of the device is shown and highlighted in Fig. 3.2 and in Fig. 3.3. The designed microfluidic device contains a particle separation technique which is easy to implement in cheap disposable plastic chips, that we believe is well suited for the task of removing parasites from a few *ml* of blood in order to aid the instantaneous filtration. The mechanism of separation by FTNF is based on the interaction of nematodes suspended in whole blood with an ordered array of microcapillaries and micropillars that the fluid is forced to flow through under low Reynolds number conditions, while the detectable larvae are trapped.

The required filtration range of the designed device for nematode filtration comes from parasitology. These nematodes are ovoviviparous and the evolving unsheathed embryo (microfilariae) live in the bloodstream. The length of *D. immitis* is $330-380\ \mu m$ and their width is $5-7\ \mu m$ [149]. The microfilariae of *D. repens* is bigger, $300-360\ \mu m$ long and $6-8\ \mu m$ wide [149]. In this matter the developed structure has to be robust, efficient to filter out the desired nematodes and to reduce the risk of coagulation.

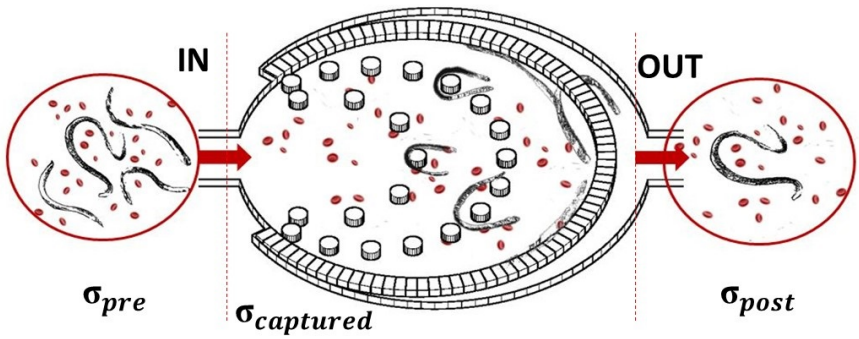

Figure 3.3: The overall mechanism of the flow through nematode filter (FTNF) device. Parasite-infected serological sample is forced through the capillary system from the inlet on the left (IN) through to the outlet on the right (OUT), meanwhile the most of the parasites remain trapped within the pillar and capillary filter system.

DOI:10.15774/PPKE.ITK.2015.011

3.1 Filtration of Nematodes Using an Integrated Microcapillary System

Here, a continuous hydrophoretic filtration technique of nematodes which does not require auxiliary liquid control, can be fabricated using a monolithic polydimethylsiloxane (PDMS)-glass technique, has been presented to construct 12 parallel microfluidic systems varying microcapillary width from 6.1 μm up to 15.4 μm. The flow-through nematode filter (FTNF), which represented in Fig. 3.3 is based on a common microfluidics-based particle filtration technique, easy to implement in cheap disposable plastic chips, that we believe is well suited for the task of removing parasites from blood in order to aid filtration. The fabrication of constructed devices are based on soft-lithography techniques using monolithic polydimethylsiloxane (PDMS).

DOI:10.15774/PPKE.ITK.2015.011

3.2 Device Principles

Figure 3.4 demonstrates the geometry of the microfluidic filter for this mentioned veterinarian purpose. Each microfluidic structure has a 400 μm wide and 20 μm high inlet and an outlet. 12 capillary structures have been implemented, which are uniform within the central region of one device but the widths of microcapillaries ($W_{capillary}$) varies from 6.1 μm up to 15.4 μm. The active zone, where parasites remain trapped is surrounded by these rectangular cross-section microcapillaries, which are on a radius (r) of 1 mm from the center and its repetition angle (α) is from 3.38° up to 3.91°. The width of obstacles/pillars (W_{pillar} = 52.8 μm) and the angle without capillary connection ($\beta = 75°$) are the same in each structure.

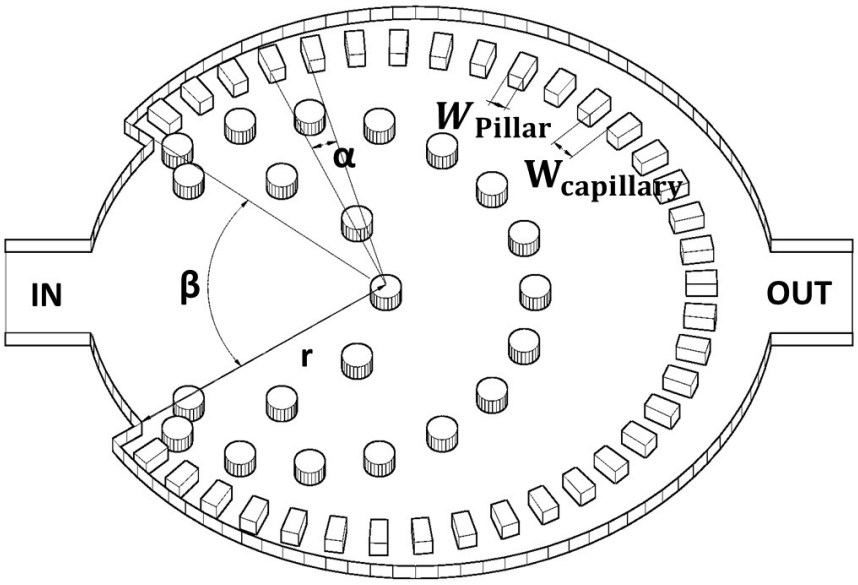

Figure 3.4: Schematic of the flow-through nematode filter. The α angle is the structural repetition of the microcapillaries, r is the radius of the active zone, W_{pillar} is the width of the pillars, $W_{capillary}$ is the width of the capillary channel and β is the angle without capillary connection. The proposed inlet and outlet channels are marked with IN and OUT, respectively. The capillaries are positioned in a circular manner to increase filtration efficiency by providing an isobaric pressure distribution along the entire filter system.

The following trigonometrical equation proximates the relationship between α and

DOI:10.15774/PPKE.ITK.2015.011

the capillary width ($W_{capillary}$):

$$\sin\frac{\alpha}{2} = \frac{W_{pillar} + W_{capillary}}{2r} \tag{3.1}$$

Those rigid particles which have greater diameter than $W_{capillary}$, will be filtered out from the liquid flow. The total cross section of microcapillaries is described by the following equation:

$$S_{capillaries} = \frac{360^\circ - \beta h}{\alpha}(2r\sin\frac{\alpha}{2} - W_{pillar}) \tag{3.2}$$

where h is the height of the channel and $360^\circ - \beta$ is that angle where the capillaries connect to the active zone.

Generally, the microfluidic filters are described by the pressure drops (ΔP) at different flow velocities and the total flow resistance (R_{tot}).

$$\Delta P = R_{tot}Q \tag{3.3}$$

The pressure drop is the function of the flow rate (Q) and the total flow resistance R_{tot} which is defined as:

$$\frac{1}{R_{tot}} = \sum_{i=1}^{n}\frac{1}{R_i} = \frac{1}{R_1} + \frac{1}{R_2} + ... + \frac{1}{R_n} \tag{3.4}$$

where n is the number of capillaries within one device ($n = (360^\circ - \beta)/\alpha$). R_i is the flow resistance of one capillary channel

$$R_i = \frac{8\mu L}{\pi r_H^4} \tag{3.5}$$

where μ is the dynamic viscosity, L is the length of the microcapillary and the nominal hydrodynamic diameter (r_H) is

$$r_H = \frac{hW_{capillary}}{h + W_{capillary}} \tag{3.6}$$

Integrating Eq. 3.4, Eq. 3.5 and Eq. 3.6 into Eq. 3.3 we get the pressure drop of cylindric-shape a capillary structure

$$\Delta P = \frac{8\mu LQ\alpha(h + W_{capillary})^4}{\pi(360^\circ\beta)h^4W_{capillary}^4} \tag{3.7}$$

DOI:10.15774/PPKE.ITK.2015.011

3.3 Computational Fluid Dynamic Simulations

The main aim of the computational fluid dynamics simulation was to design an isobaric zone in the middle of the device by predicting the flow behavior of the microfluidic device. Due to this reason, the verification of the simulation by pressure measurements were not in the scope of the thesis work. In this case, the efficiency of filtration could be increased by these results. The computational fluid dynamics simulations were calculated to predict the velocity and pressure profiles of the developed structure by COMSOL Multiphysics 4.3 (COMSOL Inc., Burlington, MA, USA). The pressure drop has a significant meaning from the point of flow through filtering. Twelve similar microfluidic devices were designed by increasing capillary width ($W_{capillary}$) from 6.1 μm up to 15.4 μm and the flow velocity and pressure profile was calculated at 0.25 ml/h, 0.5 ml/h, and 1 ml/h flow rates with the initial and boundary condition and shown in Fig. 3.5.

As it was discussed in Chapter 2, in narrow microfluidic channels the blood could be considered as Newtonian fluid thus the eq. 2.2 could be applied to determine the flow profile. The initial parameters were set to the appropriate blood properties thus the viscosity was around $3.53 \cdot 10^{-3}$ Pas, the density was 1060 kg/m^3 in the all domains of the microfluidic device. The side walls had non slipping condition, the outlet had zero-pressure and the inlet laminar inflow condition at 0.25 ml/h, 0.5 ml/h, and 1 ml/h volumetric flow rates. To investigate the efficiency of filtration the pressure drop has an important effect. If the pressure drop is significant the trapped elastic particles, which are larger than the capillary width ($W_{capillary}$) can be squeezed through the microcapillary structure while using an abnormal pressure the filter can be also destroyed [161].

For each geometry the flow velocity and pressure profiles have been calculated and the maximum pressure differences within the devices are shown in Fig. 3.6. The pressure field has a maximum value on the sidewall of inlet and the smallest value appears on the sidewall of outlet. Within one device the pressure drop rises as a laminar way in the function of flow rate and is reduced by the capillary width at the same boundary and initial conditions. The equidistant microcapillaries from the geometric center develop

DOI:10.15774/PPKE.ITK.2015.011

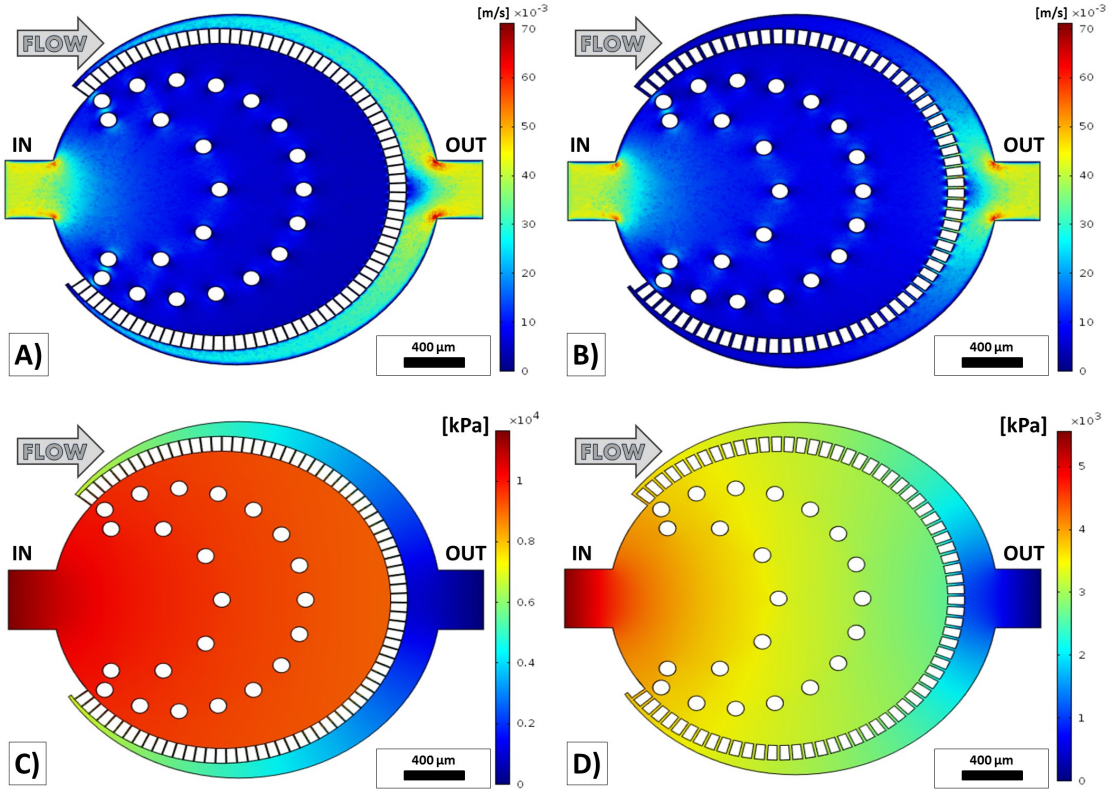

Figure 3.5: Numerical simulation results of flow velocity and pressure profiles at 1 ml/h inflow rate. A) Flow velocity profile of the thinnest ($W_{capillary} = 6.1\ \mu m$) capillary structure at 1 ml/h. B) Flow velocity profile of the thickest ($W_{capillary} = 15.4\ \mu m$) capillary structure at 1 ml/h. C) Pressure profile of the thinnest capillary structure at 1 ml/h. D) Pressure profile of the thickest capillary structure at 1 ml/h.

a quasi-homogeneous pressure field within the active zone, which is the central field of the microfluidic device, where the nematodes remain trapped, aiding the filtration of the larvae but blood cells. Based on computational flow dynamics simulations the approximation of the pressure drop can be described with the following equation with $R^2 = 0.9939$. Decreasing the capillary width ($W_{capillary}$) increases the flow resistance quasi exponentially and in the same time the pressure drop at a fixed flow rate which is represented in Fig. 3.6.

The microfluidic filters could be clogged during a long measurement, thus it could be useful to predict the incense of the pressure in the case of clogging. Figure 3.8 shows the clogging caused pressure drop in the thinnest ($W_{capillary} = 6.1\mu m$) FTNF

DOI:10.15774/PPKE.ITK.2015.011

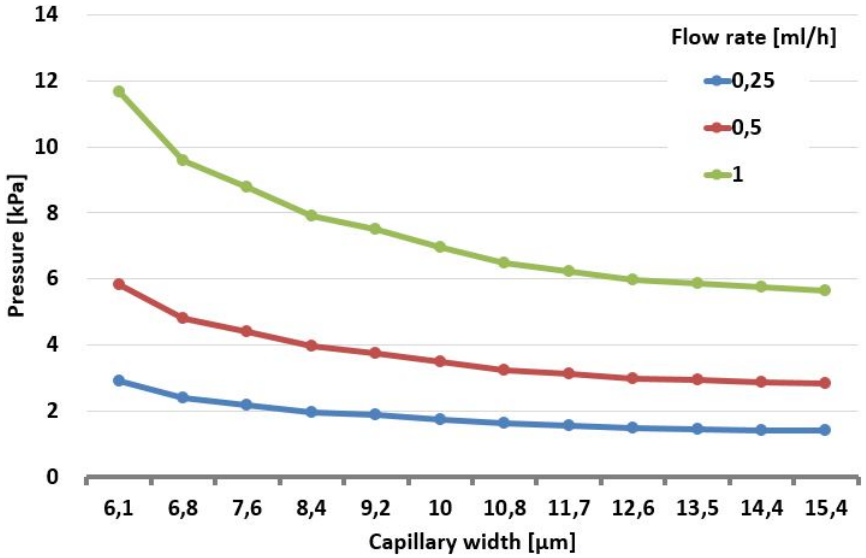

Figure 3.6: Pressure drop within each device calculated by computational fluid dynamics simulations at 0.25 ml/h, 0.5 ml/h, and 1 ml/h flow rates.

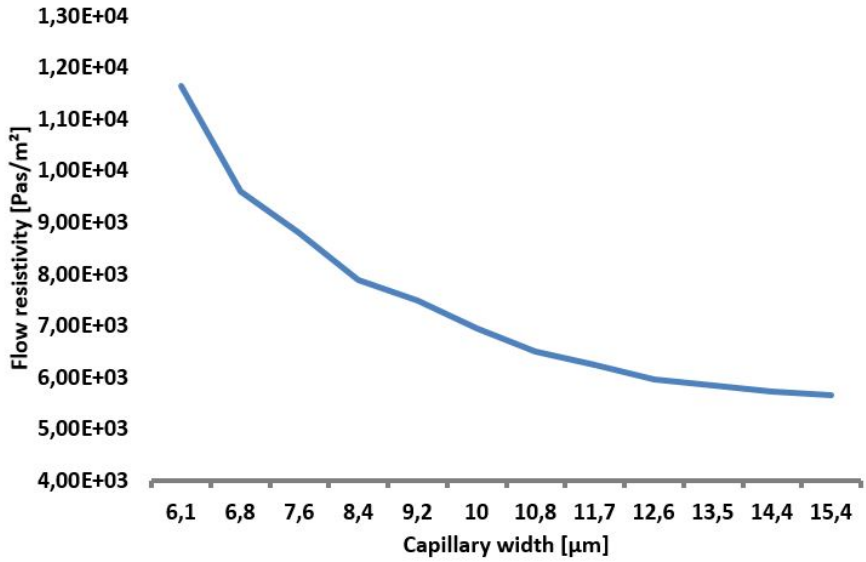

Figure 3.7: Flow resistivity within each device calculated by computational fluid dynamics simulations.

at 0.5 ml/h. The clogging effect could be significant if more than 60 percent of the channels are blocked.

DOI:10.15774/PPKE.ITK.2015.011

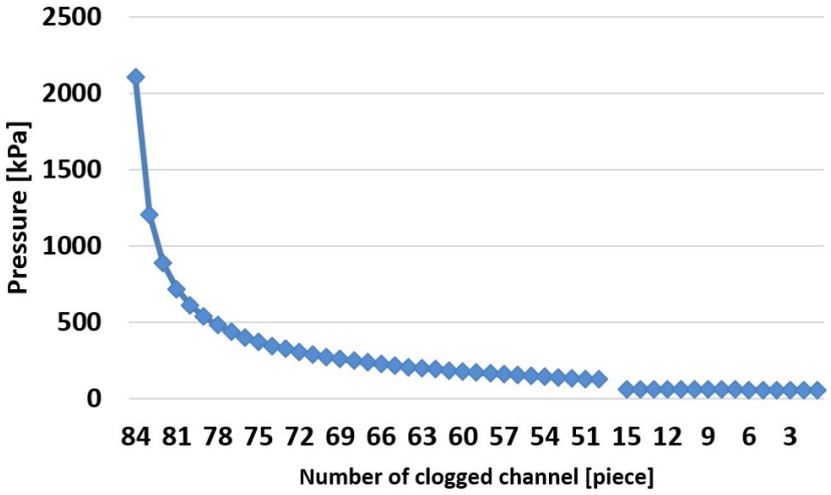

Figure 3.8: Clogging analysis of the thinnest ($W_{capillary} = 6.1\mu m$) FTNF device using computational fluid dynamics simulations at 0.5 ml/h flow rate. Closing the microcapillaries 1 by 1, the pressure drop rises.

3.4 Device Design and Fabrication

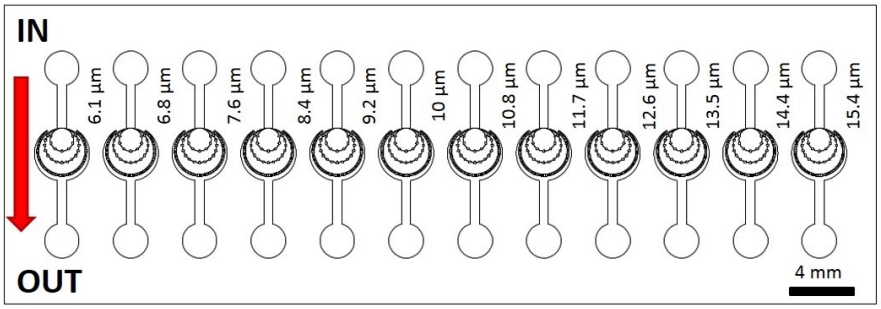

Figure 3.9: Overview of the microfluidic device, which integrate 12 different Flow Through Nematode Filters. The capillary width is between 6.1 μm and 15.4 μm.

Channel layouts were designed by using AutoCAD 2013 (Autodesk Inc., San Rafael, CA, USA), which are shown in Fig. 3.9 and devices were fabricated in polydimethylsiloxane polymer (PDMS, Sylgard 184, Dow Corning, USA) using a standard microfabrication soft-lithographic technique [161]. The microfabrication procedure starts with making a master for replica molding. SU-8 (MicroChem, Newton, MA, USA) photoresist was spin coated onto 4" silicon wafer to a thickness of 20 μm (Fig. 3.10.A) and patterned using UV light in contact mask aligner through a chrome mask (Fig. 3.10.B).

DOI:10.15774/PPKE.ITK.2015.011

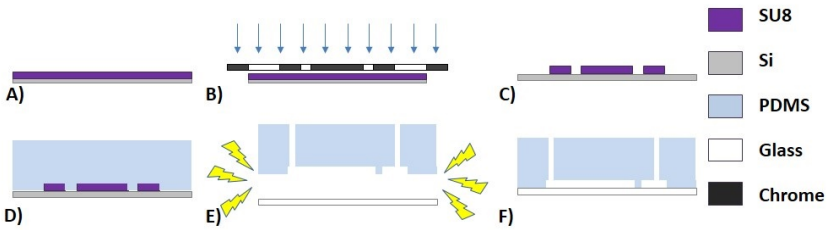

Figure 3.10: Fabrication steps of the microfluidic devices. A) SU-8 photoresist was spin coated onto silicon wafer. B) The shape of the microfluidic channels were patterned by UV light in contact mask aligner through a chrome mask. C) The unpolarized photoresist was washed away from the surface. D) The liquid PDMS pre-polymer conformed to the shape of the master. E) The patterned PDMS slab was bonded to microscope glass slide following surface treatment. F) The final device.

PDMS monomer and curing agent were mixed to a ratio of 10 : 1 (v/v), degassed and poured over the master and set aside at $70°C$ for 2 h for polymerization. The liquid PDMS pre-polymer conforms to the shape of the master and replicates the features of the master (Fig.3.10.D). After the polymerization the solid PDMS replica was pulled off from the mold surface and access holes were punched through the patterned PDMS slab using a 1 mm hollow pin vise. The patterned PDMS slab was bonded to microscope glass slide following surface treatment by Plasma-preen II 863 (Plasmatic Systems Inc. North Brunswick, NJ, USA) (Fig. 3.10.E). Finally, teflon tubes were inserted into the access holes for fluidic contacts.

3.5 Experimental Setup

Figure 3.11 illustrates the schematic diagram of our nematode filtration platform. Pressure-driven flow was created using syringe pumps (NE-4000, New Era Pumping System Inc, Farmingdale, NY, USA) attached to the inlet via Teflon tubes. Typical flow rates were used between 0.1 ml/h and 2 ml/h, controlled by the syringe pump. Imaging was performed on an inverted Olympus IX71 microscope (Olympus, Tokyo, Japan). Image recording was through a USB color CCD camera (uEye UI-222x series, IDS Imaging Development Systems GmbH, Obersulm, Germany). All videos were captured at a speed of 50 frames/second and captured videos were analyzed using Matlab (The MathWorks Inc., Novi, MI, USA). For parasitological experiments, blood-borne infected, anticoagulant, canine blood has been used, where *D. repens* parasites were

DOI:10.15774/PPKE.ITK.2015.011

determined previously by Knott's method obtaining their concentration in serological samples.

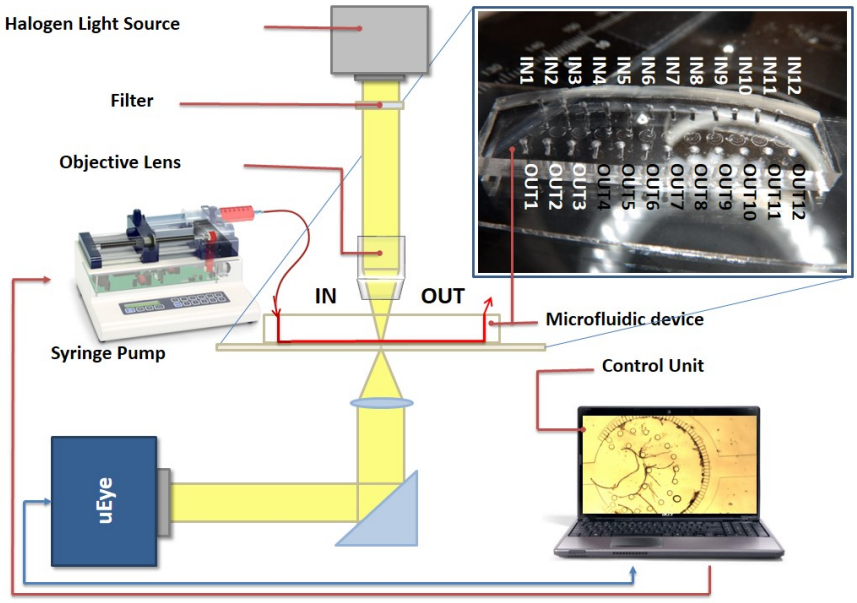

Figure 3.11: Schematic image of the parasite filtration platform. The microfluidic devices are mounted on an inverted microscope. The syringe pump system with the CCD camera unit are controlled from a single platform.

3.6 Experimental Results

The single layer microfluidic design allows the easy loading, immediate filtration and analysis of nematodes, eliminating the need of other sample preparation instruments such as centrifuge or other devices. Before each experiment, these microfluidic structures were optically checked, purified and dried eliminating unnecessary particles (dust), which can cause clogging. The developed structures were tested at 0.25 ml/h, 0.5 ml/h, and 1 ml/h volumetric flow rates by 15 different blood-borne infected, anticoagulant, canine blood samples. The type and the severity of dirofilariosis was determined and classified into three commonly used classes (-, +, ++).

Figure 3.12 shows the procedure of nematode filtration, which contains the following steps. First, the serological sample is forced through the microfluidic device at a constant volumetric flow rate during which most of the nematodes remain trapped in

DOI:10.15774/PPKE.ITK.2015.011

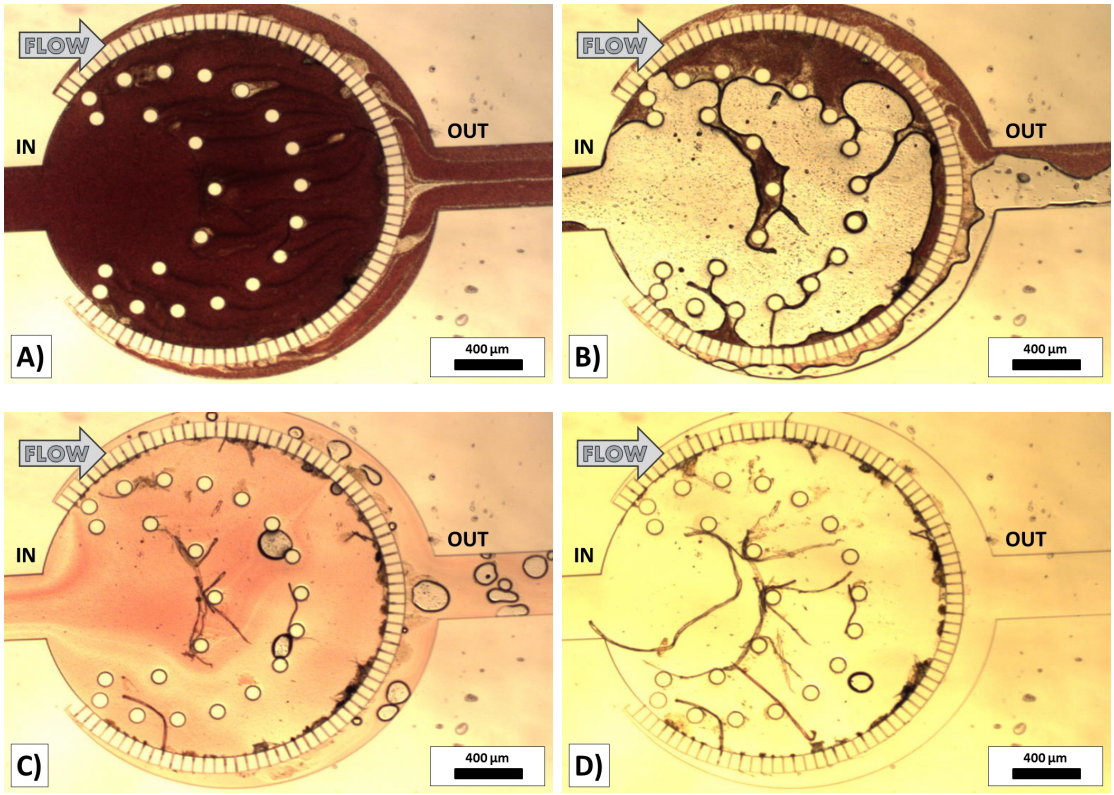

Figure 3.12: Procedure of nematode filtration. A) serological sample is forced through the microfluidic device B) the medium is changed to air then deionized water C) haemolysis and increment of visibility D) counting the nematodes optically

the isobaric central region (Fig. 3.12.A). Changing the medium to air and subsequently to deionized water, air bubble is pushed thought the capillary structure (Fig. 3.12.B). Since deionized water induces hemolysis by osmotic shock the attached and aggregated cells as thrombocytes and lymphocytes are lysed and flushed away from the detection area, while nematodes are resistant to osmotic shock due to their cuticulae this lysis increases the visibility and the contrast (Fig. 3.12.C). Finally, the trapped nematodes are counted optically in the central region (Fig. 3.12.D). Our experiments indicates that the number of trapped nematodes correlates with the applied volumetric flow rate and the microcapillary width.

Blood-borne infected, anticoagulant blood samples were pushed through the microfluidic devices and the major population of nematodes were captured in the quasi-isobaric central region (Fig. 3.4). The population of the nematodes in the original

DOI:10.15774/PPKE.ITK.2015.011

blood samples (σ_{pre} and in the waste products (σ_{post}) were analyzed by basic serologic methods (tick blood smears) to determine the efficiency of the device at different flow rates (0.25 ml/h, 0.5 ml/h, and 1 ml/h). The filtration efficiency (η), which is represented on Fig. 3.3, has been calculated by taking the amount of the trapped nematodes ($\sigma_{captured}$) and the initial number of larvae (σ_{pre}) in the native serological sample. The number of trapped nematodes ($\sigma_{captured}$) has been counted optically within the active zone. Assuming a homogenous sample the following relationship describe the nematode numbers:

$$\sigma_{pre} = \sigma_{captured} + \sigma_{post} \tag{3.8}$$

If the sample volume is fixed and concentration is homogeneous the efficiency (η) can be defined in the following way:

$$\eta = \frac{\sigma_{captured}}{\sigma_{post} + \sigma_{captured}} \tag{3.9}$$

Due to the sedimentation of the heavier particles (e.g. nematodes), inhomogeneity (IH) of the serological sample can occur at low flow rates, which can cause false prediction of the nematode population in the original sample. The inhomogeneity of the samples was defined by the following equation:

$$IH = \frac{|\sigma_{pre} - \sigma_{captured} + \sigma_{post}|}{\sigma_{pre}} = \frac{2\sigma_{post}}{\sigma_{pre}} \tag{3.10}$$

The efficiencies of the different microfluidic channels, which is presented in Fig. 3.13, have been calculated at constant volumetric flow rates (0.25 ml/h, 0.5 ml/h, and 1 ml/h) by the previously described procedure. During each measurement, one examined sample (+ or ++) was chosen and forced through 12 different FTNF structures with microcapillary width from 6.1 μm up to 15.4 μm separately at a constant flow rate five times binning efficiency (η) for histograms. The average population of the nematodes in the original blood samples (σ_{pre}) was obtained from 5 intermediate control tests at each measurement. The volumetric nematode concentration (σ_{pre}) was between $0.65 \cdot 10^3$ and $3.06 \cdot 10^3$ $nematodes/ml$). The flow velocity on the inlet determines the pressure drop though the microcapillary structure. Increasing the flow rate, the pressure drop forces more nematodes through the filter decreasing the efficiency of the filtration. On the other hand, decreasing the flow rate has an influence on

DOI:10.15774/PPKE.ITK.2015.011

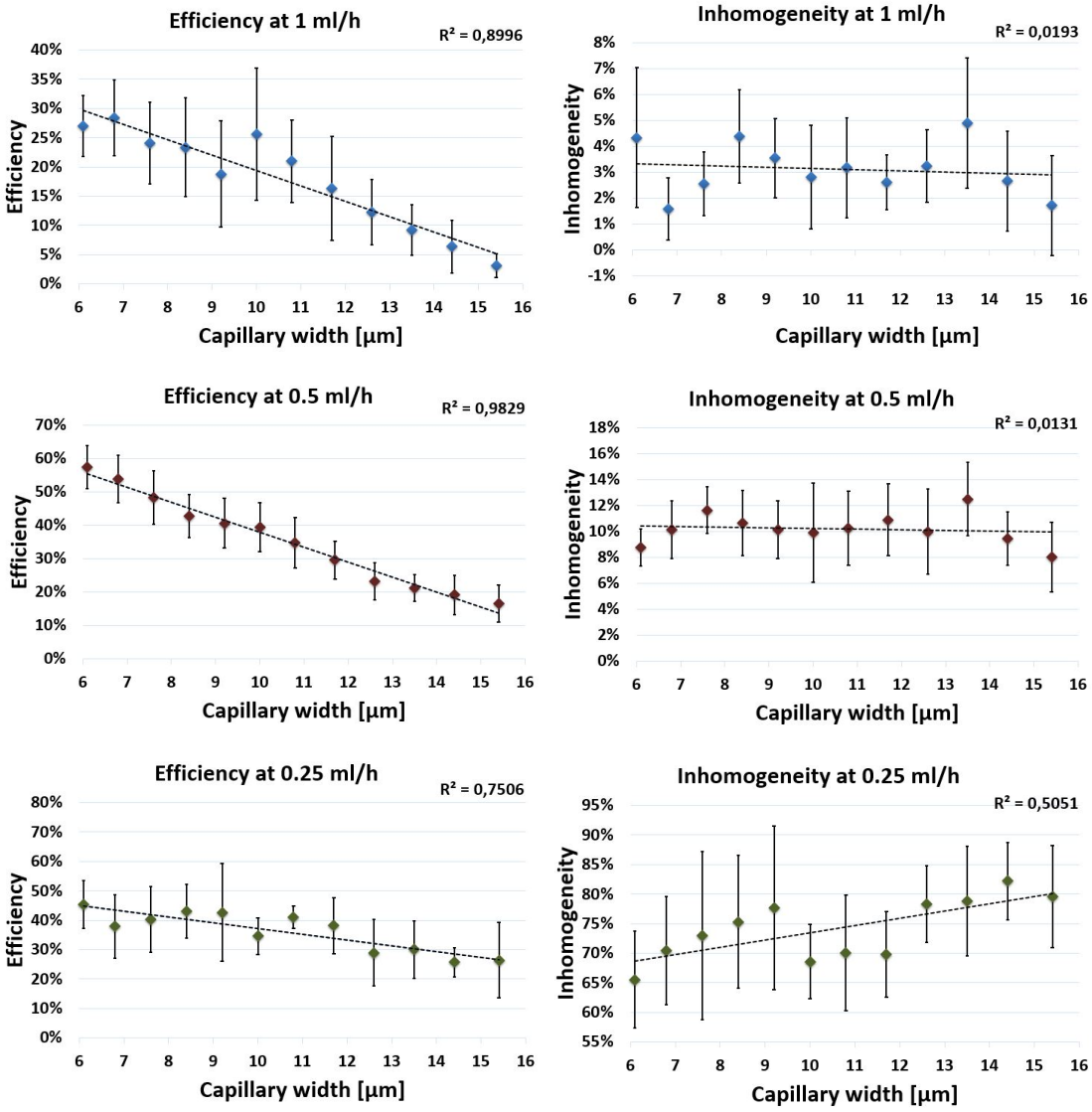

Figure 3.13: The efficiency and the inhomogeneity of each microfluidic structure ($W_{capillary}$ from 6.1 μm up to 15.4 μm) at different flow rates (0.25 ml/h, 0.5 ml/h, and 1 ml/h). The error bars of each histogram shows the standard deviations from the mean values. The R-squared values of each trendlines are displayed.

the inhomogeneity of the samples. Optimizing the applied flow rate for the described purpose, the inhomogeneity was also measured and binned for histograms. The standard deviations of the mean values of filtration efficiency and sample inhomogeneity were calculated and displayed on Fig. 3.13 with trendlines and their R-squared values.

DOI:10.15774/PPKE.ITK.2015.011

The robustness analysis of the procedure was considered by trend estimation of mean efficiencies of different devices ($W_{capillary}$ from 6.1 μm up to 15.4 μm) and their R-squared values ($R^2 = 0.8996$ at 0.25 ml/h, $R^2 = 0.9829$ at 0.5 ml/h and $R^2 = 0.7506$ at 1 ml/h). The highest mean efficiency of filtration was obtained at 0.5 ml/h flow velocity with the best trend fit. Based on the measurements, we found that increasing flow rate increases the level and the stability of sample homogeneity. By decreasing the capillary width ($W_{capillary}$) the filtration efficiency is increased but applying a higher volumetric velocity the nematodes can be forced through the capillary structure due to the increased pressure drop and the properties of non-rigid particles. Finally, we found that the best setup was using 6.1 μm wide capillaries at 0.5 ml/h flow rate.

The nematode infected blood sample, which was obtained at the same homogeneity, was forced through the FTNF devices. The filtrate contained not only nematodes, but other blood components (mainly WBCs and platelets). The risk of clogging of the devices could be significant, if the serological sample was highly populated by nematodes and the measurement took longer, than the estimated procedure time. The total filtration capacity of the FTNF devices were not between the main aims of the research work, but the contamination of an average or low populated samples. The total blockage of the device was not observed during the experimental procedures on a highly populated sample (++).

The classical veterinarian procedures include sedimentation or centrifugation just for sample preparation and the total procedure time takes $30 - 45$ $mins$ without guarantee to homogeneity of concentration of nematodes [146]. The analysis of 0.01 ml sample using the microfluidic devices at 0.25 ml/h volumetric flow rate takes 58 $mins$, at 0.5 ml/h takes 29 $mins$ and at 1 ml/h takes 15 $mins$ which is comparable with the widely used nematode diagnostic procedures (table 3.2). The parallelization of the measurement reduces the procedure time guaranteeing the same filtration efficiency.

3.7 Results with the Flow Through Nematode Filter

I have successfully shown how microfilariae circulating in the blood stream can be filtered and detected using the flow-through nematode filter (FTNF). This microfluidic device provides a new diagnostic method for parasitic detection from native blood samples. Pressure and velocity profiles have been calculated to predict the pressure drop

DOI:10.15774/PPKE.ITK.2015.011

to secure the efficiency of the microfluidic device. A range of microcapillary structures within different microfluidic devices have been designed, fabricated and tested to uncover dirofilarioses from blood samples. Our results show that this passive filtration device can be used to speed up current diagnostic processes. A parasite filtration platform has been constructed to automate the procedure decreasing diagnostic costs and time. The obtained structure is able to use for filtration of other specific parasites. Due to the applied materials, the FTNF device also can be loaded by the degas-driven flow avoiding the usage of external syringe pumps to create a laboratory-independent construction.

3.8 Related thesis groups

Thesis Group I: I have designed, developed and characterized a novel flow through filter with isobaric filter region for the separation, enrichment and analysis of blood-borne pathogens ro aid and simplify diagnostic procedures of parasitoses.

Related publications [L1, L4-L10]

I.1: I have designed and developed a novel device structure using biocompatible materials for the filtration of a wide range of micron-size pathogens.

a) I have designed a novel microcapillary structure arranged in a circular geometry for hydrophoretic filtration of micron-size pathogens with isobaric filtration conditions which us called a flow-through nematode filter(FTNF). I have designed structures with different capillary widths ($W_{capillary}$) from 6.1 μm up to 15.4 μm to test a wide range of pressure and flow conditions for optimization purposes.

b) I have determined the velocity and pressure profile of each FTNF for different flow rates using computational fluid dynamics (CFD) simulations. I have calculated the pressure drop and the flow resistivity of each FTNF structure to develop an isobaric condition in the center of the structure, and to avoid leakages during the experiments. Numerical calculations showed that the designed structures will be able to withstand filtration pressure differences of 1 bar. Also, I have investigated the effect of clogging on pressure drop on the device and found that 50% clogging increases the

DOI:10.15774/PPKE.ITK.2015.011

pressure drop beyond 1 bar.

I.2: I have demonstrated the working principle of the designed nematode filter furthermore, I have determined and measured the efficiency of the FTNF devices and the inhomogeneity of the sample.

a) I have fabricated the FTNF structures with different capillary widths by soft-lithography. I have developed a filtration platform and a 4-step procedure to be used width the FTNF devices.

b) I have determined the efficiency of the FTNF devices with different capillary widths and the inhomogeneity of the blood samples due to particle sedimentation have also been considered during the testing and evaluation. The filtration efficiency was necessary to be introduced due to the implemented filtration method which does not provide 100% percent retention of filtrate. Based on the geometrical parameters of the device, the filtration settings and the nematode size to be filtered ,an average device efficiency parameter could be established for future reference. Due to the sedimentation of the heavier particles (nematodes), inhomogeneity (IH) of the serological sample can occur at low flow rates, which can cause false prediction of the nematode population in the original sample because more concentrated samples filter differently through the device.

Testing the filtration devices with nematode infected canine blood, I experimentally measured the efficiency of each FTNF device taking into consideration the inhomogeneity based differences in filtration of the blood sample at different flow rates (0.25 ml/h, 0.5 ml/h and 1 ml/h). I found that the optimal setup was to use 6.1 μm wide capillary structure at 0.5 ml/h flow rate.

I was able to represent the influence of the flow rate on the inhomogeneity of the sample due to the sedimentation. Based on the measurements, I found that increasing flow rate, the homogeneity of the sample increased.

Decreasing capillary width ($W_{capillary}$), the filtration efficiency increases but beyond a higher volumetric rate the nematodes can be forced through the capillary structure due to the raised pressure drop.

DOI:10.15774/PPKE.ITK.2015.011

Chapter 4

Deterministic Lateral Displacement Based Fractionation

4.1 Separation of Microvesicles from Serological Samples

As it was discussed in Chapter 2, blood can be considered as a diagnostic tool for monitoring the body functions of the patient. The extracellular space of multicellular organisms contains solutions of metabolites, ions, proteins and polysaccharides and a large number of mobile membrane-bounded vesicles, called extracellular vesicles such as exosomes (Exs), microvesicles (MVs) and apoptotic bodies (ABs) [162]. The size ranges of major blood components is represented in Fig. 4.1.

Recent advances in the study of tumor-derived microvesicles reveal new insights into the cellular basis of disease progression and the potential to translate this knowledge into innovative approaches for cancer diagnostics and personalized therapy [163]. A key step in cancer diagnostics and molecular biological observations is to separate cells, functionalized microbeads, extracellular vesicles, or other particles from a solution which may contain other undesirable elements [30]. Even though a number of microfluidic techniques have been developed to enhance on-chip blood fractionation [11], classification of membrane vesicles, protocols of their isolation and detection, molecular details of vesicular release, clearance and biological functions are still under intense investigation. The most frequently used methods to purify microvesicles and exosomes

DOI:10.15774/PPKE.ITK.2015.011

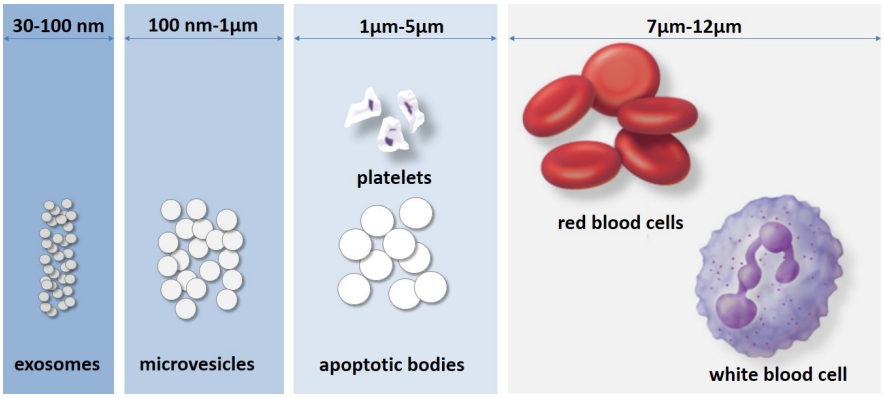

Figure 4.1: Size ranges of major blood components. While exosomes share size distribution with viruses, microvesicles overlap in size with bacteria and protein aggregates (e.g. immune complexes), apoptotic bodies and thrombocytes fall into the size range of $1-5\ \mu m$, the diameter of red blood cells is around $6-8\ \mu m$ and the size of lymphocytes is from $7\ \mu m$ up to $12\ \mu m$.

from cell culture supernatants or body fluids involve a series of centrifugation and filtration steps to remove cells, apoptotic bodies and other cellular contaminants by a final high-speed ultracentrifugation to pellet small extracellular vesicles [164]. These procedures require long preparation time, ultracentrifuge equipment and yield a relatively low amount of extracellular vesicles [165], making it difficult for application in clinical practice.

In chapter 1, I have classified the different microfluidic sample preparation techniques. Based on the scientific literature, I have decided to develop a novel microfluidic device to separate tumor-delivered extracellular microvesicles from serological samples. The novelty of the microfluidic device is the continuous and label-free separation of microvesicles across functional laminar streams in pressure-driven microfluidic flow that uses an asymmetric micropost array.

The chosen continuous, label-free separation procedure was reported first by Huang et al. [88], known as deterministic lateral displacement (DLD), and shown in Fig. 4.2. The device has 3 inlets and a few millimeters long microfluidic channel with an asymmetric post array. The theoretical background of the DLD structure is discussed in Sec. 4.9. The DLD technique is a size-based particle fractionation procedure which has shown an extremely high size selectivity, adaptability to sorting multiple particle sizes, and a broad range of operating conditions, sorting particles from sub-

DOI:10.15774/PPKE.ITK.2015.011

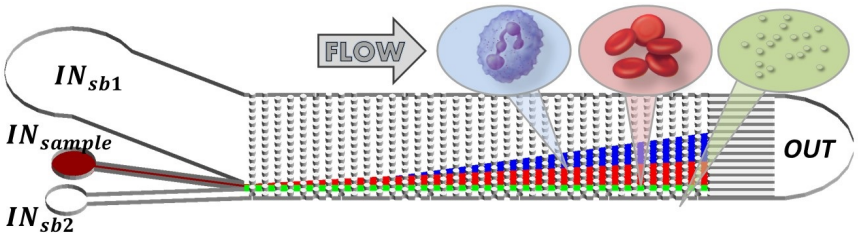

Figure 4.2: Overview image from the deterministic lateral displacement device. The serological sample (IN_{sample}) is focused by the lateral sheath buffer solutions (IN_{SB1} and IN_{SB1}). The different-sized particles are fractionated along the column structure (leukocytes (blue), erythrocytes (red), and microvesicles (green)).

Application	Critical diameter (D_c)	Post shape	References
Leukocytes	From 3 μm to 23 μm	Circular	[86, 91, 96, 166]
Erythrocytes	From 3 μm to 9 μm	Circular, square, I-shape	[167, 168]
Thrombocytes	From 2.3 μm to 5.3 μm	Circular	[97]
Plasma	From 1 μm to 4 μm	Circular	[91]
Circulating tumor cells	From 5 μm to 7 μm	Circular, triangular	[84, 100, 169]
Nematodes, infections, pathogens	From 1.2 μm to 15 μm	Circular, I-shape	[83, 88, 90, 92, 95, 98, 167]

Table 4.1: Serological applications of the deterministic lateral displacement [170]. The critical diameter (D_c) determines the size of separated particles.

micrometer scale up to millimeter scale [87–89, 91, 92, 101, 171–177] with even a resolution of down to 10 nm [88]. This technique which shows a marked improvement over existing methods [170], has been shown capable of separating erythrocytes (RBCs), white blood cells (WBCs), thrombocytes, plasma, circulating tumor cells and nematodes/infections/pathogens from whole blood based on their size as summed up in Table 4.1. Being a continuous separation method, DLD has all the advantages that such methods have to offer. Furthermore, clinical implementation of DLD devices may open new perspectives in translational medicine both in diagnostics and therapy.

Based on the literature, I have designed and developed a microfluidic device, which

DOI:10.15774/PPKE.ITK.2015.011

implements a DLD structure to fractionate serological samples with 500 nm resolution for biomedical purpose. In the following sections, I introduce the applied geometrical parameters of the microfluidic device (Sec. 4.2), the computational fluid dynamics simulations (Sec. 4.3), the fabrication protocol (Sec. 4.4), the sample preparation steps (Sec. 4.5), the experimental setup (Sec. 4.6), the implemented cell counting algorithm (Sec. 4.7), and finally the results of the measurements (Sec. 4.8).

4.2 Design Parameters of the Developed Microfluidic Device

Figure 4.3 shows the geometrical parameters of the asymmetric array. The horizontal (tangential to the flow) distance between two column lines is γ, the vertical array period is λ, each subsequent column is shifted by $\Delta\lambda$ and diameter of pillars is D_{post}. Microvesicles (green particles) remain within the flow stream and cells (red particles) are displaced by α angle at each obstacle.

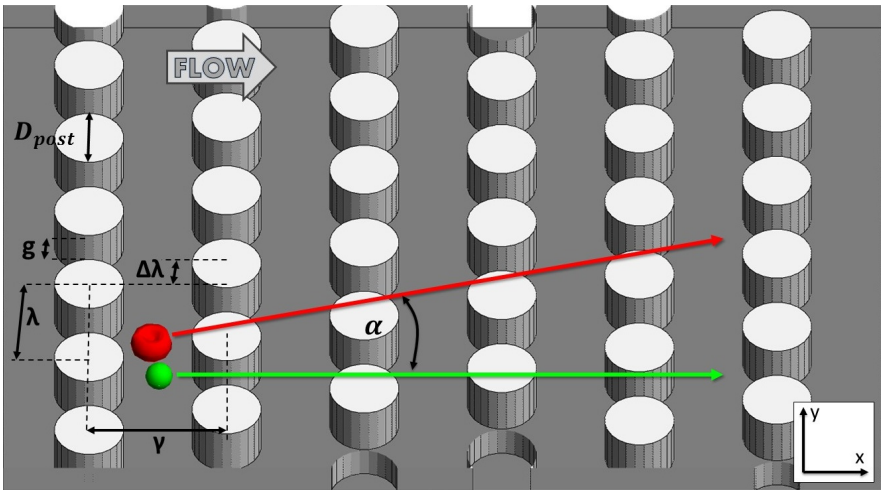

Figure 4.3: Definition of the device geometry based on [88]. The horizontal (tangential to the flow) distance between two column lines is γ, the vertical array period is λ, each subsequent column is shifted by $\Delta\lambda$ and diameter of pillars is D_{post}. Microvesicles (green particles) remain within the flow stream and cells (red particles) are displaced by α angle at each obstacle.

These geometrical parameters describe a threshold size, which is also called critical diameter (D_c), where the bigger particles are displaced from the smaller ones. The

DOI:10.15774/PPKE.ITK.2015.011

theoretical models of the particle separation along the DLD structure are discussed in Sec. 4.9. Multiple arrays with different geometrical parameters connected in series (a serial connection of different critical size DLD structures) have also been implemented to retrieve size fractions of mixed particles. The DLD array was designed with pillars of 20 μm diameter (D_{post}), the gap between adjacent pillars in each column (g) is 10 μm, the vertical (perpendicular to the flow) array period (λ) is 30 μm and the horizontal (tangential to the flow) array period (γ) is 40 μm. The column shift ratio (ϵ_n) which ranges from 0.1 up to 0.33 with steps of 1/60, describes 15 column sections (n) following each other thus the $D_{c,n}$ is between 3.9 μm and 7.7 μm in such an array sequence (Table 4.2). The width of our DLD structure is 1.5 mm, while the length is 11 mm thus the sidewall effect could be negligible along the DLD structure.

n	$\Delta\lambda_n$ $[\mu m]$	ϵ_n	α_n $[Deg]$	L_n $[\mu m]$	$D_{max,n}$ $[\mu m]$	$D_{c,n}$ $[\mu m]$
1	3	0.100	4.3	720	54	3.9
2	3.5	0.117	5.0	720	63	4.3
3	4	0.133	5.7	680	68	4.6
4	4.5	0.150	6.4	600	67.5	4.9
5	5	0.167	7.1	560	70	5.2
6	5.5	0.183	7.8	520	71.5	5.5
7	6	0.200	8.5	480	72	5.7
8	6.5	0.217	9.2	440	71.5	6.0
9	7	0.233	9.9	440	77	6.3
10	7.5	0.250	10.6	400	75	6.5
11	8	0.267	11.3	400	80	6.8
12	8.5	0.283	12.0	400	85	7.0
13	9	0.300	12.7	400	90	7.3
14	9.5	0.317	13.4	400	95	7.5
15	10	0.333	14.0	400	100	7.7

Table 4.2: Device geometry parameters. $\lambda = 30\ \mu m$, $D_{post} = 20\ \mu m$, $g = 10\ \mu m$ and $\gamma = 40\ \mu m$ are fixed parameters (see Fig.**??**). α_n is the angle of displacement, L_n is the length of a section, $D_{max,n}$ is maximum vertical (tangential to the flow) distance which the displaced particles ($D_{particle}>D_{c,n}$) can be drifted during section n and $D_{c,n}$ is the critical diameter of each section

DOI:10.15774/PPKE.ITK.2015.011

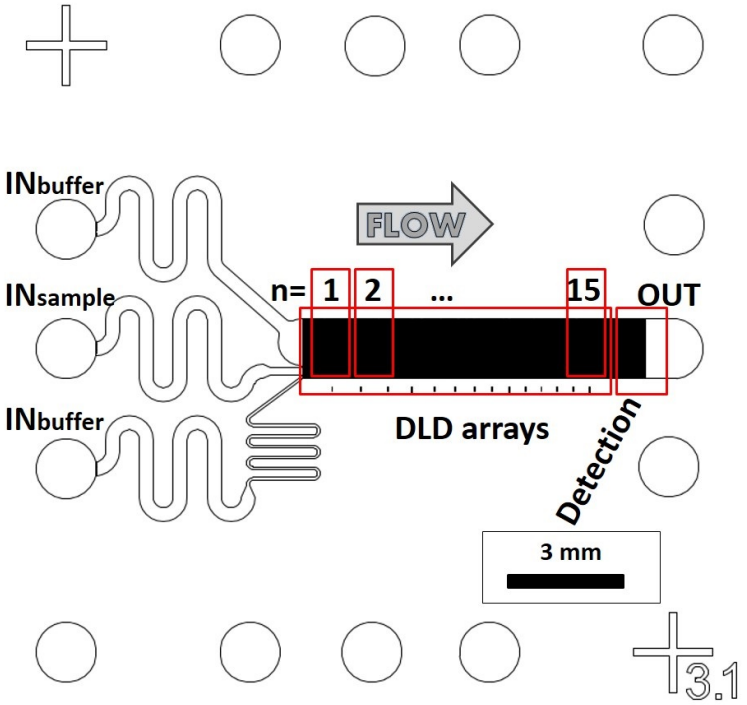

Figure 4.4: The design of the microfluidic device, which has 3 inlets and 1 outlet. The DLD array zone contains 15 array sections with different critical diameters implemented. The detection area is before the outlet.

Figure 4.4 shows the layout of the microfluidic structure, which consists of 15 different sections with different critical diameters. The biological sample is injected at the center inlet (IN_{sample}) and hydrodynamically focused by sheath buffers (IN_{buffer}) and pushed through the array structure. The 7560 μm-long DLD array terminates in an observation section in which the laterally displaced distance and the occurred dispersion can be measured optically in set of parallel channels. These channels facilitate counting and binning of the cells for the histograms.

4.3 Flow and Pressure Profiles of the DLD Structure

Velocity and pressure profiles of the DLD structure have been calculated in each section applying the physical properties of blood and solving the Navier-Stokes equa-

DOI:10.15774/PPKE.ITK.2015.011

tion 2.2 by COMSOL Multiphysics 4.4 to optimize the geometry of microfluidic device. The calculation of the pressure drop profile was necessary to optimize the height of the device, and also to determine the effective length of the DLD structure (Fig. 4.5). The prediction of the velocity profile was useful to design the sidewalls and the background structure of the DLD device.

The pressure drop (ΔP) across the DLD device, which has an effects on the shape and the rigidity of the cells, is a function of fluid viscosity (μ), the flow rate (Q), the gap distance between two pillars in the same row (g), the length of the device (L), the channel height (h) and the channel width (w, $w>>h$). The gap size (g) between inertial obstacles, the total width of the DLD array are fixed (in our device, $g = 10\ \mu m$, $w_{device} = 1.5\ mm$) and using the boundary condition of structure-incorporated sidewall (Fig. 4.21.C) the pressure drop between two adjacent column lines (ΔP_i) is constant; thus the total pressure drop over the entire DLD structure could be calculated by the following way:

$$\Delta P_{tot} = \sum_{1}^{n} k_i * \Delta P_i = \sum_{1}^{n} k_i * Q * R_i, \tag{4.1}$$

where k_i is the number of column lines in section n and R_i is the fluid resistance using Eq. 2.4:

$$R_i = \frac{\mu\gamma B_{nom_i}^4}{32\pi(wh)^4}, \tag{4.2}$$

where B_{nom_i} is the wetted nominal perimeter of cross-section area. The total pressure drop ΔP_{tot} of the DLD array with different channel heights (5 μm, 10 μm, 20 μm, 30 μm, 50 μm) at different flow rates (from 1 mm/s up to 10 mm/s with step of 1 mm/s) was calculated by computational fluid dynamics simulations and displayed in Fig. 4.5. The flow resistivity in different channel height (5 μm, 10 μm, 20 μm, 30 μm, 50 μm), which is shown in Fig. 4.6, is defined as:

$$\rho_i = \frac{\mu B_{nom}^4}{32\pi(wh)^3}. \tag{4.3}$$

The prediction of pressure drop had an important role to determine the height of the device at a fixed flow rate. To reach the proposed aim, the volumetric flow rate on the inlets had to be regulated. Based on computational fluid dynamics simulation, the pressure drop was calculated on different-height channel structures. The results of simulation on calculation of pressure drop shows that increasing the channels height,

DOI:10.15774/PPKE.ITK.2015.011

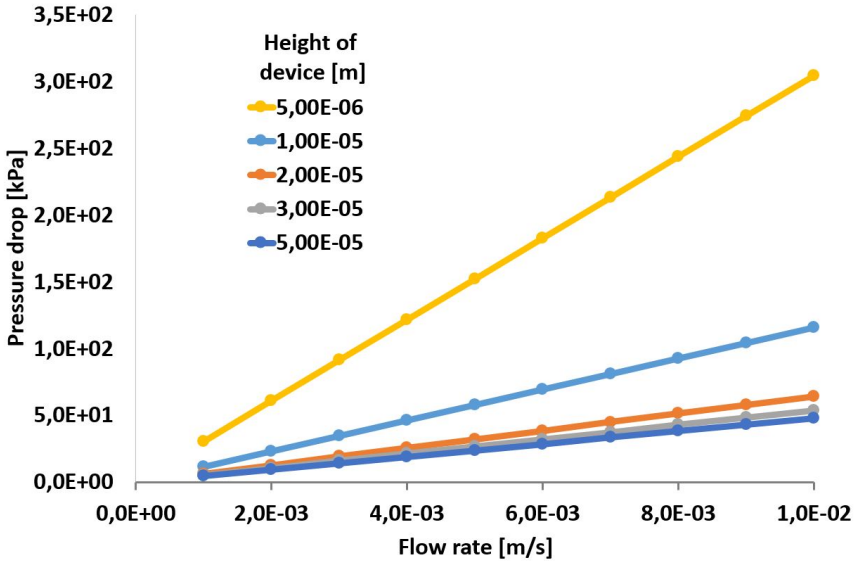

Figure 4.5: The calculated total pressure drop of the DLD array with different channel heights (5 μm, 10 μm, 20 μm, 30 μm, and 50 μm) at different flow rates.

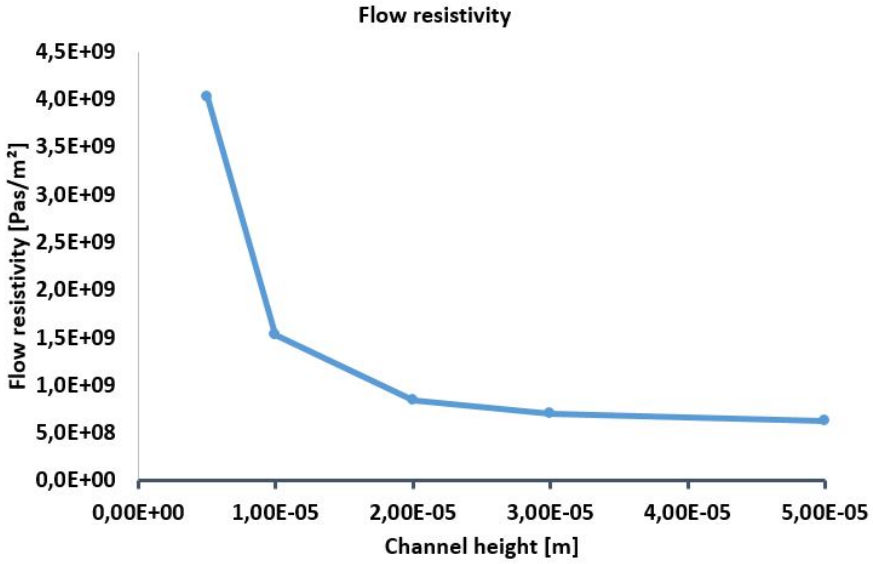

Figure 4.6: The calculated flow resistivity of the DLD array in different channel height (5 μm, 10 μm, 20 μm, 30 μm, and 50 μm) at different flow rates.

the pressure drop along the DLD structure will decrease. The pressure drop of the DLD structure with a 20 μm height channel remains under $5 \cdot 10^3$ Pa at $1 \cdot 10^{-2}$ m/s, which is inside the optimal range of usage conditions. Finally, in consideration of a

DOI:10.15774/PPKE.ITK.2015.011

longer DLD structure the lateral displacement of the particles will increase but along with that the pressure drop will also increase.

4.4 Device Fabrication

I have applied the same fabrication steps as it was discussed in section 3.4. Channel layouts were designed using AutoCAD 2013 and devices were produced using standard microfabrication soft-lithographic techniques [161,178] by casting polydimethylsiloxane on a SU-8 positive relief patterned mold on a 4" silicon wafer which was produced using photolithography. PDMS monomer and curing agent were mixed to a ratio of $10 : 1$ (v/v), degassed and poured over the master and set aside at $70°C$ for 2 h for crosslinking. The liquid PDMS pre-polymer conforms to the shape of the master and replicates the features of the master. The crosslinked PDMS was removed from the mold and 0.75 mm inlet and outlet ports were fabricated through the PDMS slab using a Harris Uni-Core biopsy punch. The patterned PDMS slab was bonded to microscope glass slide following surface treatment by Plasma-preen II 863. Finally, Teflon tubes were inserted into the access holes for fluidic contacts. The depth of all channels used was 20 μm.

4.5 Sample Preparation

The isolation of red bood cells (RBCs) and white blood cells (WBCs) was based on the Ficoll - Paque^{TM} process. Venous human blood was collected from a male healthy adult volunteer and diluted by buffer solution (PBS with 2 mM EDTA) at a ratio of 1:1 (v/v). 35 mL of diluted blood was carefully layered over 15 mL of Ficoll-Paque (Ficoll-Paque PLUS, GE Healthcare Europe GmbH, Freiburg, Germany) in a 50 mL conical tube. The sample was centrifuged at 400 g for 20 $minutes$ at $20°C$ in a swinging-bucket rotor without brake. The isolated mononuclear cell layer (lymphocytes and monocytes) was carefully aspirated and transferred to a new conical tube. The conical tube was filled by buffer (PBS with 2 mM EDTA), and the cells were resuspended and centrifuged at 300 g for 7 $minutes$ at $20°C$. The supernatant was removed and the cell pellet, which contained WBCs, was resuspended in basic media (RPMI-1640 with

DOI:10.15774/PPKE.ITK.2015.011

10% FBS) (sample A). RBCs were harvested from the first 50 mL conical tube from the pellet, and resuspended in basic media (RPMI-1640 with 10% FBS) (sample B).

For the isolation of microvesicles we used a purification procedure as described previously by Turiák, Misják et al. [179]. The first steps are designed to eliminate cells and large extracellular vesicles by successive centrifugations at increasing speeds at each of these steps, the pellet was discarded and the supernatant was used for the following step. Firstly, the conditioned medium, which mainly contains microvesicles (MVs) and exosomes (Exs) but also contained some apoptotic bodies (ABs) from BV-2 cell culture (mouse, C57BL/6, brain, microglial cells), was centrifuged at 300 g for 20 minutes at 17°C. The pellet consisting of cells was discarded and the supernatant was transferred to conical tubes. Next, apoptotic bodies were removed from the supernatant by centrifuging it at 2000 g for 20 minutes at 17°C. The supernatant was submitted for further centrifugation. Finally the supernatant (enriched in microvesicles and exosomes) was centrifuged at 20000 g for 40 minutes at 4°C, and the microvesicle pellet was resuspended in 0.5 ml PBS. This microvesicle preparation was added to cell- and platelet-depleted blood plasma (sample C).

4.6 Experimental Setup

Pressure-driven flow was created using syringe pumps, which were attached to the inlet via Teflon tubes. This setting made it possible to hydrodynamically focus the sample into a stream of 20 μm in width. Typical flow rates were used between 0.01 ml/h and 0.1 ml/h, and they were controlled by the syringe pump. Before the measurements the devices were treated by poliethylenglicol solution($20ml\ H_2O + 0.2g\ PEG$) during 60 mins to avoid clogging. Imaging was performed on an inverted Olympus IX71 microscope. Image recording was through an EyeRIS camera system. I have developed an image processing algorithm on a CNN-based device to count the number of particles in real-time.

4.7 The Developed Cell Counting Algorithm

My aim was to develop a semi-automated system for these high resolution separation tasks that consists of controllable syringe pumps, controllable microscopic platform, a

DOI:10.15774/PPKE.ITK.2015.011

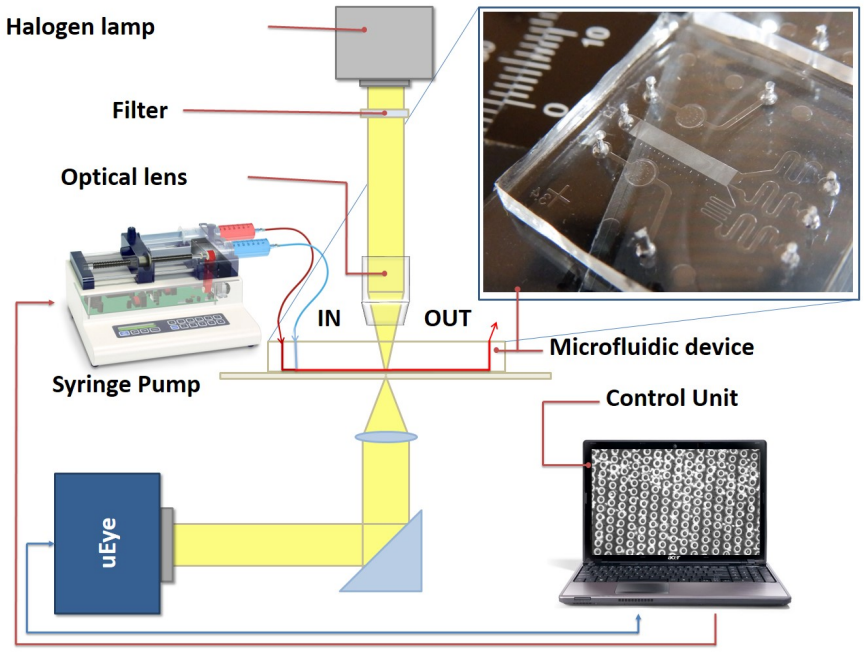

Figure 4.7: Schematic view of our experimental setup. The platform consists of computer-controlled syringe pump system, a microfluidic device on an inverted microscope, and a CNN-based camera (EyeRIS).

camera and real-time image processing. The latter two tasks can be implemented in modern camera systems (e.g. the programmable EyeRIS system by Anafocus; the programmable SPS02 by Toshiba Teli; or the Bi-I system by Eutecus). Our University has ongoing research in these areas as well, it was obvious that we could greatly improve the functionality and automation of the experimental setup with such a device.

Therefore,I have developed a CNN-based algorithm implemented on an EyeRIS v1.3 camera, which is able to count particles in continuous liquid flow using the following image processing steps. The algorithm is the following: image recognition, Gaussian filter, global threshold, morphologic erosion, morphologic dilatation, morphologic centering, and cell/object counting. The proposed algorithm works with grey-scale and binary images and contains four main parts. First of all, it starts with the image recognition, continues the preprocessing part with filtration. Thirdly, the algorithm performs the binary image processing steps, which start with the threshold measurements, and terminate with one pixel in the middle of recognized cells. Finally, the cells/particles are counted from the result images.

DOI:10.15774/PPKE.ITK.2015.011

During the measurements the integration time (also called exposure time) is highly correlated to the light intensity ($expTime = 0.7\ ms$). The observation output channels of the DLD structure is monitored (*SensedImg N*, showed in Fig. 4.8.A). The camera has a limited $144x176$ resolution, the field of view is around 190 μm x 230 μm and the RBCs are approximately 5-6 pixels in size.

The sensed image (*SensedImg N*, Fig. 4.8.A) could be perturbed with different noises due to the sensor or external causes. The proposed algorithm starts with a Gaussian filter to reduce the single pixel noise (*GaussianImg N*, Fig. 4.8.B).

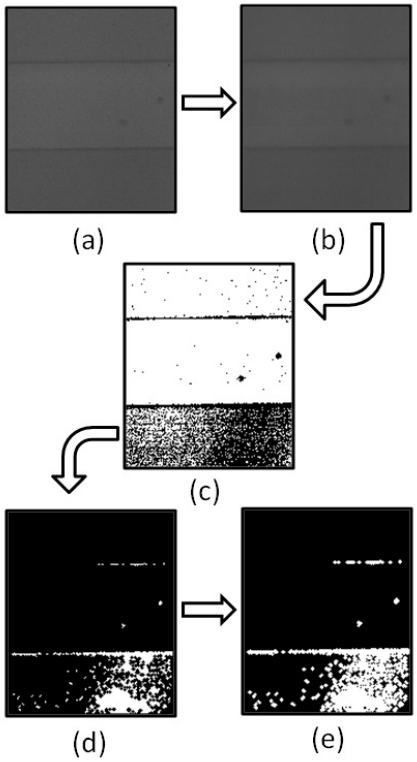

Figure 4.8: Cell detection algorithm. A) Grey-scale sensed image from the cell flow (*SensedImg N*). B) Gaussian filtering on the *SensedImg N* (*GaussianImg N*). C) Binary image is the result of use of threshold (*ThreshImg N*). D) The erosion function eliminates the noise from the image (*ErosionImg N*). E) Dilatation fills the holes on the cells (*DilatationImg N*).

The conversion from gray-scale (*GaussianImg N*) to binary image (*ThreshImg N*, Fig. 4.8.C) is made by the global threshold value (GTV). The histogram of the gray-scale image is not flattened, the values of the pixels are between 100 and 145,

DOI:10.15774/PPKE.ITK.2015.011

nevertheless we can consider a stable microfluidic system with fixed illumination ($TresholdValue = 115$). During this step the algorithm uses only one function, thus it is optimal in time, but not in quality. The fluctuation of the light can cause significant errors, if the size of noise exceeds 2-3 pixels.

The erosion function on a binary image (*ErosionImg N*, Fig. 4.8.D) eliminates or reduces the noise. Before this step the image is inverted because the following functions work with white objects on black background. Two main methods exist for image erosion. The first is to use a predefined constant that allows to select between 4-neighbor connection and 8-neighbor connection or use a 3x3 pattern that completely defines the structuring element. Our algorithm is based on the first method with the 4-neighbor connection case and erases 1 pixels to open morphologically the objects and eliminate the one pixel errors.

The erosion function erases not only the noise and mistakes, but also consumes pixels from the objects, which is compensated by the algorithm in the next step. The dilatation is complementary to the morphological closing, it dilates a binary image in which objects are white and the background is black. After the dilatation function the cells have the same diameter on the result image (*DilatationImg N*, Fig. 4.8.E) like before the erosion. The second importance of dilatation is colligated to the next function.

The last step of the image precessing is the centering. This function gets the centroid positions of the objects (*CentroidImg N*). The morphological centroid peels the image one pixel off as many times as indicated in an input parameter. In our case, it iterates until no change occurs between iterations.

The termination part of the algorithm counts the cells/particles inside the Region-Of-Interest (ROI), which is determined by a predefined binary mask (*MaskImg*). The result image (*ResultImg N*) is generated from a logical AND function of the *CentroidImg N* and the *MaskImg*. The flow velocity is constant inside the output channel and generally it is 0.020 mm/s. If the flow velocity is fix, in that case also the waiting time ($T_{waiting} = 2370ms$) is well-known between two subsequent images (*ResultImg N*, *ResultImg N+1*). The number of the white pixels in the *ResultImg N* Images describes the number of the cells in the focused liquid flow. The efficiency of this algorithm was more than 90 percent.

DOI:10.15774/PPKE.ITK.2015.011

4.8 Experimental Results

Section 4.5 introduces the applied sample preparation procedures and the type of the samples. Sample A contains WBCs, sample B contains RBCs and sample C has microvesicles with the well defined concentrations. During the measurements, a composition of the purified blood components (sample D = sample A + sample B + sample C, w/w 1:1:1), such as RBCs, WBCs and microvesicles, was loaded into the center inlet (IN_{Sample}) whereas the sheath buffer (PBS) was introduced at the ports on the left (IN_{sb1}) and right (IN_{sb2}) sides of the sample port thus focusing the sample flow to the desired width (Fig. 4.2). The concentration of RBCs (sample B) was around $5 \cdot 10^6$ per μL, WBCs (sample A) were around $7 \cdot 10^3$ per μL and microvesicles (sample C) were around $8 \cdot 10^4$ per μL. Thrombocytes and apoptotic bodies have been extracted from the sample simplifying optical classifications. During the measurements negligible population of the WBCs has been attached to the surface of the obstacles thus the purity of applied process could be conserved.

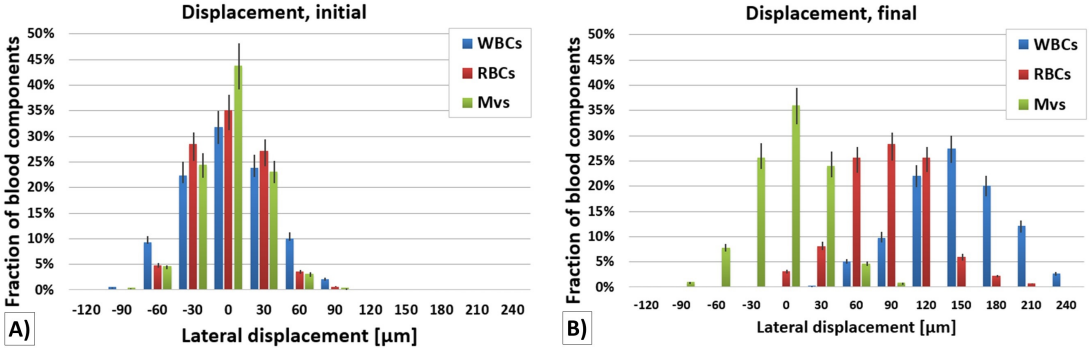

Figure 4.9: The efficiency of cell separations using the DLD device (white blood cells (WBCs, blue), red blood cells (RBCs, red), and microvesicles (MVs, green)). A) The dispersion of the blood components in the initial section ($n = 1$). B) The lateral displacement of the components in the final section ($n = 15$). The error bar displays the standard deviations.

To optically detect the blood elements, the biological sample (sample D) is driven through the device at 0.001 ml/h flow rate which provides a suitable rate of cells for counting and a suitable residence time in front of the camera to be imaged. We record the lateral position of particles from the center of the inlet at two different positions along the device ($n = 1$ and $n = 15$) in the DLD array and bin the results of 10 different

DOI:10.15774/PPKE.ITK.2015.011

measurements into histograms which are shown in Fig. 4.9. Around $1.47 \cdot 10^5$ of particles have been optically distinguished and classified into WBCs, RBCs and microvesicles.

The microvesicles, which are below any critical hydrodynamic diameter $D_{c,n}$, are able to follow a given stream through the array in zigzagging mode whereas RBCs and WBCs occur laterally displaced by every interaction with posts. The further displacement of WBCs occur, when the diameter of RBCs becomes equal with the actual critical diameter of the post arrayand RBCs enter in zigzagging mode meanwhile WBCs are forced to adopt orientations that give them a greater displacement along the device.

Shear forces, which result from gradients in the fluid velocity around a particle may induce complex motions including rotation, tumbling and shape change [168]. RBCs and WBCs can be considered as deformable and non-spherical particles, which suggests that such blood cells appear to modify their shape and diameter as they pass through the DLD device which can lead to lower separation efficiency. The behavior of blood components in the DLD array results in smooth histograms (Fig. 4.9). The displacement of RBCs, WBCs and microvesicles are observed at the terminal section by the described system (Sec. 4.6)and algorithm (Sec. 4.7).

The displacement of the different particles are bins for the histograms at the initial section (Fig. 4.9.A)and in the observation zone (the end of our DLD array) (Fig. 4.9.B). The position of microvesicles remains equal to their initial position along the entire device due to the dimensionless numbers of fluid dynamics (Re_p<1, Pe>1 and St<1). The lateral displacement of RBCs from the center of the inlet is around $100 - 120\ \mu m$ between the initial and the terminal sections. Whereas, WBCs are displaced by $140 - 160\ \mu m$ from their initial position. The obtained and reported efficiency of fractionation can be increased by a longer device and the throughput can be improved by parallel microfluidic devices.

DOI:10.15774/PPKE.ITK.2015.011

4.9 Device Principles

The results of our experiments applying the DLD structure for novel biomedical applications, highlights the need to study the theoretical backgrounds more deeply. The first publications presented separation theories of the DLD structures from the results of the experiments [88].

Huang el al. states that the DLD separation utilizes the specific arrangement of posts within a channel to precisely control the trajectory of and facilitate separation of particles larger and smaller than a critical diameter (D_c) [88]. Each succeeding row within a constriction is shifted laterally at a set distance from the predecessor, this leads to the creation of separate flow laminae, which follow well defined paths through the device [88]. If the particles below D_c are able to follow one such stream through the array (zigzagging mode) whereas bigger particles are forced through interactions with posts, to change streams many times, always in the same general direction, becoming laterally displaced (displacement mode). The DLD phenomenon is based on the column shift fraction (ϵ):

$$\epsilon = \frac{\Delta\lambda}{\lambda} = \frac{1}{N} = \tan\alpha, \tag{4.4}$$

which is the ratio of vertical (tangential to the flow) distance that each subsequent column is shifted ($\Delta\lambda$) to the vertical array period (λ), N is the period of geometry repetition and α is the displacement angle. Inglis et al. described the critical diameter of the separation [101] by the following equation :

$$D_c = 2g\epsilon\eta, \tag{4.5}$$

where g is the gap distance between two pillars in the same row ($g = D_{post} - \lambda$) and η is a dimension-less parameter taking into account the parabolic flow profile between the pillars in the array, which is a consequence of pressure driven flow [101]. Each flow between two obstacles can be divided into $N = 1/\epsilon$ streams, which carry equal fluid flux. These streams shift their position in a cyclic manner thus after N subsequent columns each stream returns to its initial position within the gap.

If the radius of particles is bigger than the mentioned first stream, these particles will be displaced laterally by $\alpha = \arctan(\epsilon) = \arctan(\frac{\Delta\lambda}{\lambda})$ angle (displacement mode), meanwhile if their radius is less, they will follow the cyclic repetition of the streams

DOI:10.15774/PPKE.ITK.2015.011

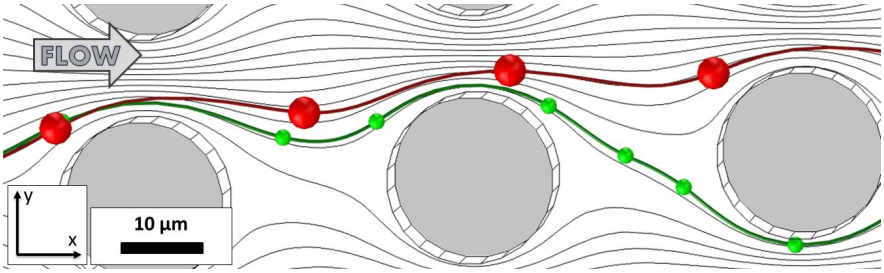

Figure 4.10: Migration of particles along the deterministic lateral displacement array. The smaller than D_c particles flow in zigzagging mode (ZM) The bigger than D_c particles travel in displacement mode (DM). $N = 10$, $g = 10\ \mu m$, $\gamma = 40\ \mu m$, and $\lambda = 30\ \mu m$.

(zigzag mode, $\alpha = 0°$) as it is shown in Fig. 4.10. Due to this case, the width of the first stream can be considered the following way [101]:

$$\beta = g\epsilon\eta = \frac{D_c}{2}. \tag{4.6}$$

If β is defined to be the width of the first stream which is correlated by the following way with the flow profile ($v(x)$) within the gap (g)

$$\int_0^{\beta} v(x)dx = \epsilon \int_0^{g} v(x)dx. \tag{4.7}$$

By assuming a conventional parabolic flow profile through the gap with zero velocity at the post sidewalls, the flow profile can be numerically determined by

$$v(x) = \left[\frac{g^2}{4} - \left(x - \frac{g}{2}\right)^2\right]. \tag{4.8}$$

Solving Eq. 4.7 involves finding the cube root of

$$\left[\frac{\beta}{g}\right]^3 - \frac{3}{2}\left[\frac{\beta}{g}\right]^2 + \epsilon\frac{1}{2} = 0. \tag{4.9}$$

Assuming the flow profile between the micro obstacles is parabolic which holds true at low Reynolds number, the critical separation diameter D_c can be numerically determined by [101]:

$$D_c = g\left[1 + 2w + \frac{1}{2w}\right], \tag{4.10}$$

where

$$w = \left[\frac{1}{8} - \frac{\epsilon}{4} + \sqrt{\frac{\epsilon}{16}(\epsilon - 1)}\right]^{1/3}\left(-\frac{1}{2} - i\frac{\sqrt{3}}{2}\right). \tag{4.11}$$

DOI:10.15774/PPKE.ITK.2015.011

The previously published models explain the migration of the particles based on the particle-obstacle interaction and these models do not consider the mass, the diameter and the velocity of the particles along the DLD array. I have constructed a novel theory of the migration of the particles with real physical parameters within the DLD structure, which called inertia-based particle separation and discussed in the following section 4.10.

4.10 Inertia-based Particle Separation Theory

In order to achieve spatial control of particles in microchannels, a mechanism of lateral migration is required. The DLD structure can be considered as a manipulation tool that can be used to fractionate a randomly distributed set of particles in a flow [180]. The drag force accelerates the particles until they are forced free in the flow direction and travel at the average intersected fluid speed. Lift forces are most often applied to differentiating different-sized/mass particles.

This inertial migration phenomenon of the particles along the DLD structure could be observed by the mismatch between fluid streams and particle trajectories, which is induced by the geometric configuration of channel with sudden expansion and contraction elements [5, 181].

Let us consider a Descartes coordinate system in two dimensions, as it is shown in Fig. 4.3, where x coordinate is in the longitudinal direction and y is in the perpendicular direction of the DLD structure.

In this coordinate system, let us consider an infinite wide DLD structure; thus the influence of sidewall effect (Sec. 4.11.3) on the flow streams could be neglected. Applying a stable, developed velocity profile along the DLD structure, the number of the equivolumed is determined by the period of geometry repetition (N) (Eq. 4.4). It means, after N column line the fluid stream returns to the same position. Each stream carries equal fluid flux but is not necessary the same stream width as is shown in Fig. 4.11.

Figure 4.11 demonstrates the x- and y-components of the flow velocity field between two obstacles with streams. Before reaching the smallest cross-section area, the liquid flow is pinched thus its velocity is accelerated. In other hand leaving the pinched area, the nominal channel diameter is increased; thus the flow velocity is reduced.

DOI:10.15774/PPKE.ITK.2015.011

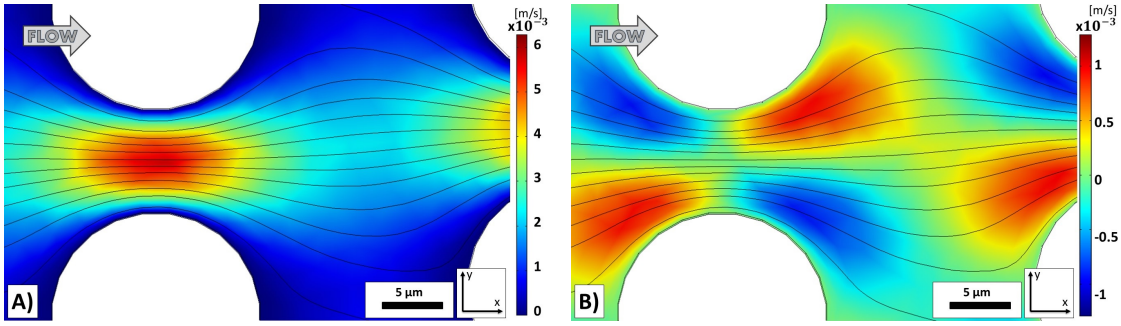

Figure 4.11: Flow velocity field with streams (black lines) within the DLD device ($v_{IN} = 1 \cdot 10^{-3}$ m/s, $h = 20$ μm, $N = 10$, $g = 10$ μm, $\gamma = 40$ μm, and $\lambda = 30$ μm). A) the x-component of the velocity field B) the y-component of the velocity field.

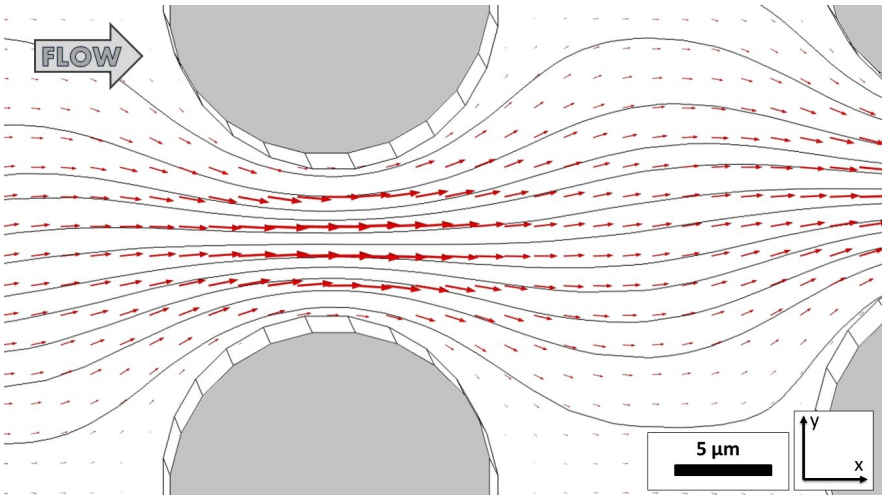

Figure 4.12: Streams (black lines) and vector field of flow velocity (red arrows) within a DLD array ($v_{IN} = 1 \cdot 10^{-3}$ m/s, $h = 20$ μm, $N = 10$, $g = 10$ μm, $\gamma = 40$ μm, and $\lambda = 30$ μm).

However, the x-component of the velocity field dominates; the y-component is also important, which causes the lateral migration of the particles along the DLD structure. Figure 4.12 shows the vector field of flow velocity with the streams between obstacles at same boundary conditions $v_{IN} = 1 \cdot 10^{-3}$ m/s, $h = 20$ μm, $N = 10$, $g = 10$ μm, $\gamma = 40$ μm, and $\lambda = 30$ μm).

Let us consider neutrally buoyant particles in this stable, developed flow velocity field. The longitudinal inertial force on the particle is the drag force (F_D), which is

DOI:10.15774/PPKE.ITK.2015.011

defined the following way:

$$F_D = \frac{1}{2}\rho v^2 C_D A, \tag{4.12}$$

where ρ is the fluid density, v velocity of the particle, A is the reference area, and C_D is the drag coefficient, which is a dimensionless coefficient related to the geometry of the object. Let us consider rigid, circular particles with diameter and mass: (d_1, m_1, and m_2, d_2). The drag force of circular particles could be simplified into the following equation:

$$F_D = 3\pi\mu d v, \tag{4.13}$$

where μ is the dynamic viscosity and d is the diameter of the particle. Using Newton's second law the acceleration of the particle is the following:

$$a = \frac{3\pi\mu d v}{m}. \tag{4.14}$$

The tangential inertial lift effects on the neutrally buoyant particles [182–184]: the wall-induced lift force and the shear gradient induced lift force. The wall-induced lift force is an interaction between the particle and the adjacent wall, which directs the particle away from the wall. The shear gradient induced lift force, due to the curvature of the velocity flow profile, directs the particle away from the center of the channel. The particles also have an effect on the streams they are carried by thus altering the original streams.

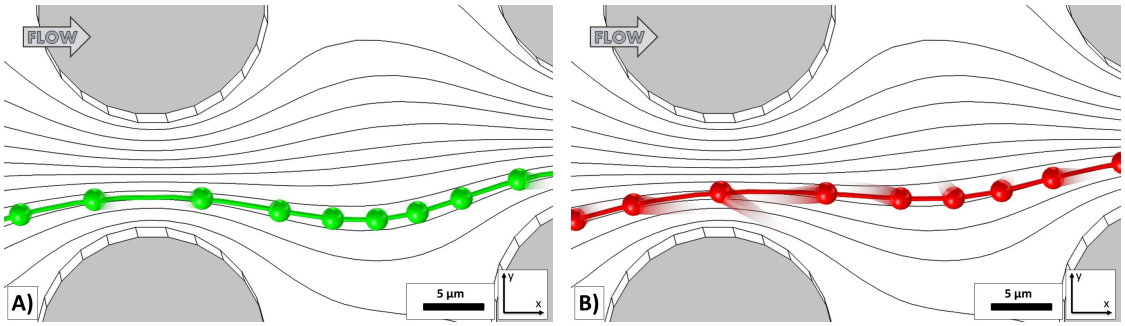

Figure 4.13: The cornet tails on two different particles ($d_1 = d_2$ and $m_1 < m_2$) along the trajectories represent the acting drag forces with streams (black lines), and the flow direction ($v_{IN} = 1 \cdot 10^{-3}$ m/s, $h = 20$ μm, $N = 10$, $g = 10$ μm, $\gamma = 40$ μm, and $\lambda = 30$ μm). A) Low-inertial particle (m_1) at different time steps with cornet tails on its trace, which represent the acting drag force at actual positions. B) High-inertial particle (m_2) at different time steps with cornet tails on its trace.

DOI:10.15774/PPKE.ITK.2015.011

Figure 4.13 represents a DLD structure ($N = 10$, $g = 10\ \mu m$, $\gamma = 40\ \mu m$, and $\lambda = 30\ \mu m$) with flow streams and trajectories of two different particles, which have diameter and mass ($d_1 = d_2$ and $m_1 < m_2$). The initial position of these particles is the same, but their trajectories become different along the DLD structure. The particle with smaller inertia (green) travels with the flow streams, but the particle with bigger inertia (red) traverse through the streams.

The small inertia particle travels in a zigzagging mode in its original stream, which returns into the same displacement position from its origin after N constrictions. In a zigzagging mode ($\alpha = 0°$), the small inertia particle is laterally displaced $N - 1$ times, but at the last cyclic step (N^{th}) this particle returns into the original position without any lateral displacement by the last downstream. In a displacement mode ($\alpha = \arctan(\epsilon)$), the high inertia particle is drifted away from their original flow stream into the adjacent stream at each column line as it is shown in Fig. 4.10.

For a better analysis of the particle migration along the DLD structure, an inlet line in vertical position has been applied in the middle of the channel. As it was described by Eq. 4.14, in consideration of a constant viscosity, three variables could influence the acceleration of particles: the velocity (v), the diameter of the particles (d), and the mass of the particles (m). The following part discusses the influence of the mass, the diameter, and the velocity of the particles on the travel mode (zigzagging/displacement).

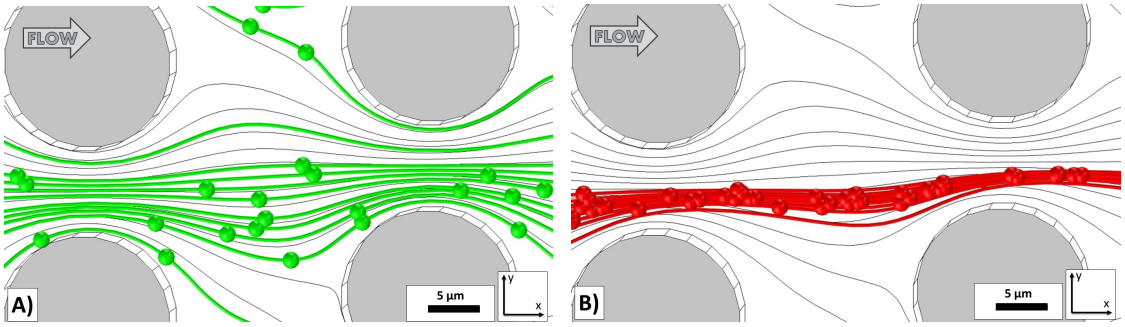

Figure 4.14: Trajectories of the same particles with flow streams (black lines) from horizontal inlet ($h = 20\ \mu m$, $N = 10$, $g = 10\ \mu m$, $\gamma = 40\ \mu m$, and $\lambda = 30\ \mu m$) at different flow rates ($v_{IN1} < v_{IN2}$). A) At lower flow rate (v_{IN1}) the particles could follow the flow streams. B) At higher flow rates (v_{IN2}) the particles are displaced laterally mismatching their streams.

First of all, let us consider only one particle type along the DLD structure entering

DOI:10.15774/PPKE.ITK.2015.011

into the DLD structure in a horizontal line at different flow rates ($v_{IN1} < v_{IN2}$). Figure 4.14 shows that, at lower flow rates (v_{IN1}) the particles could follow the flow streams, meanwhile at higher flow rates (v_{IN2}) the particles are displaced laterally crossing their streams.

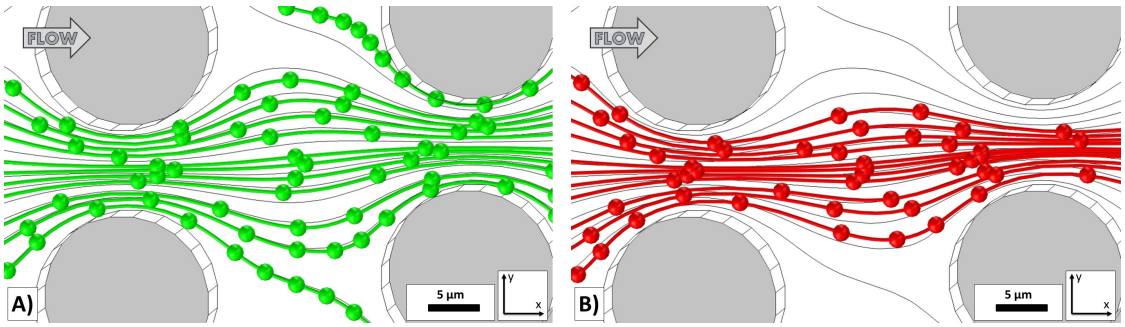

Figure 4.15: Trajectories of different-weights but identical sizes particles ($d_1 = d_2$ and $m_1 < m_2$) with flow streams (black lines) from horizontal inlet ($v_{IN} = 1 \cdot 10^{-3}$ m/s, $h = 20$ μm, $N = 10$, $g = 10$ μm, $\gamma = 40$ μm, and $\lambda = 30$ μm). A) The lighter particles (m_1) flow in zigzagging mode. B) The heavier particles (m_2) are displaced laterally.

Let us consider a fix flow rate and two types of particles with the same diameter but different-mass ($d_1 = d_2$ and $m_1 < m_2$). Figure 4.15 shows that case, when the lighter particles (m_1) follow the flow streams without crossing them, and travel along the DLD structure in zigzagging mode. Instead, the heavier particles (m_2) leave the original streams along the DLD structure displacing themselves laterally.

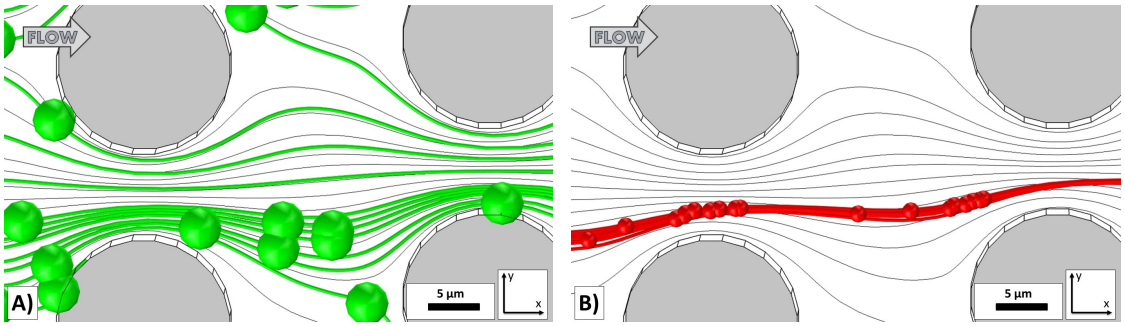

Figure 4.16: Trajectories of different-sized (in diameter) but equal weight particles ($d_1 < d_2$ and $m_1 = m_2$) with flow streams (black lines) from horizontal inlet ($v_{IN} = 1 \cdot 10^{-3}$ m/s, $h = 20$ μm, $N = 10$, $g = 10$ μm, $\gamma = 40$ μm, and $\lambda = 30$ μm). A) The bigger particles (d_1) flow in zigzagging mode. B) The smaller particles (d_2) are displaced laterally.

DOI:10.15774/PPKE.ITK.2015.011

Figure 4.16 shows the case, where the diameters of particles are different but their weight is the same ($d_1 > d_2$ and $m_1 = m_2$). The bigger particles (d_1) are moved easily away from the displacing mode into a zigzagging mode than the smaller particles (d_2), which are displaced laterally along the DLD structure.

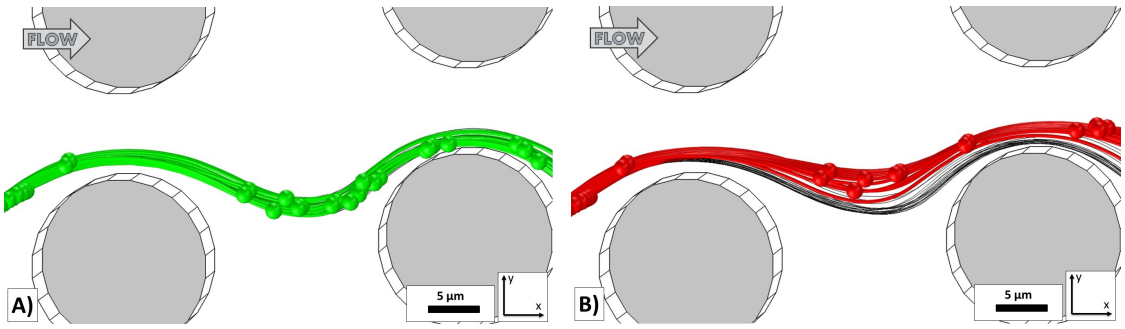

Figure 4.17: Trajectories of different-weights but identical size particles ($d_1 = d_2$ and $m_1 < m_2$) with flow streams (black lines) from vertical inlet ($v_{IN} = 1 \cdot 10^{-3}$ m/s, $h = 20$ μm, $N = 10$, $g = 10$ μm, $\gamma = 40$ μm, and $\lambda = 30$ μm). A) The lighter particles (m_1) follow the original flow streams. B) The heavier particles (m_2) leave the original flow streams.

All of the above figures interpreted results where the particles arrived into the model horizontally at the middle of the device. As it was described previously, we have to consider tangential inertial lift forces on the neutrally buoyant particles. These forces are not identical in the vertical direction thus we have to increase the two dimensions of the Descartes coordinate system into three dimensions, where the z-component is in the direction of height. In a three-dimension system, let us consider a vertical inlet line from the bottom to the top of the channel, where two types of particles with the same diameter but different-weights ($d_1 = d_2$ and $m_1 < m_2$) enter the DLD structure. Figure 4.17 shows these particles from a vertical inlet with streams, where the initial positions have the same line as the particles. In a vertical case, we obtained the same results: the trajectories of the lighter particles (m_1) follow the original flow streams (zigzagging mode), meanwhile the heavier particles (m_2) cross the flow streams.

Introducing the z-direction, the velocity field along the DLD structure has to be interpreted for better understanding. For this purpose, nine cut planes (CP1, CP2, ..., CP9) have been inserted perpendicularly to the x-direction. Figure 4.18 shows the first three cut planes (CP1, CP2, and CP3) with the different components of the flow

DOI:10.15774/PPKE.ITK.2015.011

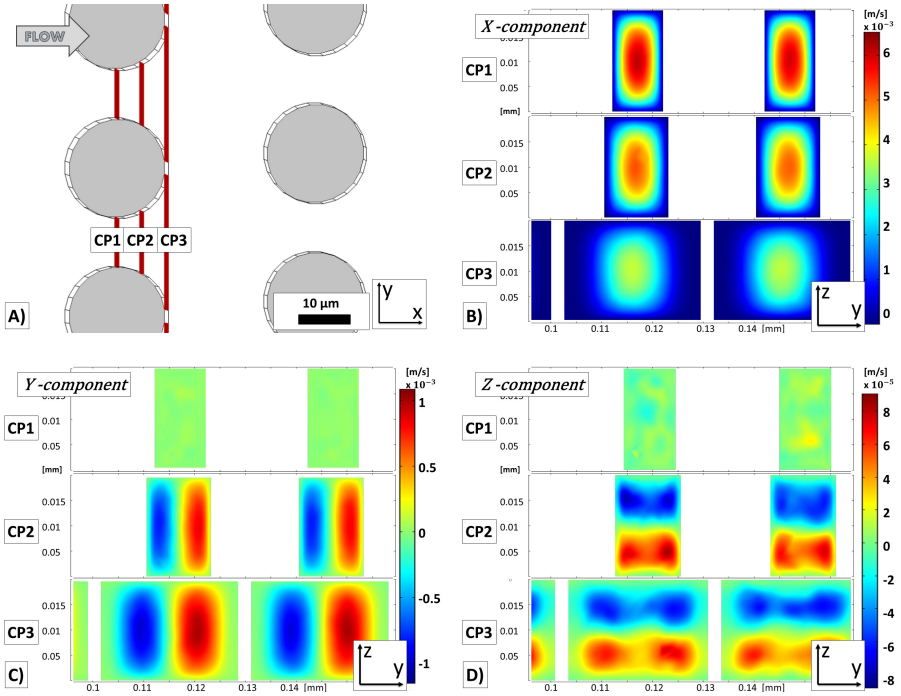

Figure 4.18: Three components of the velocity field after the pinched section. A) showing the z-y plane cross section positions relative to the DLD geometry B) the x-component C) the y-component, and D) the z-component of the flow velocity field at CP1, CP2, and CP3. Please observe the different range of velocities in different directions.

velocity field. The x-component of the flow velocity field is the most dominant among the other components along the DLD device, but the oscillation of y- and z- components also have a significant meaning. At CP1 and CP9, we manage to observe that the flow velocity profile has only x-component but leaving the middle of the pinched section from CP1 to CP3, the y- and z-components increase significantly. Due to an increase of the y-component, the flow streams will open and determine the displacement of different particles. However the z-component of the flow velocity field along the DLD structure is around centesimal of the x-component, it also has an effect on the particles.

The region between two column lines has an important change in the y- and the z-components, which is shown in Fig. 4.19. From CP4 to CP6, these components of the flow velocity field change their sign. For the z-component, this change is without any dependence on y-coordinates, but the change of the y-component has a lateral displacement by $\Delta\lambda$ shift factor due to the influence of the second column line. The

DOI:10.15774/PPKE.ITK.2015.011

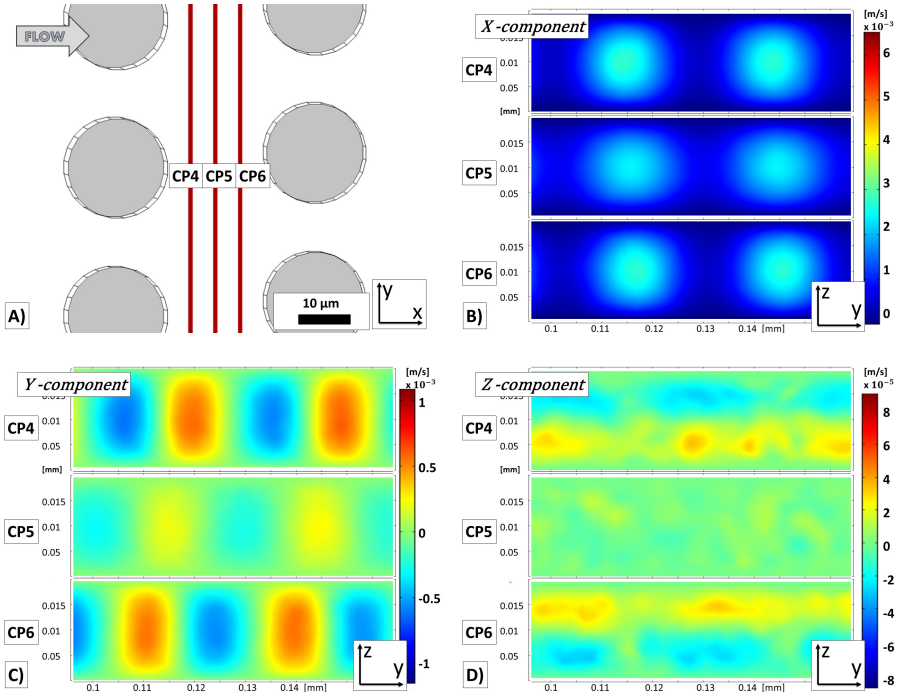

Figure 4.19: Three components of the velocity field between two column lines. A) showing the z-y plane cross section positions relative to the DLD geometry B) the x-component C) the y-component, and D) the z-component of the flow velocity field at CP4, CP5, and CP6.

width of the downstream flow caused by $\Delta\lambda$ determines the resolution of the separation.

Arriving into the pinched section from CP7 to CP9, the x-component starts to rule the flow velocity field and with y-component focus the flow into the gap between two adjacent obstacles as it is shown in Fig. 4.20. From the analysis of particle trajectories, this effect is the most significant due to the fact that in this area the drag force accelerates the particles the most. When the different particles arrive into the expanding regime (Fig. 4.18), the particles with higher inertia cross the opening flow streams and enter in displacement mode. Those particles, which have a lower inertia, let themselves accelerated by the drag force as well, following their original streams after the pinched section.

As it was mentioned previously, the particle effect back to the originally developed stream flow. To simulate the movement of the particles along the DLD structure requires own developed computational fluid dynamics environment. The novel theoretical

DOI:10.15774/PPKE.ITK.2015.011

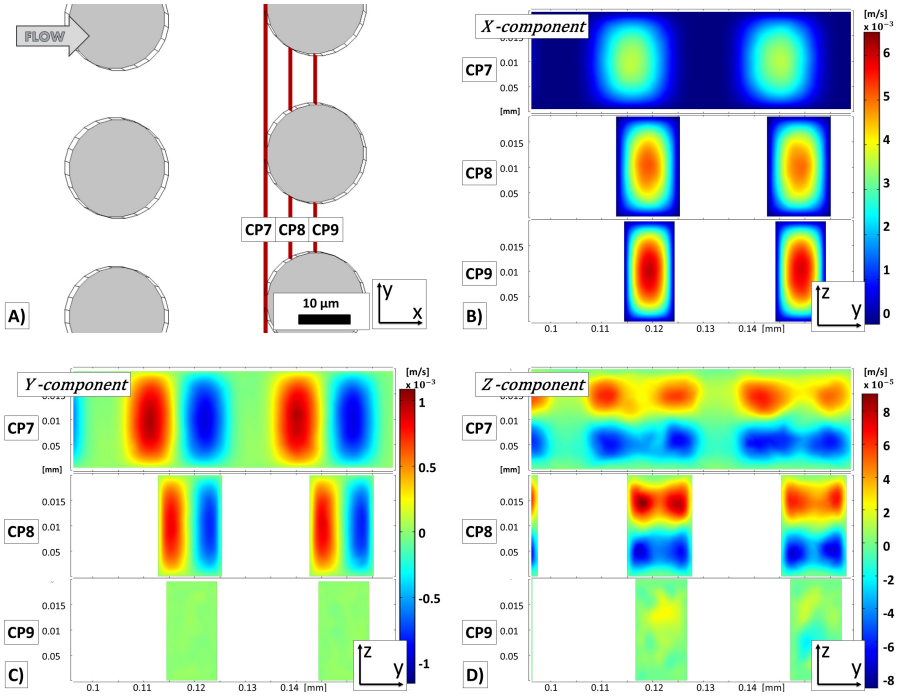

Figure 4.20: Three components of the velocity field before the pinched section. A) showing the z-y plane cross section positions relative to the DLD geometry B) the x-component C) the y-component, and D) the z-component of the flow velocity field at CP7, CP8, and CP9.

model of the particle migration along the DLD structure has to consider also this in the future work.

4.11 Uncovered Research Fields of the DLD effect

The investigation into DLD effect is an encouraging topic between the sample preparation techniques. The following sections highlight the uncovered research fields of the DLD effect.

4.11.1 Post-Particle Interactions

Steric interactions of non-rigid particles with column array effect on the effective size of the cells. Attraction and repulsion can occur with the particles due to external forces which make the particles adhere to the device. In consideration of blood,

DOI:10.15774/PPKE.ITK.2015.011

the adhesion of leucocytes onto the blood vessels is a well-known process during the inflammation response which acts also within the microfluidic devices or modify the migration of the cells along the DLD array. During the presented measurements this effect was minimized by a chemical modification of the inner surfaces of the devices using polyethylene glycol (PEG) solution.

4.11.2 Particle-Particle Interactions

In the DLD array structure, the gap width (g) is commeasurable with the size of solute particles thus their perturbation on the surrounding flow fluid can be significant, which is mostly influenced by their diameter and their rigidity [185]. Increasing the concentration of the sample, the particle-particle interaction will increase this perturbation effect regarding the particle migration, modify the effective diameter of the flexible cells and may stick mostly the leucocytes and thrombocytes to the inner surface, which leads to clogging the DLD structure during a long measurement. In this case, the critical diameter of the DLD array will locally be modified thus decreasing the resolution of fractionation, and the flow resistance will increase decreasing the throughput.

4.11.3 Sidewall Effect

Since the separation mechanism of deterministic lateral displacement array relies on a small amount of fluid flux, the perturbation of the uniform flow profile can be modified significantly close to the sidewalls [186].

Three design possibilities could be considered: straight sidewall (Fig. 4.21.A), zig-zag sidewall (Fig. 4.21.B), and structure-incorporated sidewall (Fig. 4.21.C). The boundary condition of sidewall as linear straight wall modifies the uniform streams close to the sidewall which effect propagates into upper stream layers. The zig-zag sidewall-shape compensates this effect but the structure-incorporated sidewall has less influence on the neighbor streams. Based on these fluid dynamic calculations in the developed structure the structure-incorporated sidewall has been chosen.

4.11.4 Shape of the Obstacles

Many researchers have investigated the effect of changing post shape within a DLD, in order to improve performance whilst retaining several of the advantageous proper-

DOI:10.15774/PPKE.ITK.2015.011

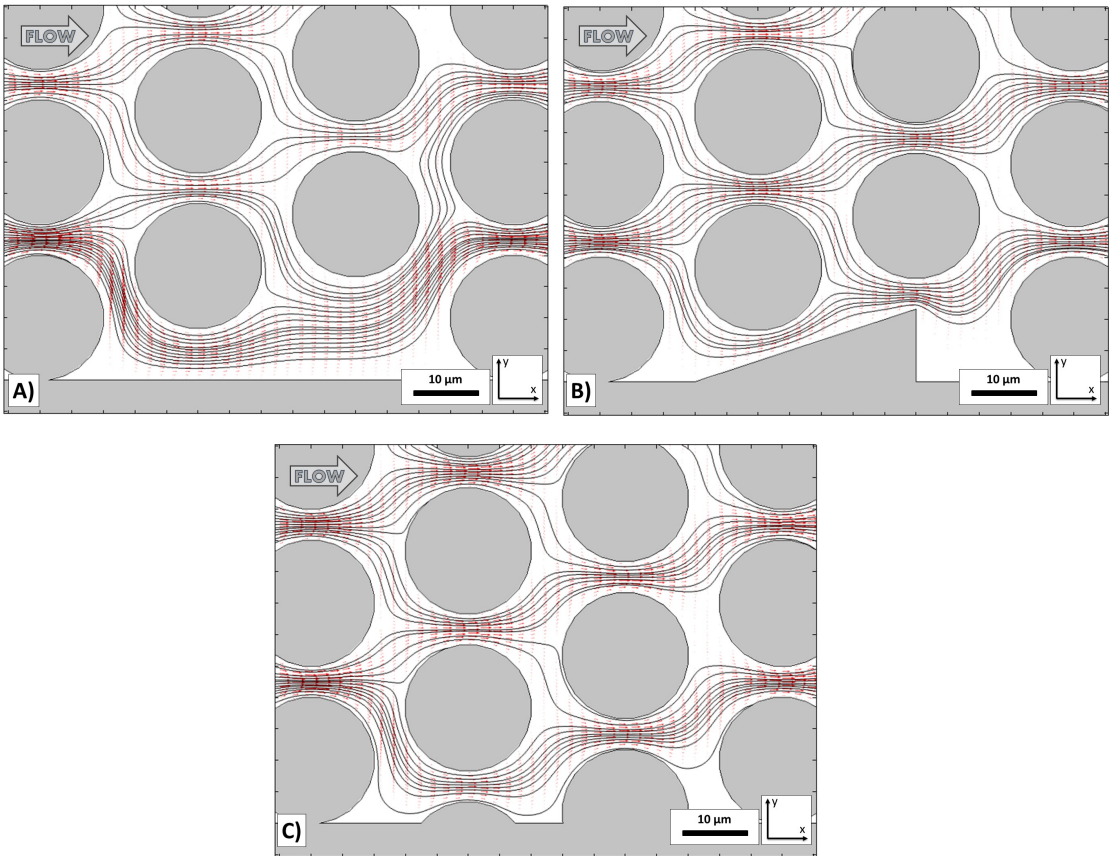

Figure 4.21: Sidewall effect. Streams (black lines) of the deterministic lateral displacement array with $N = 3$, $g = 5\ \mu m$, $\gamma = 15\ \mu m$, and $\lambda = 15\ \mu m$ for each possible sidewall type: straight sidewall (A), zig-zag sidewall (B), and structure-incorporated sidewall (C).

ties of this technology [170]. The widely used round column shape provides symmetric flow velocity profile on both sides of the obstacle. Modifying the shape an asymmetric flow profile can be formed to increase the lateral displacement of bigger particles and decrease the effect of clogging in slow volumetric rate areas (behind the obstacles). A wide variety of post shapes were used experimentally and simulated within DLD structure including round, streamlined, quadrilateral, diamond, triangular, I-shaped, which are summed up in Table 4.1. Fig. 4.22 presents the velocity profile of the mentioned post shapes at 1 mm/s flow velocity, when water was used as a medium with $N = 3$, $\gamma = 25\ \mu m$, and $\lambda = 25\ \mu m$. The zero or negligible velocity profile of the round and the streamlined post shapes is less than the other column types thus these can be

DOI:10.15774/PPKE.ITK.2015.011

considered as the most robust geometry against particle trapping/clogging.

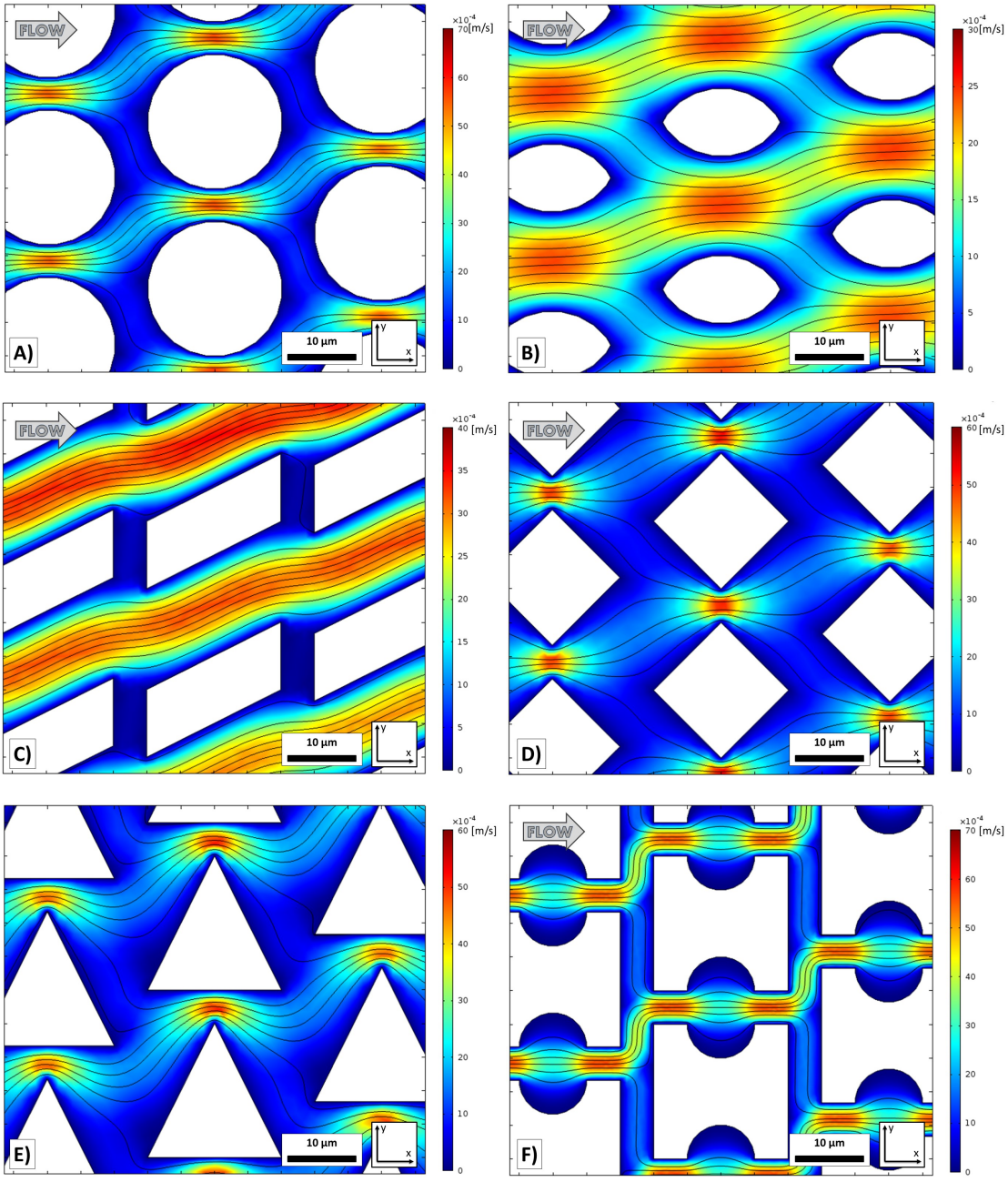

Figure 4.22: Velocity profile with uniform streams (black lines) the deterministic lateral displacement array applying different post shape types form experiments or simulations: A) round B) streamlined C) quadrilateral D) diamond E) triangular F) I-shaped.

DOI:10.15774/PPKE.ITK.2015.011

4.11.5 Separation or Concentration Modes

The DLD structure, as it was described previously, can separate two different particles from each other using an asymmetric array structure. Fig. 4.23.A represents the separation mode where the smaller particles than a critical diameter flow in zigzagging, which is also used in the applied approach. From the original stream, the bigger particles than a critical diameter (D_c) can be displaced laterally into the direction of the sidewall, these particles become concentrated along the DLD structure; thus the device can be used to increase the concentration of bigger particles relative to a background of smaller particles or to remove a fraction of larger particles from a sample (Fig. 4.23.B).

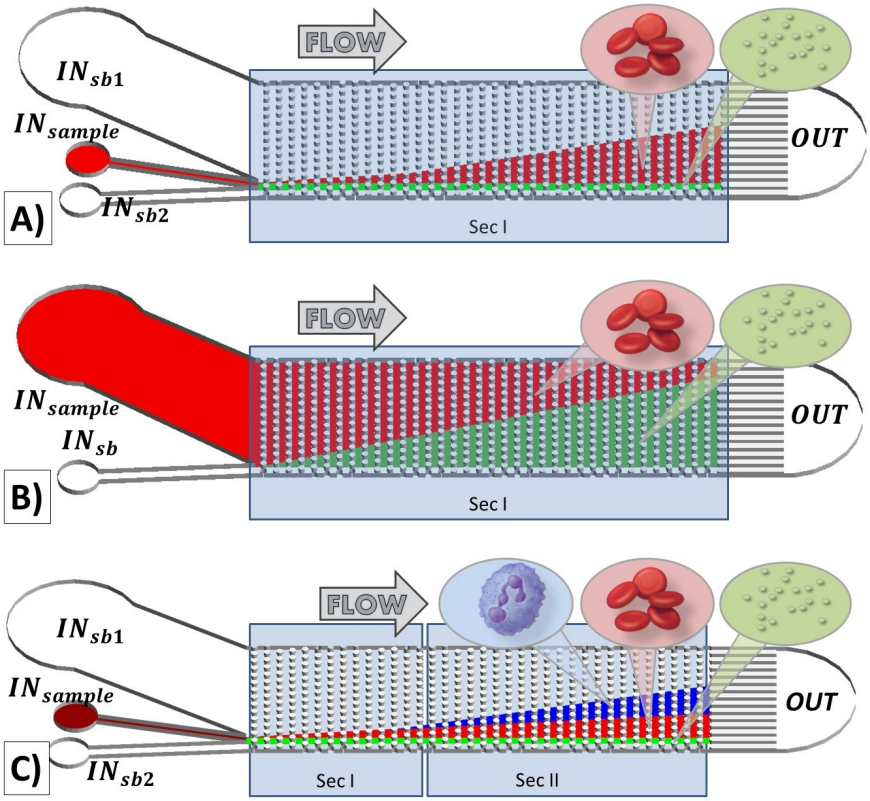

Figure 4.23: Possible application modes of the deterministic lateral displacement. A) Separation of different particles from a focused inlet. B) Concentration of bigger particles than the critical diameter in unfocused sample flow. C) Multiple arrays in series give multi-modal fractionation.

In order to separate particles into more than two fractions, subsequent arrays with different critical diameter can be used as it is shown on Fig. 4.23.C. By having several

DOI:10.15774/PPKE.ITK.2015.011

arrays with sequentially decreasing D_c, it is possible to separate particles within various size thresholds. Increasing critical diameter of the subsequent array should increase the purity of each fraction and should decrease the risk of clogging along the device.

4.11.6 Dynamic Range of the Separation

The range over which a device is functional is an important evaluation of separation technologies. Generally, dynamic range refers to the ratio between the largest and the smallest values of a variable quantity. The dynamic range of a DLD structure can be considered as the ratio of the largest and the smallest critical diameter within the device, at which the separation can operate without clogging. The dynamic range of a single array device is always 1.

The larger the gaps between the obstacles are the better, as the device can accept a broader range of particle sizes, and that is less susceptible to clogging and results in lower resistance and potentially higher throughput. In multiple arrays, the DLD structures with different critical diameters have to be aligned and joined behind each other.

4.11.7 Shape, Deformation, and Rotation of the Particles

Generally, live biological cells are flexible particles and come in many shapes. These solute non-spherical particles travel along the DLD device modifying their orientation and center of mass thank to the fluid-particle, post-particle, and particle-particle interactions. Rotation of the particles varies their effective radius, which also influences the traveling mode along the DLD structure. This can greatly limit the predictability of the computational fluid dynamics simulations but on the other hand, controlling the orientation or flexibility of the solute particles, can lead to the applicable for finer fractionation or to further separation purposes.

4.12 Conclusion and outlook

Extracellular vesicles provide a means for cells to interact with each other and appear to play an important role in cancer research and in a wide variety of physiological and pathological processes. In this study, on-chip microvesicle fractionation from

DOI:10.15774/PPKE.ITK.2015.011

biologically complex samples, such as human blood and conditioned medium from cultured cells was achieved for the first time as a deterministic lateral displacement array structure was used. Compared to the current standard protocols for isolating microvesicles, our deterministic lateral displacement device is faster, cheaper, label-free and its efficiency is comparable with clinical laboratory procedures.

Based on these experiments, the DLD array can be considered as a powerful tool for particle separation and manipulation. We can show the evidence that label-free fractionation of micron-scale particles can be delivered by using a deterministic lateral displacement array. This suggests that our DLD device may be able to provide rapid diagnostic information about the haemostatic condition of a blood sample, to explore cell-to-cell communication or to fractionate blood sample efficiently for clinical tests without the use of an activation specific label or marker. This chapter begins with a concise discussion about label-free separation techniques and the exact biomedical problem is described, which we worked on. We identified that the mechanism of separation is based on an inertia-based motion behavior of the particles along the DLD structure. This causes that the inertia-based separation of particles, which was characterized by computational fluid dynamics simulation, shows correlations with our experimental measurements and results. Based on the theoretical works, we manage to create a DLD structure, which was useful to solve the initial challenge.

The main objective of this chapter was to produce cell-free plasma containing extracellular vesicles from serological samples, and it has been archived successfully. In this version of the microfluidic device, we would like to understand better the functionality of the DLD structure experimentally, determine the position of outlets to increase the efficiency of separation; thus we designed this microfluidic device with an observation part, which torrents into just a single outlet. The cost of these aims was that we have no choice for any analysis of the output products, but only optically using an inverse microscope.

The efficiency of separation could be increased using a longer DLD structure. Using specific surface modification the clogging could be eliminated in the inertial section. The flow resistivity of the inlet channels can be increased applying parallel microcapillaries. These errors will be solved easily in the further designs significantly raising the efficiency of the separation.

DOI:10.15774/PPKE.ITK.2015.011

As it was mentioned before, the DLD can be used in a diagnostic tool for disease severity, assess the efficacy of different treatment strategies and possibly determine the eventual location of metastatic invasions for possible treatment. The DLD structure could be designed for several purposes as biomedical sample preparation, chemical analysis or other industrial applications.

In biomedical sense, the DLD array system could be a useful analytic tool for further hemorheology. The human erythrocyte adopts a distinctive biconcave disc form in vivo. Any change or variety of their structure could highlight uncovered diseases as sicklemia, infection of malaria, or other blood-borne pathogens. Another important field of application is the uncovering of circulating tumor cells (CTCs) and circulating clusters of cancer and stromal cells, which could be identified in the blood of patients by the presence of malignant cancer. CTCs constitute seeds for subsequent growth of additional tumors (metastasis) in vital distant organs, triggering a mechanism that is responsible for the vast majority of cancer-related deaths. The continuous observation or filtration of CTCs using DLD devices could give us invaluable information.

Water is essential to life, but many people do not have access to clean and safe drinking water and many die of waterborne bacterial infections thus nowadays other challenging field, where the DLD structure could apply, is the observation of water-born pathogens from drinking water. The most important bacterial diseases transmitted through water are cholera, typhoid fever and bacillary dysentery. Using the DLD structure with high throughput could be useful also to detect these water-borne pathogens. Finally, I would like to mention, that by changing the separation range close or under micron-range could also have a fundamental interest in biomedical detection field as the fractionation of different-sized extracellular vesicles.

DOI:10.15774/PPKE.ITK.2015.011

4.13 Related thesis groups

Thesis Group II: I have realized a continuous label-free separation of tumor-delivered extracellular vesicles from serological samples by adapting and fine tuning the deterministic lateral displacement (DLD) method. In this novel application area of the method I designed, fabricated and tested separation devices and showed their separation efficiency. I have also studied and extended the physical description of the DLD effect on particles with an inertia-based theory.

Related publications [L2, L10-L15]

II.1: I have developed a multi-modal deterministic lateral displacement array to separate continuously the tumor-delivered extracellular microvesicles from serological samples.

a) I have designed an asymmetric array of cylindrical obstacles implementing the multi-modal deterministic lateral displacement theory. I have calculated the desired critical diameters of each DLD array sections. Each DLD section was designed with cylindric pillars of 20 μm diameter (D_{post}), the gap between adjacent pillars in each columnline (g) is 10 μm, the vertical array period (λ) is 30 μm and the horizontal array period (γ) is 40 μm. The column shift ratio (ϵ_n) which ranges from 0.1 up to 0.33 with steps of 1/60, describes 15 column sections (n) following each other thus the $D_{c,n}$ is between 3.9 μm and 7.7 μm.

b) I have calculated the pressure drop and the flow resistivity of different-height devices to obtain an acceptable channel height and length for the adopted purpose.

c) I have fabricated DLD devices by soft-lithography. I have constructed a microfluidic platform and a procedure to test the DLD devices.

d) I have extended the semi-automated experimental setup with a real-time image processing and particle counting application which required a CNN-based algorithm development to count the number of particles in the final channel section area. I could count the number of cells with this algorithm using an EyeRIS v1.3 camera.

II.2: I have proved experimentally and measured the displacement of the white blood cells, red blood cells, and microvesicles using the DLD structure. Based on the

DOI:10.15774/PPKE.ITK.2015.011

experiments I have created a novel description of the particle migration along the DLD structure.

a) I proved that the proposed label-free fractionation of microvesicle from blood cells in serological samples can be delivered in practice by using the deterministic lateral displacement array at 1 mm/s flow velocity within a 20 μm high DLD structure with $g = 10$ μm, $\lambda = 30$ μm, and $\Delta\lambda$ varies from 3 up to 10 μm with a step of 0.5 μm. I have measured the displacement of these blood components from the initial position at the final detection area.

b) I have created a novel description of the particle migration along the DLD structure, which considers also the physical parameters of the particles (mass, diameter, and velocity).

DOI:10.15774/PPKE.ITK.2015.011

Chapter 5

Conclusions and outlook

In my thesis I have presented a series of improvements to the method of the Flow-Through Nematode Filter to enrich circulating nematodes from native blood and a deterministic lateral displacement device to separate tumor-derived extracellular vesicles from serological samples that I have developed together with my coworkers.

I have successfully developed a novel microcapillary structure for hydrophoretic filtration of blood-borne micron-size pathogens. I have designed a set of novel deterministic filter (flow-thought nematode filter, FTNF) have been designed by increasing capillary width ($W_{capillary}$) from 6.1 μm up to 15.4 μm. I determined the velocity and pressure profile of each FTNF at different flow rates using CFD simulations. I calculated the pressure drop and the flow resistivity of each FTNF to avoid leakages during the experiments. Based on the results of I found that decreasing the capillary width the pressure drop raises at constant flow rate. Raising the flow rate, the pressure drop raises and develop an isobaric condition in the center of the FTNF structure.

I have fabricated FTNF devices by soft-lithography. I have developed a detection platform and a 4-step procedure to use the FTNFs. I have determined the efficiency of the FTNFs and the inhomogeneity of the samples. Testing the microfluidic devices with nematode infected canine blood, I measured the efficiency of the each FTNF device and calculated the robustness of the obtained procedure for veterinary purpose. I found that the efficiency of the constructed devices at 0.25 ml/h, 0.5 ml/h and 1 ml/h flow rate is influenced by the sedimentation and the flow rate. The highest mean efficiency of filtration was obtained at 0.5 ml/h flow velocity with the best trend fit. Based on the measurements, I found that increasing flow rate, the homogeneity and its

DOI:10.15774/PPKE.ITK.2015.011

stability increase. Decreasing capillary width ($W_{capillary}$) the filtration efficiency rises but beyond a higher volumetric rate the nematodes can be forced through the capillary structure due to the raised pressure drop and the properties of non-rigid particles. Finally, I found that the best setup was using 6.1 μm wide capillary at 0.5 ml/h flow rate.

I designed an asymmetric array of cylindrical obstacles implementing multi-modal DLD effect. Each DLD array section was designed with pillars of 20 μm diameter (D_{post}), the gap between adjacent pillars in each column (g) is 10 μm, the horizontal array period (λ) is 30 μm and the vertical (tangential to the flow) array period (γ) is 40 μm. The column shift ratio (ϵ_n) which ranges from 0.1 up to 0.33 with steps of 1/60, describes 15 column sections (n) following each other thus the $D_{c,n}$ is between 3.9 μm and 7.7 μm. I determined the velocity and pressure profile of the DLD arrays using computational fluid dynamic simulations. I calculated the pressure drop between two adjunct column lines, which is useful to determine easily the total pressure drop of all DLD structure. I calculated the flow resistivity of different-heights device to obtain an optimal channel height for the adopted purpose.

I have fabricated the microfluidic devices by soft-lithography. I have developed a separation platform and a procedure to use the DLDs. I proved that the proposed label-free fractionation of microvesicle from blood cells in serological samples can be delivered in practice by using the DLD array at 1 mm/s flow velocity within a 20 μm high DLD structure with $g = 10$ μm, $\lambda = 30$ μm, and $\Delta\lambda$ varies from 3 up to 10 μm with a step of 0.5 μm. I measured the displacement of these blood components from the initial position at the final detection area. And also a CNN-based algorithm was implemented to count the number of particles in the final channel section area. I could count the number of cells with this algorithm using an EyeRIS v1.3 camera.

I have created an inertia-based model of particle migration, which consider also the physical parameters of the particles (mass, diameter, and velocity). Based on computational fluid dynamics simulation, I could demonstrate the effect of mass, diameter, and velocity on the travel mode (zigzagging or displacement mode). I have found that tracing the same particles at different flow rates, there is a threshold flow rate, below which the particles flow in zigzagging mode, above which enter into displacement mode. The inertia-based model of particles migration along DLD structure has seven independent variables (λ, $\Delta\lambda$, γ, g, v, m, d).

DOI:10.15774/PPKE.ITK.2015.011

The developed microfluidic devices can be used as a diagnostic tools for several biomedical purposes as biomedical sample preparation, chemical analysis or other industrial applications. Modifying the geometries of both devices, the developed microfluidic structures can be adapted for novel clinical, veterinarian, and industrial cases.

In biomedical sense, these microfluidic devices can replace analytic procedures or tools in clinical applications. Human erythrocytes adopt biconcave disc form. Any change or variety of their shape highlights diseases as sicklemia, infection of malaria, or other blood-borne pathogens.

Another important application can be the observation of the circulating tumor cells (CTCs), which has an important role in cancer metastasis. The clustering of the cancer and the stromal cells could be useful to show the presence of malignant cancers. The continuous observation or filtration of CTCs using the developed microfluidic devices can give us invaluable information.

Further application of the developed microfluidic devices can be the filtration of drinking water. Water is essential to life, but many people do not have access to clean and safe drinking water and many die of waterborne bacterial infections. The observation and filtration of water-born pathogens from drinking water using microfluidic devices can be significant in the close future.

DOI:10.15774/PPKE.ITK.2015.011

Chapter 6

List of the Publications

[L1] **A. J. Laki**, K. Ivan, E. Fok, and P. Civera, *Filtration of Nematodes using an Integrated Microcapillary System,* BioNanoSci., pp. 111, Oct. 2014.

[L2] **A. J. Laki**, L. Botzheim, K. Ivan, V. Tamasi, and P. Civera, Separation of Microvesicles from Serological Samples Using Deterministic Lateral Displacement Effect, BioNanoSci., pp. 17, Nov. 2014.

[L3] I. N. Huszar, Z. Martonfalvi, **A. J. Laki**, K. Ivan, and M. Kellermayer, Exclusion-Zone Dynamics Explored with Microfluidics and Optical Tweezers, Entropy, vol. 16, no. 8, pp. 43224337, Aug. 2014.

[L4] **A. J. Laki**, G. Z. Nagy, K. Ivan, P. Furjes, O. Jacso, E. Fok, and P. Civera, *Integrated microcapillary system for microfluidic parasite analysis,* in 2013 IEEE Biomedical Circuits and Systems Conference (BioCAS), 2013, pp. 118121.

[L5] **A. J. Laki**, K. Ivan, Z. Fekete, D. Demarchi, and P. Civera, *Filtration of intravenous cardiopulmonary parasitic nematodes using a cross-flow microfluidic separator,* presented at the NanoBio-Europe (NBE), 2012.

[L6] **A. J. Laki**, K. Ivan, Z. Fekete, P. Furjes, and P. Civera, *Filtration of intravenous cardiopulmonary parasitic nematodes using a cross-flow microfluidic separator,"* presented at the EMBL Microfluidics, 2012.

[L7] **A. J. Laki**, K. Ivan, P. Furjes, and P. Civera, *Integrated microcapillary system for microfluidic parasite analysis,* presented at the Advances in Microfluidics & Nanofluidics (AMN), 2013.

[L8] **A. J. Laki**, G. Z. Nagy, K. Ivan, P. Furjes, and P. Civera, *Stand-alone integrated microfluidic parasite analysis system,* presented at the From Medicine to Bionics,

DOI:10.15774/PPKE.ITK.2015.011

2013.

[L9] **A. J. Laki**, G. Nagy, K. Ivan, P. Furjes, and P. Civera, *Stand-alone integrated microfluidic parasite analysis system,* presented at the NanoBioEurope (NBE), 2013.

[L10] **A. J. Laki**, G. Nagy, K. Ivan, P. Furjes, and P. Civera, *Stand-alone integrated microfluidic parasite analysis system,* presented at the International Conference on Biomedical Engineering (ICBME), 2013.

[L11] **A. J. Laki**, L. Botzheim, K. Ivan, T. G. Szabo, V. Tamasi, E. Buzas, and P. Civera, *Microvesicle Fractionation Using Deterministic Lateral Displacement Effect,* presented at the IEEE Nano/Micro Engineered and Molecular Systems (IEEE-NEMS), 2014.

[L12] **A. J. Laki**, L. Botzheim, K. Ivan, T. Szabo, E. I. Buzas, and P. Civera, *Label-Free Fractionation of Tumor-Derived Extracellular Vesicles from Human Blood Using Deterministic Lateral Displacement Effect,* presented at the Miniaturized Systems for Chemistry and Life Sciences (MicroTAS 2014), 2014.

[L13] **A. J. Laki**, I. Rattalino, A. Sanginario, N. Piacentini, K. Ivan, D. Lapadatu, J. Taylor, D. Demarchi, and P. Civera, *An integrated and mixed technology LOC hydrodynamic focuser for cell counting application,* presented at the IEEE Biomedical Circuits and Systems Conference (BioCAS), 2010, pp. 7477.

[L14] **A. J. Laki**, I. Rattalino, F. Corinto, K. Ivan, D. Demarchi, and P. Civera, *An integrated LOC hydrodynamic focuser with a CNN-based camera system for cell counting application,* presented at the IEEE Biomedical Circuits and Systems Conference (BioCAS), 2011, pp. 301304.

[L15] **A. J. Laki**, A. Sanginario, D. Demarchi, K. Ivan, and P. Civera, *An Integrated and Mixed Technology LOC Hydrodynamic Focuser for Cell Counting Structures,* presented at the NanoBio-Europe (NBE), 2011.

DOI:10.15774/PPKE.ITK.2015.011

References

[1] G. M. Whitesides, "The origins and the future of microfluidics," *Nature*, vol. 442, no. 7101, pp. 368–373, Jul. 2006. 1, 3

[2] S. Haeberle and R. Zengerle, "Microfluidic platforms for lab-on-a-chip applications," *Lab on a Chip*, vol. 7, no. 9, pp. 1094–1110, Aug. 2007. 1

[3] D. R. Reyes, D. Iossifidis, P.-A. Auroux, and A. Manz, "Micro total analysis systems. 1. introduction, theory, and technology," *Analytical Chemistry*, vol. 74, no. 12, pp. 2623–2636, Jun. 2002. 1

[4] P.-A. Auroux, D. Iossifidis, D. R. Reyes, and A. Manz, "Micro total analysis systems. 2. analytical standard operations and applications," *Analytical Chemistry*, vol. 74, no. 12, pp. 2637–2652, Jun. 2002. 1

[5] T. M. Squires and S. R. Quake, "Microfluidics: Fluid physics at the nanoliter scale," *Reviews of Modern Physics*, vol. 77, no. 3, pp. 977–1026, Oct. 2005. 1, 58

[6] C. D. Chin, V. Linder, and S. K. Sia, "Lab-on-a-chip devices for global health: Past studies and future opportunities," *Lab on a Chip*, vol. 7, no. 1, pp. 41–57, Dec. 2006. 1

[7] S. F. Ibrahim and G. v. d. Engh, "Flow cytometry and cell sorting," in *Cell Separation*, ser. Advances in Biochemical Engineering/Biotechnology, A. Kumar, I. Y. Galaev, and B. Mattiasson, Eds. Springer Berlin Heidelberg, Jan. 2007, no. 106, pp. 19–39. 1

[8] M. B. Dainiak, A. Kumar, I. Y. Galaev, and B. Mattiasson, "Methods in cell separations," in *Cell Separation*, ser. Advances in Biochemical Engineer-

DOI:10.15774/PPKE.ITK.2015.011

ing/Biotechnology, A. Kumar, I. Y. Galaev, and B. Mattiasson, Eds. Springer Berlin Heidelberg, Jan. 2007, no. 106, pp. 1–18. 1, 2

[9] X.-J. J. Li and Y. Zhou, *Microfluidic Devices for Biomedical Applications*. Elsevier, Oct. 2013. 1

[10] D. R. Gossett, W. M. Weaver, A. J. Mach, S. C. Hur, H. T. K. Tse, W. Lee, H. Amini, and D. D. Carlo, "Label-free cell separation and sorting in microfluidic systems," *Analytical and Bioanalytical Chemistry*, vol. 397, no. 8, pp. 3249–3267, Aug. 2010. 1, 2

[11] H. W. Hou, A. A. S. Bhagat, W. C. Lee, S. Huang, J. Han, and C. T. Lim, "Microfluidic devices for blood fractionation," *Micromachines*, vol. 2, no. 3, pp. 319–343, Jul. 2011. 2, 41

[12] T. Chianea, N. E. Assidjo, and P. J. P. Cardot, "Sedimentation field-flow-fractionation: emergence of a new cell separation methodology," *Talanta*, vol. 51, no. 5, pp. 835–847, Apr. 2000. 2

[13] H. Pertoft, "Fractionation of cells and subcellular particles with percoll," *Journal of Biochemical and Biophysical Methods*, vol. 44, no. 1-2, pp. 1–30, Jul. 2000. 2

[14] P. Cuatrecasas and C. B. Anfinsen, "Affinity chromatography," *Annual Review of Biochemistry*, vol. 40, no. 1, pp. 259–278, 1971. 2

[15] P. Cuatrecasas, M. Wilchek, and C. B. Anfinsen, "Selective enzyme purification by affinity chromatography." *Proceedings of the National Academy of Sciences of the United States of America*, vol. 61, no. 2, pp. 636–643, Oct. 1968. 2

[16] P. Cuatrecasas, "Protein purification by affinity chromatography derivation of agarose and polyacrylamide beads," *Journal of Biological Chemistry*, vol. 245, no. 12, pp. 3059–3065, Jun. 1970. 2

[17] W. A. Bonner, H. R. Hulett, R. G. Sweet, and L. A. Herzenberg, "Fluorescence activated cell sorting," *Review of Scientific Instruments*, vol. 43, no. 3, pp. 404–409, Mar. 1972. 2

DOI:10.15774/PPKE.ITK.2015.011

[18] A. Y. Fu, C. Spence, A. Scherer, F. H. Arnold, and S. R. Quake, "A microfabricated fluorescence-activated cell sorter," *Nature Biotechnology*, vol. 17, no. 11, pp. 1109–1111, Nov. 1999. 2

[19] C. S. Owen and N. L. Sykes, "Magnetic labeling and cell sorting," *Journal of Immunological Methods*, vol. 73, no. 1, pp. 41–48, Oct. 1984. 2

[20] I. Safarik and M. Safarikova, "Use of magnetic techniques for the isolation of cells," *Journal of Chromatography B: Biomedical Sciences and Applications*, vol. 722, no. 1-2, pp. 33–53, Feb. 1999. 2

[21] D. Pappas and K. Wang, "Cellular separations: A review of new challenges in analytical chemistry," *Analytica Chimica Acta*, vol. 601, no. 1, pp. 26–35, Oct. 2007. 2

[22] B. Mosadegh, T. Bersano-Begey, J. Y. Park, M. A. Burns, and S. Takayama, "Next-generation integrated microfluidic circuits," *Lab on a Chip*, vol. 11, no. 17, pp. 2813–2818, Aug. 2011. 3

[23] H. Craighead, "Future lab-on-a-chip technologies for interrogating individual molecules," *Nature*, vol. 442, no. 7101, pp. 387–393, Jul. 2006. 3

[24] D. Mark, S. Haeberle, G. Roth, F. v. Stetten, and R. Zengerle, "Microfluidic lab-on-a-chip platforms: requirements, characteristics and applications," *Chemical Society Reviews*, vol. 39, no. 3, pp. 1153–1182, Feb. 2010. 3

[25] D. Erickson and D. Li, "Integrated microfluidic devices," *Analytica Chimica Acta*, vol. 507, no. 1, pp. 11–26, Apr. 2004. 3

[26] T. A. Franke and A. Wixforth, "Microfluidics for miniaturized laboratories on a chip," *ChemPhysChem*, vol. 9, no. 15, pp. 2140–2156, Oct. 2008. 3

[27] P. S. Dittrich and A. Manz, "Lab-on-a-chip: microfluidics in drug discovery," *Nature Reviews Drug Discovery*, vol. 5, no. 3, pp. 210–218, Mar. 2006. 3

[28] A. Manz, N. Graber, and H. M. Widmer, "Miniaturized total chemical analysis systems: A novel concept for chemical sensing," *Sensors and Actuators B: Chemical*, vol. 1, no. 1-6, pp. 244–248, Jan. 1990. 3

DOI:10.15774/PPKE.ITK.2015.011

[29] A. Manz, J. C. Fettinger, E. Verpoorte, H. Ludi, H. M. Widmer, and D. J. Harrison, "Micromachining of monocrystalline silicon and glass for chemical analysis systems a look into next century's technology or just a fashionable craze?" *TrAC Trends in Analytical Chemistry*, vol. 10, no. 5, pp. 144–149, May 1991. 3

[30] N. Pamme, "Continuous flow separations in microfluidic devices," *Lab on a Chip*, vol. 7, no. 12, pp. 1644–1659, Nov. 2007. 3, 4, 41

[31] J. C. Giddings, "A new separation concept based on a coupling of concentration and flow nonuniformities," *Separation Science*, vol. 1, no. 1, pp. 123–125, 1966. 4

[32] J. Shi, S. Yazdi, S.-C. S. Lin, X. Ding, I.-K. Chiang, K. Sharp, and T. J. Huang, "Three-dimensional continuous particle focusing in a microfluidic channelvia standing surface acoustic waves (SSAW)," *Lab on a Chip*, vol. 11, no. 14, pp. 2319–2324, Jun. 2011. 5

[33] J. Shi, H. Huang, Z. Stratton, Y. Huang, and T. J. Huang, "Continuous particle separation in a microfluidic channel via standing surface acoustic waves (SSAW)," *Lab on a Chip*, vol. 9, no. 23, pp. 3354–3359, Dec. 2009. 5

[34] J. Nam, H. Lim, D. Kim, and S. Shin, "Separation of platelets from whole blood using standing surface acoustic waves in a microchannel," *Lab Chip*, vol. 11, no. 19, pp. 3361–3364, Sep. 2011. 5

[35] T. Laurell, F. Petersson, and A. Nilsson, "Chip integrated strategies for acoustic separation and manipulation of cells and particles," *Chem. Soc. Rev.*, vol. 36, no. 3, pp. 492–506, Feb. 2007. 5

[36] J. Shi, X. Mao, D. Ahmed, A. Colletti, and T. J. Huang, "Focusing microparticles in a microfluidic channel with standing surface acoustic waves (SSAW)," *Lab on a Chip*, vol. 8, no. 2, pp. 221–223, Jan. 2008. 5

[37] T. Franke, S. Braunmuller, L. Schmid, A. Wixforth, and D. A. Weitz, "Surface acoustic wave actuated cell sorting (SAWACS)," *Lab on a Chip*, vol. 10, no. 6, pp. 789–794, Mar. 2010. 5

DOI:10.15774/PPKE.ITK.2015.011

[38] Y. Li, C. Dalton, H. J. Crabtree, G. Nilsson, and K. V. I. S. Kaler, "Continuous dielectrophoretic cell separation microfluidic device," *Lab on a Chip*, vol. 7, no. 2, pp. 239–248, Jan. 2007. 5

[39] A. Valero, T. Braschler, A. Rauch, N. Demierre, Y. Barral, and P. Renaud, "Tracking and synchronization of the yeast cell cycle using dielectrophoretic opacity," *Lab Chip*, vol. 11, no. 10, pp. 1754–1760, May 2011. 5

[40] M. J. Hilhorst, G. W. Somsen, and G. J. de Jong, "Capillary electrokinetic separation techniques for profiling of drugs and related products," *Electrophoresis*, vol. 22, no. 12, pp. 2542–2564, Jul. 2001. 5

[41] H.-H. Cui, J. Voldman, X.-F. He, and K.-M. Lim, "Separation of particles by pulsed dielectrophoresis," *Lab on a Chip*, vol. 9, no. 16, pp. 2306–2312, Aug. 2009. 5

[42] S.-I. Han, S.-M. Lee, Y.-D. Joo, and K.-H. Han, "Lateral dielectrophoretic microseparators to measure the size distribution of blood cells," *Lab on a Chip*, vol. 11, no. 22, pp. 3864–3872, Oct. 2011. 5

[43] M. D. Vahey and J. Voldman, "Emergent behavior in particle-laden microfluidic systems informs strategies for improving cell and particle separations," *Lab on a Chip*, vol. 11, no. 12, pp. 2071–2080, Jun. 2011. 5

[44] L. Wang, L. A. Flanagan, N. L. Jeon, E. Monuki, and A. P. Lee, "Dielectrophoresis switching with vertical sidewall electrodes for microfluidic flow cytometry," *Lab on a Chip*, vol. 7, no. 9, pp. 1114–1120, Aug. 2007. 5

[45] H.-S. Moon, K. Kwon, S.-I. Kim, H. Han, J. Sohn, S. Lee, and H.-I. Jung, "Continuous separation of breast cancer cells from blood samples using multi-orifice flow fractionation (MOFF) and dielectrophoresis (DEP)," *Lab on a Chip*, vol. 11, no. 6, pp. 1118–1125, Feb. 2011. 5

[46] H. Lee, J. Jung, S.-I. Han, and K.-H. Han, "High-speed RNA microextraction technology using magnetic oligo-dT beads and lateral magnetophoresis," *Lab on a Chip*, vol. 10, no. 20, pp. 2764–2770, Oct. 2010. 5

DOI:10.15774/PPKE.ITK.2015.011

[47] F. Shen, H. Hwang, Y. K. Hahn, and J.-K. Park, "Label-free cell separation using a tunable magnetophoretic repulsion force," *Analytical Chemistry*, vol. 84, no. 7, pp. 3075–3081, Feb. 2012. 5

[48] T. Zhu, R. Cheng, S. A. Lee, E. Rajaraman, M. A. Eiteman, T. D. Querec, E. R. Unger, and L. Mao, "Continuous-flow ferrohydrodynamic sorting of particles and cells in microfluidic devices," *Microfluidics and Nanofluidics*, vol. 13, no. 4, pp. 645–654, Oct. 2012. 5

[49] A. I. Rodriguez-Villarreal, M. D. Tarn, L. A. Madden, J. B. Lutz, J. Greenman, J. Samitier, and N. Pamme, "Flow focussing of particles and cells based on their intrinsic properties using a simple diamagnetic repulsion setup," *Lab on a Chip*, vol. 11, no. 7, pp. 1240–1248, Apr. 2011. 5

[50] D. Robert, N. Pamme, H. Conjeaud, F. Gazeau, A. Iles, and C. Wilhelm, "Cell sorting by endocytotic capacity in a microfluidic magnetophoresis device," *Lab on a Chip*, vol. 11, no. 11, pp. 1902–1910, Jun. 2011. 5

[51] N. Pamme and C. Wilhelm, "Continuous sorting of magnetic cells via on-chip free-flow magnetophoresis," *Lab on a Chip*, vol. 6, no. 8, pp. 974–980, Jul. 2006. 5

[52] P. Bhardwaj, P. Bagdi, and A. K. Sen, "Microfluidic device based on a micro-hydrocyclone for particle-liquid separation," *Lab on a Chip*, vol. 11, no. 23, pp. 4012–4021, Nov. 2011. 5

[53] D. Huh, J. H. Bahng, Y. Ling, H.-H. Wei, O. D. Kripfgans, J. B. Fowlkes, J. B. Grotberg, and S. Takayama, "Gravity-driven microfluidic particle sorting device with hydrodynamic separation amplification," *Analytical Chemistry*, vol. 79, no. 4, pp. 1369–1376, Jan. 2007. 5

[54] R. Gorkin, J. Park, J. Siegrist, M. Amasia, B. S. Lee, J.-M. Park, J. Kim, H. Kim, M. Madou, and Y.-K. Cho, "Centrifugal microfluidics for biomedical applications," *Lab on a Chip*, vol. 10, no. 14, pp. 1758–1773, Jun. 2010. 5

[55] S. Haeberle, T. Brenner, R. Zengerle, and J. Ducree, "Centrifugal extraction of plasma from whole blood on a rotating disk," *Lab on a Chip*, vol. 6, no. 6, pp. 776–781, May 2006. 5

DOI:10.15774/PPKE.ITK.2015.011

[56] H. Zhang, E. Tu, N. D. Hagen, C. A. Schnabel, M. J. Paliotti, W. S. Hoo, P. M. Nguyen, J. R. Kohrumel, W. F. Butler, M. Chachisvillis, and P. J. Marchand, "Time-of-flight optophoresis analysis of live whole cells in microfluidic channels," *Biomedical Microdevices*, vol. 6, no. 1, pp. 11–21, Mar. 2004. 5

[57] B. S. Zhao, Y.-M. Koo, and D. S. Chung, "Separations based on the mechanical forces of light," *Analytica Chimica Acta*, vol. 556, no. 1, pp. 97–103, Jan. 2006. 5

[58] T.-H. Wu, Y. Chen, S.-Y. Park, J. Hong, T. Teslaa, J. F. Zhong, D. D. Carlo, M. A. Teitell, and P.-Y. Chiou, "Pulsed laser triggered high speed microfluidic fluorescence activated cell sorter," *Lab on a Chip*, vol. 12, no. 7, pp. 1378–1383, Mar. 2012. 5

[59] M. Kersaudy-Kerhoas, D. M. Kavanagh, R. S. Dhariwal, C. J. Campbell, and M. P. Y. Desmulliez, "Validation of a blood plasma separation system by biomarker detection," *Lab on a Chip*, vol. 10, no. 12, pp. 1587–1595, Jun. 2010. 5

[60] O. Forouzan, J. M. Burns, J. L. Robichaux, W. L. Murfee, and S. S. Shevkoplyas, "Passive recruitment of circulating leukocytes into capillary sprouts from existing capillaries in a microfluidic system," *Lab on a chip*, vol. 11, no. 11, pp. 1924–1932, Jun. 2011. 5

[61] S. Sugaya, M. Yamada, and M. Seki, "Observation of nonspherical particle behaviors for continuous shape-based separation using hydrodynamic filtration," *Biomicrofluidics*, vol. 5, no. 2, p. 24103, 2011. 5

[62] J. Marchalot, Y. Fouillet, and J.-L. Achard, "Multi-step microfluidic system for blood plasma separation: architecture and separation efficiency," *Microfluidics and Nanofluidics*, pp. 1–14, Dec. 2013. 5

[63] M. Yamada and M. Seki, "Microfluidic particle sorter employing flow splitting and recombining," *Analytical Chemistry*, vol. 78, no. 4, pp. 1357–1362, Feb. 2006. 5

[64] M. Kersaudy-Kerhoas, R. Dhariwal, M. P. Y. Desmulliez, and L. Jouvet, "Hydrodynamic blood plasma separation in microfluidic channels," *Microfluidics and Nanofluidics*, vol. 8, no. 1, pp. 105–114, Jan. 2010. 5

DOI:10.15774/PPKE.ITK.2015.011

[65] A. I. Rodriguez-Villarreal, M. Arundell, M. Carmona, and J. Samitier, "High flow rate microfluidic device for blood plasma separation using a range of temperatures," *Lab on a chip*, vol. 10, no. 2, pp. 211–219, Jan. 2010. 5

[66] E. Sollier, M. Cubizolles, Y. Fouillet, and J.-L. Achard, "Fast and continuous plasma extraction from whole human blood based on expanding cell-free layer devices," *Biomedical microdevices*, vol. 12, no. 3, pp. 485–497, Jun. 2010. 5

[67] S. Yang, A. Undar, and J. D. Zahn, "A microfluidic device for continuous, real time blood plasma separation," *Lab on a Chip*, vol. 6, no. 7, pp. 871–880, Jun. 2006. 5

[68] D. H. Yoon, J. B. Ha, Y. K. Bahk, T. Arakawa, S. Shoji, and J. S. Go, "Size-selective separation of micro beads by utilizing secondary flow in a curved rectangular microchannel," *Lab on a Chip*, vol. 9, no. 1, pp. 87–90, Jan. 2009. 5

[69] W. C. Lee, A. A. S. Bhagat, S. Huang, K. J. V. Vliet, J. Han, and C. T. Lim, "High-throughput cell cycle synchronization using inertial forces in spiral microchannels," *Lab on a Chip*, vol. 11, no. 7, pp. 1359–1367, Apr. 2011. 5

[70] I. D. Johnston, M. B. McDonnell, C. K. L. Tan, D. K. McCluskey, M. J. Davies, and M. C. Tracey, "Dean flow focusing and separation of small microspheres within a narrow size range," *Microfluidics and Nanofluidics*, pp. 1–10, Jan. 2014. 5

[71] A. Russom, A. K. Gupta, S. Nagrath, D. D. Carlo, J. F. Edd, and M. Toner, "Differential inertial focusing of particles in curved low-aspect-ratio microchannels," *New Journal of Physics*, vol. 11, no. 7, p. 075025, Jul. 2009. 5

[72] A. A. S. Bhagat, S. S. Kuntaegowdanahalli, and I. Papautsky, "Continuous particle separation in spiral microchannels using dean flows and differential migration," *Lab on a Chip*, vol. 8, no. 11, pp. 1906–1914, Nov. 2008. 5

[73] A. A. S. Bhagat and S. S. Kuntaegowdanahalli, "Inertial microfluidics for continuous particle filtration and extraction," *Microfluidics and Nanofluidics*, vol. 7, no. 2, pp. 217–226, Aug. 2009. 5

DOI:10.15774/PPKE.ITK.2015.011

[74] D. D. Carlo, "Inertial microfluidics," *Lab on a Chip*, vol. 9, no. 21, pp. 3038–3046, Nov. 2009. 5

[75] S. S. Kuntaegowdanahalli, A. A. S. Bhagat, G. Kumar, and I. Papautsky, "Inertial microfluidics for continuous particle separation in spiral microchannels," *Lab on a Chip*, vol. 9, no. 20, pp. 2973–2980, Oct. 2009. 5

[76] D. D. Carlo, D. Irimia, R. G. Tompkins, and M. Toner, "Continuous inertial focusing, ordering, and separation of particles in microchannels," *Proceedings of the National Academy of Sciences*, vol. 104, no. 48, pp. 18 892–18 897, Nov. 2007. 5

[77] S. Choi and J.-K. Park, "Tuneable hydrophoretic separation using elastic deformation of poly(dimethylsiloxane)," *Lab on a Chip*, vol. 9, no. 13, pp. 1962–1965, Jul. 2009. 5

[78] S. Choi and J. K. Park, "Sheathless hydrophoretic particle focusing in a microchannel with exponentially increasing obstacle arrays," *Analytical Chemistry*, vol. 80, no. 8, pp. 3035–3039, Apr. 2008. 5

[79] S. Choi, T. Ku, S. Song, C. Choi, and J. K. Park, "Hydrophoretic high-throughput selection of platelets in physiological shear-stress range," *Lab on a Chip*, vol. 11, no. 3, pp. 413–418, Feb. 2011. 5

[80] S. Choi and J.-K. Park, "Continuous hydrophoretic separation and sizing of microparticles using slanted obstacles in a microchannel," *Lab on a Chip*, vol. 7, no. 7, pp. 890–897, Jun. 2007. 5

[81] S. Choi, J. M. Karp, and R. Karnik, "Cell sorting by deterministic cell rolling," *Lab on a Chip*, vol. 12, no. 8, pp. 1427–1430, Apr. 2012. 5

[82] S. Choi, O. Levy, M. B. Coelho, J. M. S. Cabral, J. M. Karp, and R. Karnik, "A cell rolling cytometer reveals the correlation between mesenchymal stem cell dynamic adhesion and differentiation state," *Lab on a Chip*, vol. 14, no. 1, pp. 161–166, Nov. 2013. 5

DOI:10.15774/PPKE.ITK.2015.011

[83] S. H. Holm, J. P. Beech, M. P. Barrett, and J. O. Tegenfeldt, "Separation of parasites from human blood using deterministic lateral displacement," *Lab on a chip*, vol. 11, no. 7, pp. 1326–1332, Apr. 2011. 5, 43

[84] J. P. Gleghorn, E. D. Pratt, D. Denning, H. Liu, N. H. Bander, S. T. Tagawa, D. M. Nanus, P. A. Giannakakou, and B. J. Kirby, "Capture of circulating tumor cells from whole blood of prostate cancer patients using geometrically enhanced differential immunocapture (GEDI) and a prostate-specific antibody," *Lab on a Chip*, vol. 10, no. 1, pp. 27–29, Jan. 2010. 5, 43

[85] N. Srivastava, C. Din, A. Judson, N. C. MacDonald, and C. D. Meinhart, "A unified scaling model for flow through a lattice of microfabricated posts," *Lab on a Chip*, vol. 10, no. 9, pp. 1148–1152, May 2010. 5

[86] S. Zheng, R. Yung, Y.-C. Tai, and H. Kasdan, "Deterministic lateral displacement MEMS device for continuous blood cell separation," in *18th IEEE International Conference on Micro Electro Mechanical Systems, 2005. MEMS 2005*, Jan. 2005, pp. 851–854. 5, 43

[87] K. Loutherback, K. S. Chou, J. Newman, J. Puchalla, R. H. Austin, and J. C. Sturm, "Improved performance of deterministic lateral displacement arrays with triangular posts," *Microfluidics and Nanofluidics*, vol. 9, no. 6, pp. 1143–1149, Dec. 2010. 5, 43

[88] L. R. Huang, E. C. Cox, R. H. Austin, and J. C. Sturm, "Continuous particle separation through deterministic lateral displacement," *Science*, vol. 304, no. 5673, pp. 987–990, May 2004. 5, 42, 43, 44, 56

[89] K. J. Morton, K. Loutherback, D. W. Inglis, O. K. Tsui, J. C. Sturm, S. Y. Chou, and R. H. Austin, "Crossing microfluidic streamlines to lyse, label and wash cells," *Lab on a Chip*, vol. 8, no. 9, pp. 1448–1453, Aug. 2008. 5, 43

[90] H. N. Joensson, M. Uhlen, and H. A. Svahn, "Droplet size based separation by deterministic lateral displacement-separating droplets by cell-induced shrinking," *Lab on a Chip*, vol. 11, no. 7, pp. 1305–1310, Apr. 2011. 5, 43

DOI:10.15774/PPKE.ITK.2015.011

[91] J. A. Davis, D. W. Inglis, K. J. Morton, D. A. Lawrence, L. R. Huang, S. Y. Chou, J. C. Sturm, and R. H. Austin, "Deterministic hydrodynamics: Taking blood apart," *Proceedings of the National Academy of Sciences*, vol. 103, no. 40, pp. 14 779–14 784, Oct. 2006. 5, 43

[92] D. W. Inglis, N. Herman, and G. Vesey, "Highly accurate deterministic lateral displacement device and its application to purification of fungal spores," *Biomicrofluidics*, vol. 4, no. 2, p. 024109, Jun. 2010. 5, 43

[93] B. R. Long, M. Heller, J. P. Beech, H. Linke, H. Bruus, and J. O. Tegenfeldt, "Multidirectional sorting modes in deterministic lateral displacement devices," *Physical Review E*, vol. 78, no. 4, p. 046304, Oct. 2008. 5

[94] M. Heller and H. Bruus, "A theoretical analysis of the resolution due to diffusion and size dispersion of particles in deterministic lateral displacement devices," *Journal of Micromechanics and Microengineering*, vol. 18, no. 7, p. 075030, Jul. 2008. 5

[95] J. V. Green, M. Radisic, and S. K. Murthy, "Deterministic lateral displacement as a means to enrich large cells for tissue engineering," *Analytical Chemistry*, vol. 81, no. 21, pp. 9178–9182, Nov. 2009. 5, 43

[96] N. Li, D. Kamei, and C.-M. Ho, "On-chip continuous blood cell subtype separation by deterministic lateral displacement," in *2nd IEEE International Conference on Nano/Micro Engineered and Molecular Systems, 2007. NEMS '07*, Jan. 2007, pp. 932–936. 5, 43

[97] D. W. Inglis, K. J. Morton, J. A. Davis, T. J. Zieziulewicz, D. A. Lawrence, R. H. Austin, and J. C. Sturm, "Microfluidic device for label-free measurement of platelet activation," *Lab on a Chip*, vol. 8, no. 6, pp. 925–931, May 2008. 5, 43

[98] M. Al-Fandi, M. Al-Rousan, M. A. K. Jaradat, and L. Al-Ebbini, "New design for the separation of microorganisms using microfluidic deterministic lateral displacement," *Robotics and Computer-Integrated Manufacturing*, vol. 27, no. 2, pp. 237–244, Apr. 2011. 5, 43

DOI:10.15774/PPKE.ITK.2015.011

[99] T. Bowman, J. Frechette, and G. Drazer, "Force driven separation of drops by deterministic lateral displacement," *Lab on a Chip*, vol. 12, no. 16, pp. 2903–2908, Jul. 2012. 5

[100] Z. Liu, F. Huang, J. Du, W. Shu, H. Feng, X. Xu, and Y. Chen, "Rapid isolation of cancer cells using microfluidic deterministic lateral displacement structure," *Biomicrofluidics*, vol. 7, no. 1, p. 011801, Jan. 2013. 5, 43

[101] D. W. Inglis, J. A. Davis, R. H. Austin, and J. C. Sturm, "Critical particle size for fractionation by deterministic lateral displacement," *Lab on a Chip*, vol. 6, no. 5, pp. 655–658, May 2006. 5, 43, 56, 57

[102] Y. Koh, H. Kang, S. H. Lee, J.-K. Yang, J.-H. Kim, Y.-S. Lee, and Y.-K. Kim, "Nanoslit membrane-integrated fluidic chip for protein detection based on size-dependent particle trapping," *Lab on a Chip*, vol. 14, no. 1, pp. 237–243, Nov. 2013. 5

[103] P. Lv, Z. Tang, X. Liang, M. Guo, and R. P. S. Han, "Spatially gradated segregation and recovery of circulating tumor cells from peripheral blood of cancer patients," *Biomicrofluidics*, vol. 7, no. 3, p. 034109, May 2013. 5

[104] H. M. Ji, V. Samper, Y. Chen, C. K. Heng, T. M. Lim, and L. Yobas, "Silicon-based microfilters for whole blood cell separation," *Biomedical Microdevices*, vol. 10, no. 2, pp. 251–257, Apr. 2008. 5

[105] H. Wei, B.-h. Chueh, H. Wu, E. W. Hall, C.-w. Li, R. Schirhagl, J.-M. Lin, and R. N. Zare, "Particle sorting using a porous membrane in a microfluidic device," *Lab on a Chip*, vol. 11, no. 2, pp. 238–245, Jan. 2011. 5

[106] K. Aran, A. Fok, L. A. Sasso, N. Kamdar, Y. Guan, Q. Sun, A. Undar, and J. D. Zahn, "Microfiltration platform for continuous blood plasma protein extraction from whole blood during cardiac surgery," *Lab on a Chip*, vol. 11, no. 17, pp. 2858–2868, Aug. 2011. 5

[107] J. S. Kuo, Y. Zhao, P. G. Schiro, L. Ng, D. S. W. Lim, J. P. Shelby, and D. T. Chiu, "Deformability considerations in filtration of biological cells," *Lab on a Chip*, vol. 10, no. 7, pp. 837–842, Apr. 2010. 5

DOI:10.15774/PPKE.ITK.2015.011

[108] J. S. Shim and C. H. Ahn, "An on-chip whole blood/plasma separator using hetero-packed beads at the inlet of a microchannel," *Lab on a Chip*, vol. 12, no. 5, pp. 863–866, Feb. 2012. 5

[109] M. Nakashima, M. Yamada, and M. Seki, "Pinched flow fractionation (PFF) for continuous particle separation in a microfluidic device," in *Micro Electro Mechanical Systems, 2004. 17th IEEE International Conference on. (MEMS)*, 2004, pp. 33–36. 5

[110] T. Morijiri, S. Sunahiro, M. Senaha, M. Yamada, and M. Seki, "Sedimentation pinched-flow fractionation for size- and density-based particle sorting in microchannels," *Microfluidics and Nanofluidics*, vol. 11, no. 1, pp. 105–110, Jul. 2011. 5

[111] A. L. Vig and A. Kristensen, "Separation enhancement in pinched flow fractionation," *Applied Physics Letters*, vol. 93, no. 20, p. 203507, Nov. 2008. 5

[112] A. Jain and J. D. Posner, "Particle dispersion and separation resolution of pinched flow fractionation," *Analytical Chemistry*, vol. 80, no. 5, pp. 1641–1648, Mar. 2008. 5

[113] A. V. Larsen, L. Poulsen, H. Birgens, M. Dufva, and A. Kristensen, "Pinched flow fractionation devices for detection of single nucleotide polymorphisms," *Lab on a Chip*, vol. 8, no. 5, pp. 818–821, Apr. 2008. 5

[114] J. S. Dudani, D. R. Gossett, H. T. K. Tse, and D. D. Carlo, "Pinched-flow hydrodynamic stretching of single-cells," *Lab on a Chip*, vol. 13, no. 18, pp. 3728–3734, Aug. 2013. 5

[115] M. Yamada, M. Nakashima, and M. Seki, "Pinched flow fractionation:? continuous size separation of particles utilizing a laminar flow profile in a pinched microchannel," *Analytical Chemistry*, vol. 76, no. 18, pp. 5465–5471, Sep. 2004. 5

[116] A. A. S. Bhagat, H. W. Hou, L. D. Li, C. T. Lim, and J. Han, "Pinched flow coupled shear-modulated inertial microfluidics for high-throughput rare blood cell separation," *Lab on a Chip*, vol. 11, no. 11, pp. 1870–1878, Jun. 2011. 5

DOI:10.15774/PPKE.ITK.2015.011

[117] C. Cupelli, T. Borchardt, T. Steiner, N. Paust, R. Zengerle, and M. Santer, "Leukocyte enrichment based on a modified pinched flow fractionation approach," *Microfluidics and Nanofluidics*, vol. 14, no. 3-4, pp. 551–563, Mar. 2013. 5

[118] O. Shardt, S. K. Mitra, and J. J. Derksen, "Lattice boltzmann simulations of pinched flow fractionation," *Chemical Engineering Science*, vol. 75, pp. 106–119, Jun. 2012. 5

[119] H. Lim, J. Nam, and S. Shin, "Lateral migration of particles suspended in viscoelastic fluids in a microchannel flow," *Microfluidics and Nanofluidics*, pp. 1–10, Feb. 2014. 5

[120] A. Srivastav, T. Podgorski, and G. Coupier, "Efficiency of size-dependent particle separation by pinched flow fractionation," *Microfluidics and Nanofluidics*, vol. 13, no. 5, pp. 697–701, Nov. 2012. 5

[121] Y. Sai, M. Yamada, M. Yasuda, and M. Seki, "Continuous separation of particles using a microfluidic device equipped with flow rate control valves," *Journal of Chromatography A*, vol. 1127, no. 12, pp. 214–220, Sep. 2006. 5

[122] J. Takagi, M. Yamada, M. Yasuda, and M. Seki, "Continuous particle separation in a microchannel having asymmetrically arranged multiple branches," *Lab on a Chip*, vol. 5, no. 7, pp. 778–784, Jun. 2005. 5

[123] X. Zhang, J. M. Cooper, P. B. Monaghan, and S. J. Haswell, "Continuous flow separation of particles within an asymmetric microfluidic device," *Lab on a Chip*, vol. 6, no. 4, pp. 561–566, Mar. 2006. 5

[124] H. W. Hou, H. Y. Gan, A. A. S. Bhagat, L. D. Li, C. T. Lim, and J. Han, "A microfluidics approach towards high-throughput pathogen removal from blood using margination," *Biomicrofluidics*, vol. 6, no. 2, p. 024115, Jun. 2012. 5

[125] A. J. Laki, K. Ivan, E. Fok, and P. Civera, "Filtration of nematodes using an integrated microcapillary system," *BioNanoScience*, pp. 1–11, Oct. 2014. 6

[126] A. J. Laki, L. Botzheim, K. Ivn, V. Tamsi, and P. Civera, "Separation of microvesicles from serological samples using deterministic lateral displacement effect," *BioNanoScience*, pp. 1–7, Nov. 2014. 6

DOI:10.15774/PPKE.ITK.2015.011

[127] J. E. Hall, *Guyton and Hall Textbook of Medical Physiology: Enhanced E-book*. Elsevier Health Sciences, Jul. 2010. 7, 8

[128] J. Mazumdar, *Biofluid Mechanics*. World Scientific, Nov. 1992. 8

[129] J. Szentágothai and M. Réthelyi, *Funkciális anatómia*. Medicina könyvkiadó RT., 2002. 9, 17

[130] R. Fahraus and T. Lindqvist, "The viscosity of the blood in narrow capillary tubes," *American Journal of Physiology – Legacy Content*, vol. 96, no. 3, pp. 562–568, Jan. 1931. 10, 18

[131] J. Bec, H. Homann, and S. S. Ray, "Gravity-driven enhancement of heavy particle clustering in turbulent flow," *Physical Review Letters*, vol. 112, no. 18, p. 184501, May 2014. 13

[132] D. R. Lide, *CRC Handbook of Chemistry and Physics, 85th Edition*. CRC Press, Jun. 2004. 14

[133] T. Kenner, H. Leopold, and H. Hinghofer-Szalkay, "The continuous high-precision measurement of the density of flowing blood," *Pflugers Archiv*, vol. 370, no. 1, pp. 25–29, Jan. 1977. 14

[134] W. L. Chandler and G. Schmer, "Evaluation of a new dynamic viscometer for measuring the viscosity of whole blood and plasma." *Clinical Chemistry*, vol. 32, no. 3, pp. 505–507, Mar. 1986. 14

[135] T. T. Nguyen, R. Mongrain, J. Brunette, O. F. Bertrand, J.-C. Tardif, and Y. Biadillah, "A method for matching the refractive index and kinematic viscosity of a blood analog for flow visualization in hydraulic cardiovascular models," *Journal of Biomechanical Engineering*, vol. 126, no. 4, pp. 529–535, Sep. 2004. 14

[136] J. Wang, W. Huang, R. S. Bhullar, and P. Tong, "Modeling of surface-tension-driven flow of blood in capillary tubes," *Mechanics & chemistry of biosystems: MCB*, vol. 1, no. 2, pp. 161–167, Jun. 2004. 14

DOI:10.15774/PPKE.ITK.2015.011

[137] H. Jasper and T. C, "Cerebral blood flow and pH in excessive cortical discharge induced by metrazol and electrical stimulation," *Journal of Neurophysiology*, vol. 4, pp. 333–347, 1941. 14

[138] G. D. Lowe, F. G. Fowkes, J. Dawes, P. T. Donnan, S. E. Lennie, and E. Housley, "Blood viscosity, fibrinogen, and activation of coagulation and leukocytes in peripheral arterial disease and the normal population in the edinburgh artery study," *Circulation*, vol. 87, no. 6, pp. 1915–1920, Jan. 1993. 14

[139] C. Bonadonna, G. G. J. Ernst, and R. S. J. Sparks, "Thickness variations and volume estimates of tephra fall deposits: the importance of particle reynolds number," *Journal of Volcanology and Geothermal Research*, vol. 81, no. 3-4, pp. 173–187, May 1998. 14

[140] D. M. Eckmann, S. Bowers, M. Stecker, and A. T. Cheung, "Hematocrit, volume expander, temperature, and shear rate effects on blood viscosity," *Anesthesia & Analgesia*, vol. 91, no. 3, pp. 539–545, Jan. 2000. 18

[141] L. S. Garcia and D. A. Bruckner, *Diagnostic medical parasitology*. Elsevier, 1988. 19, 20

[142] A. Muro, C. Genchi, M. Cordero, and F. Simon, "Human dirofilariasis in the european union," *Parasitology Today (Personal Ed.)*, vol. 15, no. 9, pp. 386–389, Sep. 1999. 20, 24

[143] S. Pampiglione and F. Rivasi, "Human dirofilariasis due to dirofilaria (nochtiella) repens: an update of world literature from 1995 to 2000," *Parassitologia*, vol. 42, no. 3-4, pp. 231–254, Dec. 2000. 20

[144] E. Joseph, A. Matthai, L. K. Abraham, and S. Thomas, "Subcutaneous human dirofilariasis," *Journal of Parasitic Diseases: Official Organ of the Indian Society for Parasitology*, vol. 35, no. 2, pp. 140–143, Oct. 2011. 20

[145] F. Simón, J. López-Belmonte, C. Marcos-Atxutegi, R. Morchón, and J. R. Martín-Pacho, "What is happening outside north america regarding human dirofilariasis?" *Veterinary parasitology*, vol. 133, no. 2-3, pp. 181–189, Oct. 2005. 20

DOI:10.15774/PPKE.ITK.2015.011

[146] C. Genchi, L. Venco, and M. Genchi, "Guideline for the laboratory diagnosis of canine and feline dirofilaria infections," *Mappe Parassitologiche*, pp. 139–144, Feb. 2007. 20, 23, 24, 38

[147] T. C. Orihel and M. L. Eberhard, "Zoonotic filariasis," *Clinical Microbiology Reviews*, vol. 11, no. 2, pp. 366–381, Apr. 1998. 21

[148] K. W. Knauer, "Human dirofilariasis," *Clinical Techniques in Small Animal Practice*, vol. 13, no. 2, pp. 96–98, May 1998. 21

[149] M. T. Manfredi, A. d. Cerbo, and M. Genchi, "Biology of filarial worms parasitizing dogs and cats." *Mappe Parassitologiche*, vol. 8, pp. 39–45, 2007. 22, 25

[150] M. A. Peribanez, J. Lucientes, S. Arce, M. Morales, J. A. Castillo, and M. J. Gracia, "Histochemical differentiation of dirofilaria immitis, dirofilaria repens and acanthocheilonema dracunculoides microfilariae by staining with a commercial kit, leucognost-SP," *Veterinary Parasitology*, vol. 102, no. 1?2, pp. 173–175, Dec. 2001. 24

[151] G. Lawrence T., G. Rb, B. Eb, M.-G. M, P. Gj, D. Lm, R. Cr, and M. Jb, "Serologic pattern of canine heartworm (dirofilaria immitis) infection." *American journal of veterinary research*, vol. 45, no. 6, pp. 1178–1183, Jun. 1984. 24

[152] L. Roth, L. Brown, S. Brum, L. F. M. Nelson, D. Reczeck, and D. v. Schantz, "Comparison of three diagnostic tests for dirofilaria immitis in a low-incidence area," *Journal of Veterinary Diagnostic Investigation*, vol. 5, no. 4, pp. 647–648, Oct. 1993. 24

[153] B. Santamaria, M. Cordero, A. Muro, and F. Simon, "Evaluation of dirofilaria immitis excretory/secretory products for seroepidemiological studies on human dirofilariosis," *Parasite (Paris, France)*, vol. 2, no. 3, pp. 269–273, Sep. 1995. 24

[154] F. Simon, G. Prieto, A. Muro, G. Cancrini, M. Cordero, and C. Genchi, "Human humoral immune response to dirofilaria species," *Parassitologia*, vol. 39, no. 4, pp. 397–400, Dec. 1997. 24

DOI:10.15774/PPKE.ITK.2015.011

[155] L. Perera, J. L. Perez-Arellano, M. Cordero, F. Simon, and A. Muro, "Utility of antibodies against a 22 kD molecule of dirofilaria immitis in the diagnosis of human pulmonary dirofilariasis," *Tropical medicine & international health: TM & IH*, vol. 3, no. 2, pp. 151–155, Feb. 1998. 24

[156] G. Prieto, F. Simon, C. Genchi, J. W. McCall, and L. Venco, "Utility of adult antigens of dirofilaria immitis for the early detection of dirofilariosis and for the evaluation of chemoprophylactic treatment in experimentally infected cats," *Veterinary Parasitology*, vol. 86, no. 1, pp. 5–13, Sep. 1999. 24

[157] G. Favia, A. Lanfrancotti, A. della Torre, G. Cancrini, and M. Coluzzi, "Polymerase chain reaction-identification of dirofilaria repens and dirofilaria immitis," *Parasitology*, vol. 113 (Pt 6), pp. 567–571, Dec. 24

[158] G. Favia, A. Lanfrancotti, A. della Torre, and G. Cancrini, "Advances in the identification of dirofilaria repens and dirofilaria immitis by a PCR-based approach," *Parassitologia*, vol. 39, no. 4, pp. 401–402, Dec. 1997. 24

[159] G. Cancrini, G. Prieto, G. Favia, S. Giannetto, R. Tringali, M. Pietrobelli, and F. Simon, "Serological assays on eight cases of human dirofilariasis identified by morphology and DNA diagnostics," *Annals of Tropical Medicine and Parasitology*, vol. 93, no. 2, pp. 147–152, Mar. 1999. 24

[160] J. H. Theis, "Public health aspects of dirofilariasis in the united states," *Veterinary parasitology*, vol. 133, no. 2-3, pp. 157–180, Oct. 2005. 21

[161] J. C. McDonald and G. M. Whitesides, "Poly(dimethylsiloxane) as a material for fabricating microfluidic devices," *Accounts of Chemical Research*, vol. 35, no. 7, pp. 491–499, Jul. 2002. 29, 32, 49

[162] B. György, T. G. Szabó, M. Pásztói, Z. Pál, P. Misják, B. Aradi, V. László, E. Pállinger, E. Pap, A. Kittel, G. Nagy, A. Falus, and E. I. Buzás, "Membrane vesicles, current state-of-the-art: emerging role of extracellular vesicles," *Cellular and molecular life sciences: CMLS*, vol. 68, no. 16, pp. 2667–2688, Aug. 2011. 41

[163] C. D'Souza-Schorey and J. W. Clancy, "Tumor-derived microvesicles: shedding light on novel microenvironment modulators and prospective cancer biomarkers," *Genes & Development*, vol. 26, no. 12, pp. 1287–1299, Jun. 2012. 41

DOI:10.15774/PPKE.ITK.2015.011

[164] C. Thery, S. Amigorena, G. Raposo, and A. Clayton, "Isolation and characterization of exosomes from cell culture supernatants and biological fluids," in *Current Protocols in Cell Biology*, J. S. Bonifacino, M. Dasso, J. B. Harford, J. Lippincott-Schwartz, and K. M. Yamada, Eds. Hoboken, NJ, USA: John Wiley & Sons, Inc., Apr. 2006. 42

[165] H. G. Lamparski, A. Metha-Damani, J.-Y. Yao, S. Patel, D.-H. Hsu, C. Ruegg, and J.-B. Le Pecq, "Production and characterization of clinical grade exosomes derived from dendritic cells," *Journal of Immunological Methods*, vol. 270, no. 2, pp. 211–226, Dec. 2002. 42

[166] D. W. Inglis, M. Lord, and R. E. Nordon, "Scaling deterministic lateral displacement arrays for high throughput and dilution-free enrichment of leukocytes," *Journal of Micromechanics and Microengineering*, vol. 21, no. 5, p. 054024, May 2011. 43

[167] K. K. Zeming, S. Ranjan, and Y. Zhang, "Rotational separation of non-spherical bioparticles using i-shaped pillar arrays in a microfluidic device," *Nature Communications*, vol. 4, p. 1625, Mar. 2013. 43

[168] J. P. Beech, S. H. Holm, K. Adolfsson, and J. O. Tegenfeldt, "Sorting cells by size, shape and deformability," *Lab on a chip*, vol. 12, no. 6, pp. 1048–1051, Mar. 2012. 43, 55

[169] K. Loutherback, J. D'Silva, L. Liu, A. Wu, R. H. Austin, and J. C. Sturm, "Deterministic separation of cancer cells from blood at 10 mL/min," *AIP Advances*, vol. 2, no. 4, Oct. 2012. 43

[170] J. McGrath, M. Jimenez, and H. Bridle, "Deterministic lateral displacement for particle separation: a review," *Lab on a Chip*, Sep. 2014. 43, 68

[171] Y. S. Lubbersen, M. A. I. Schutyser, and R. M. Boom, "Suspension separation with deterministic ratchets at moderate reynolds numbers," *Chemical Engineering Science*, vol. 73, pp. 314–320, May 2012. 43

[172] J. P. Beech and J. O. Tegenfeldt, "Tuneable separation in elastomeric microfluidics devices," *Lab on a Chip*, vol. 8, no. 5, pp. 657–659, Apr. 2008. 43

DOI:10.15774/PPKE.ITK.2015.011

[173] R. Devendra and G. Drazer, "Gravity driven deterministic lateral displacement for particle separation in microfluidic devices," *Analytical Chemistry*, vol. 84, no. 24, pp. 10 621–10 627, Dec. 2012. 43

[174] T. Kulrattanarak, R. G. M. v. d. Sman, C. G. P. H. Schron, and R. M. Boom, "Analysis of mixed motion in deterministic ratchets via experiment and particle simulation," *Microfluidics and Nanofluidics*, vol. 10, no. 4, pp. 843–853, Apr. 2011. 43

[175] J. P. Beech, P. Jnsson, and J. O. Tegenfeldt, "Tipping the balance of deterministic lateral displacement devices using dielectrophoresis," *Lab on a chip*, vol. 9, no. 18, pp. 2698–2706, Sep. 2009. 43

[176] K. Loutherback, J. Puchalla, R. H. Austin, and J. C. Sturm, "Deterministic microfluidic ratchet," *Physical Review Letters*, vol. 102, no. 4, p. 045301, Jan. 2009. 43

[177] D. J. Collins, T. Alan, and A. Neild, "Particle separation using virtual deterministic lateral displacement (vDLD)," *Lab on a Chip*, vol. 14, no. 9, pp. 1595–1603, Apr. 2014. 43

[178] D. C. Duffy, J. C. McDonald, O. J. A. Schueller, and G. M. Whitesides, "Rapid prototyping of microfluidic systems in poly(dimethylsiloxane)," *Analytical Chemistry*, vol. 70, no. 23, pp. 4974–4984, Dec. 1998. 49

[179] L. Turiák, P. Misják, T. G. Szabó, B. Aradi, K. Pálóczi, O. Ozohanics, L. Drahos, A. Kittel, A. Falus, E. I. Buzás, and K. Vákey, "Proteomic characterization of thymocyte-derived microvesicles and apoptotic bodies in BALB/c mice," *Journal of proteomics*, vol. 74, no. 10, pp. 2025–2033, Sep. 2011. 50

[180] H. Amini, W. Lee, and D. Di Carlo, "Inertial microfluidic physics," *Lab on a Chip*, vol. 14, no. 15, pp. 2739–2761, Aug. 2014. 58

[181] Z. Wu, B. Willing, J. Bjerketorp, J. K. Jansson, and K. Hjort, "Soft inertial microfluidics for high throughput separation of bacteria from human blood cells," *Lab on a Chip*, vol. 9, no. 9, pp. 1193–1199, May 2009. 58

DOI:10.15774/PPKE.ITK.2015.011

[182] E. S. Asmolov, "The inertial lift on a spherical particle in a plane poiseuille flow at large channel reynolds number," *Journal of Fluid Mechanics*, vol. 381, pp. 63–87, Feb. 1999. 60

[183] B. P. Ho and L. G. Leal, "Inertial migration of rigid spheres in two-dimensional unidirectional flows," *Journal of Fluid Mechanics*, vol. 65, no. 02, pp. 365–400, Aug. 1974. 60

[184] J. A. Schonberg and E. J. Hinch, "Inertial migration of a sphere in poiseuille flow," *Journal of Fluid Mechanics*, vol. 203, pp. 517–524, Jun. 1989. 60

[185] R. Quek, D. V. Le, and K.-H. Chiam, "Separation of deformable particles in deterministic lateral displacement devices," *Physical Review E*, vol. 83, no. 5, p. 056301, May 2011. 67

[186] D. W. Inglis, "Efficient microfluidic particle separation arrays," *Applied Physics Letters*, vol. 94, no. 1, p. 013510, Jan. 2009. 67